Improving Apparent Inertia, Damping, Stability, and Fault Recovery Performance in AC Power Networks with Virtual Synchronous Machines

By

Ting Lin

A Thesis submitted to the Faculty of Graduate Studies of
The University of Manitoba
in partial fulfillment of the requirements of the degree of

Doctor of Philosophy

Department of Electrical and Computer Engineering
Faculty of Engineering
University of Manitoba
Winnipeg, Manitoba

Abstract

Traditional VSC control is of the "Grid Following Type" (GFL), where the turn-on pulses to the converter switches are determined based on fast synchronization with the external grid voltage phasor. GFL VSC have difficulty operating into very weak ac networks. In contrast, GFM controlled VSC maintains an internal voltage phasor and has the potential to maintain system stability under such challenging network conditions. One important aspect of VSM type control of a VSC is that it imparts an artificial inertia and damping behaviour to the VSC, which can have a significant impact on the VSMs ability to survive frequency events triggered by transient mismatch between generation and loads. This research investigates the disturbance ride through, stability and inertia support of using Virtual Synchronous machine (VSM) Grid-Forming (GFM) control on Voltage-Sourced Converters (VSC) High Voltage direct current (HVdc) transmission system.

An adaptive fault ride through control mode is proposed for VSM to improve its post fault recovery transient and voltage phase angle jump ride through performance. The EMT simulation shows the disturbance ride through performance of VSM GFM with cascaded or switchable current control can be optimized by transiently changing the active power order and the damping coefficient in its power synchronization loop.

Linearized models of the VSM with inertia and damping parameters are developed and validated using detailed EMT simulation for system small-signal stability analysis and controller parameter design under different system strengths. A current limiting feature is a necessity in any VSC due to the limited overcurrent ratings of the VSC's power electronic

switches. However, eigenvalue analysis reveals that the VSM can experience instability when connected to strong ac networks with the inclusion of the in-line cascaded current limiting. However, with proper controller tuning, a single suitable gain parameter set can nevertheless be found to allow stable operation under both weak and strong system strength.

An important contribution of this research is the development of a novel method for online estimation of system inertia in inverter-based resources (IBRs). A small voltage or current probing signal that is different from system frequency can be injected to a network to estimate the inertia from the GFM VSCs and synchronous machines. Since the injected signal is very small, the inertia of the GFM IBR can be conveniently measured during the steady-state operation without triggering other transient frequency support control. This can greatly improve the inertia measurement accuracy compared with the more conventional ROCOF observation method.

Acknowledge

I would like to express my deepest gratitude and appreciation to all the individuals who have contributed to the completion of this doctoral thesis. Their support, guidance, and encouragement have been invaluable throughout this journey.

First and foremost, I extend my heartfelt thanks to my supervisor, Dr. Aniruddha Gole. Your unwavering commitment to excellence, your inspiration, and your patience have been instrumental in shaping my research and molding me into a better scholar. Those insightful discussions (and the “coffee breaks”) have guided me to strive for higher standards and have been crucial in refining the quality of this thesis.

I am also indebted to the members of my thesis committee, Dr. Udaya Annakkage, Dr. Ioni Fernando, and the external examiner Dr. Vijay Sood, for their invaluable expertise, insightful suggestions. Their collective knowledge has enriched my research and helped me navigate through various challenges encountered along the way.

My heartfelt appreciation goes to the faculty members and my research lab mates at the University of Manitoba, whose contributions and dedication to their respective fields have inspired me throughout my academic journey. I am grateful for the intellectual environment and resources provided, which have significantly contributed to the development of my research.

I would like to extend my gratitude to the power system engineers at Electranix Corporation who have been sources of inspiration, support, and camaraderie. Their friendship, stimulating discussions, and willingness to collaborate have greatly enhanced my research experience. The collective intellectual atmosphere within Electranix has been crucial in shaping my ideas and broadening my perspectives.

Furthermore, I would like to express my gratitude to my parents, Yining Lin and Ling Liu, and my beloved, Chelsea Bingqing Liu, for their unwavering support, love, and encouragement throughout this arduous journey. Their belief in my abilities and their sacrifices have been the driving force and guiding light behind my perseverance, and I am forever grateful for their presence in my life.

To all those mentioned above and to the countless others who have contributed in various ways, please accept my heartfelt appreciation. This thesis would not have been possible without your support and belief in my capabilities.

Thank you.

Ting Lin

Table of Contents

List of Tables

List of Figures

Chapter 1

Introduction

This chapter first presents the research background of the thesis. Different VSC control strategies including Grid-Following (GFL) and Grid-Forming (GFM) control are compared. Then the gap in existing research for HVdc transmission with GFM control is illustrated. Finally, the objectives and outline of the thesis are defined.

1.1 Background

In the modern world, daily human life, industrial manufacturing, and technology development heavily rely on electric power. Electric power systems are also “evolving”. Traditional fossil fuel-based power generation such as coal power plants are quickly and dramatically being replaced by sustainable and renewable power generation such as hydro, wind and solar energy sources. More solar photovoltaic (PV) and battery energy storage systems (BESS) are being installed on the electricity customer’s side, the distribution systems, which usually consume electrical energy, can also generate power to the grid with such distributed energy resources (DERs). DERs are mainly inverter-based resources (IBRs) connected to the electrical grid via power electronics converters, also known as converter-interfaced generations (CIGs). In order to better utilize the DERs, efficient transmission methods such as HVdc transmission is seeing increasing use, adding more IBRs to the grid and likely will become the “backbone” of future power systems. Thus, robust control is required for HVdc and other IBRs as they play an essential part to improve future renewable power system reliability and stability.

1.1.1 Grid-Following and Grid-Forming converter

Today, traditional synchronous-machine-based power systems are quickly transferred into power electronics inverter-based power systems which include HVdc links, static var compensators (SVC/STATCOM), wind, solar photovoltaic (PV) and battery storage energy systems (BESS). For some power systems, the highest hourly penetration of renewable inverter-based resources(IBRs) has reached 95-100%[1][2][6].

The increasing number of power electronics converters in the power system can bring new challenges to maintaining power system stability. Most power electronics converters currently in service rely on fast synchronization with the external grid. A phase-locked loop (PLL) is used to track the phase of the grid ac voltage and the converter switches are operated to produce a voltage of desired magnitude and phase offset relative to the tracked phase angle. In other words, this type of control “follows” the measured grid voltage, and is also referred to as Grid-Following(GFL) control[2][3][4][5]. Most power electronics converters in service today are GFL controlled. They include:

1) Current generation wind turbines, grid-connected PV
2) Most BESS applications
3) Current generation STATCOMs/SVCs
4) LCC (Line-Commutated Converter)-HVdc transmission (uses thyristor switches that can be ordered to turn on but must rely on ac system voltage to reverse bias the valves for turnoff.)
5) Most VSC-HVdc transmission

However, GFL converters struggle to remain synchronized effectively during severe grid events, such as faults or sudden changes in load and/or generation, etc. For LCC-HVdc systems, the normal operation requires connecting a strong ac network; and for VSC-HVdc systems, the PLL gain greatly affects the operation, particularly in a weak grid condition [7]. Moreover, unlike synchronous generators that provide short circuit capacity, inertia and self-synchronization, GFL converters do not do so and make the systems appear to be even weaker.

The grid forming converter (GFM) is becoming more popular and is seeing increased use. Unlike the GFL, which tracks or “follows” an existing bus voltage, the GFM generates or “forms” its own terminal voltage. For example, if a converter is required to supply power to a dead or islanded load, it may be given a sinusoidal three phase voltage reference and would then establish the terminal voltage. Other equipment in the network would then be synchronized to this generated voltage. This has been proposed in the past as a strategy for black starts in networks[8][9].

A special case of the GFM converter occurs when it is designed to mimic the behavior of a synchronous generator, wherein its active power is adjusted proportionally based on the phase difference between the virtual source's phase angle and the system angle. It can allow the converters to provide stability in the controls and maintain synchronized with the external grid during challenging network conditions[2][3][4][5]. So far, GFM is still an ongoing research topic. Some of the pioneer GFM-controlled VSC projects around the world are listed below[5]:

- South Australia Dalrymple Substation Battery GFM project

- Hornsdale Power Reserve GFM BESS ROCOF function test
- The California Imperial Irrigation District BESS project
- Caribbean Island GFM BESS and renewable IBRs study
- Great Britain 69MW Type-4 GFM wind turbine project
- Hawaii GFM BESS with high penetration of renewable DERs study[1]
- East Germany GFM STATCOMs development[10]
- Spain Balearic Islands GFM MMC-HVdc link project[11]

Based on the above real projects, GFM control is mainly used but not limited to the below VSC applications:

1) BESS (most GFM applications)
2) STATCOMs
3) Type-4 wind turbine
4) VSC-HVdc transmission

Table 1-1 shows the comparison of the GFL and GFM converter. Compared with the GFL converter, the GFM converter shows advantages when operating with a weak ac grid and can have black start and island operation capability. Moreover, it has the potential to maintain stable operation when the penetration level of the power electronics converter in the grid is 100% [4]. As the harvesting of renewable energy heavily relies on power electronics converters, GFM becomes an essential technology for integrating more renewable energy resources into the grid and reaching the 2050 Net-Zero emissions [12] goal.

	GFL	GFM
Grid strength requirement	A stable external grid voltage is required.	Can operate with a weak ac system, maintain internal voltage phasor
Black start and island operation	Not applicable	Applicable
Reliance on PLL	Needs PLL or equivalent fast control for synchronization	Intrinsically maintains synchronization by power control

Frequency support	Can provides frequency regulation with extra control to rapidly inject energy	Provides faster energy injection than GFL in the inertial timeframe
Power electronics Converter Penetration level in the grid	Not possible to maintain stable operation at l00% penetration of IBRs	Can operate at 100% penetration of IBRs with some IBRs in GFM

Table 1-1 Comparison of the GFL and GFM converter

1.2 Gaps in existing research

In Section 1.1.1, the basic concept of GFM and its comparison with GFL were presented. Different GFM control strategies have been proposed over the past two decades. They mainly include the following:

1) Droop-Based GFM control [13][14][15][16]: GFM droop control is realized by active and reactive power droop control, it exhibits a linear relationship between frequency and voltage versus active and reactive power.
2) Virtual Synchronous machine (VSM) [17][18][19][20][21]: VSM control emulates the behaviour of Synchronous machines. The VSM model complexity can vary from simplified swing dynamics to detailed electromechanical models.
3) Virtual Oscillator Control[22][23]: Virtual Oscillator GFM control uses a voltage-controlled oscillator to produce a fixed frequency voltage. It can be used to connect the VSC to a dead load where there is no ac source. It can be embellished with Q-V and P-f droop characteristics if other machines are present. The key difference is it uses an oscillator circuit with the nominal ac grid frequency to generate the internal voltage phasor. However, it does not provide sufficient inertia support and the application can be limited [24].

Although there are differences between the above three GFM control strategies, literature [25][26] shows that operating performance of Droop-based GFM and a swing equation-based VSM control is very similar. One aspect of VSM is that it provides the flexibility for the user to select an artificial inertia constant and damping constant which is quite different from that in a real synchronous machine. VSM control is very attractive because it imparts the converter with the characteristic of a synchronous machine with which utility engineers have decades of experience. This thesis therefore concerns itself with VSM type of GFM.

Despite there being some early GFM converter products from original equipment manufacturers (OEMs), GFM control concepts are still in continuing development. In order to take better advantage of the grid forming functionality, such GFM converters require a larger rated current and consequently have oversized IGBT switches [28] compared with GFLs. Also, the fault overcurrent of the basic GFM controlled VSC [17] could be as high as 6 to 7 pu, like that in a real synchronous machine. This could damage the IGBT valves of the VSC whose overcurrent capability is usually below 2 pu [27]. Thus, it is necessary that GFM control be augmented with an overcurrent limiting controller to ride through grid faults. Different overcurrent limiting controls have been proposed mainly including switchable current limiting control[29][30][31], cascade current control[32][33], and virtual impedance control[34][35][36]. However, the fault ride through performance of GFM [37] under various system strength can be different and requires further investigation.

Another development of GFM is to investigate its stability margin with different grid strengths. Literature [38][39][40][41][42] has shown that GFM with overcurrent control can be unstable when connected to a strong ac grid even when it is stable in a weak ac grid. However, how the key control parameters such as inertia constant, damping coefficient and current controller gains affect the system stability under different system needs further investigation. Also, earlier research indicates that it may be necessary to use a different set of gains for strong (large SCR) and weak (low SCR) ac systems, which may be inconvenient when the SCR changes during operation. Thus, it is of great interest to find a single robust set of VSM control parameters which works well over the entire envisaged SCR range.

So far, most of the GFM studies are focused on battery energy storage systems (BESS) in a DER network scenario as shown in the previous sections. There are some early GFM VSC-HVdc transmission studies [11][29][43][44]. However, the inertia support from the GFM VSC cannot be easily determined. Furthermore, manufacturers sometimes “black box" the simulation models of their GFMs making it even more difficult to determine equivalent inertia. Thus, online measurement or simulation-based estimation of the equivalent inertia is of great interest today. The conventional method of inertia measurement in traditional networks is to apply a step change in power generation or consumption to create a frequency disturbance and observe the rate change of frequency (ROCOF) [45][46][47]. However, Due to the fast transient and activation of power-frequency droop control of IBRs, it can be challenging to accurately measure the GFM's inertia using ROCOF. Quantifying the inertia support from a GFM VSC remains unclear and requires further investigation.

1.3 Thesis objectives

Based on the research background and Gaps in existing research, the objectives of the thesis are:

- Investigate Virtual Synchronous Machine (VSM) Grid-Forming (GFM) control disturbance ride-through performance control under different system strength.
- Develop a small signal analytical model to study the proposed VSM controller stability margin with various ac system strength.
- Develop a measurement method to estimate the inertia of GFM IBRs and investigate its frequency support performance connected to a low inertia IBR system.

1.4 Thesis outline

This Thesis is organized as:

Chapter 1 illustrates the research background, gaps in the existing research on GFM VSCs, thesis objectives and outline.

Chapter 2 presents the operation principle and traditional grid-following control of VSC-HVdc transmission. A symmetrical monopole MMC HVdc transmission system with practical specifications is developed in the electromagnetic transients (EMT) simulation program PSCAD/EMTDC.

Chapter 3 investigates the dynamic behaviour of VSM and compares that with a synchronous machine and GFL VSC. The performance of two VSM overcurrent limiting control fault ride through capabilities are compared and evaluated by EMT simulation. An adaptive control mode on dynamically changing its power order and damping coefficient is proposed to improve VSM disturbance ride through capability connected to strong ac systems.

Chapter 4 develops the linearized analytical model of VSM. The model is validated with EMT simulation. The control stability margin of VSM with and without a current limiting loop under various grid conditions are investigated. A suitable range of VSM key control parameters that is stable when connected to strong or weak system is proposed.

Chapter 5 proposes a new inertia measurement method for IBRs system based on harmonic injection which allows inertia determination without applying a large power imbalance disturbance, as is done when using the conventional RoCoF estimation method. Using EMT simulation, the performance of the proposed inertia measurement method is first validated with the example of a synchronous machine with known inertia. It is then extended to analyze the inertia response of a network with a mix of other IBRs, VSMs and SMs. The thesis shows the proposed inertia measurement method is a convenient tool to quantify the inertia support from VSMs and total equivalent IBR system inertia.

Chapter 6 summarizes the thesis, including the conclusion and future work.

Chapter 2

Operating Principles & Grid-following Control of a VSC-HVdc Transmission System

This chapter describes operating principles and the traditional grid-following control strategy for a VSC-HVdc transmission system. An EMT model of a VSC-HVdc link with practical ratings and system parameters in the range of real systems of similar ratings is developed using the EMT simulator PSCAD/EMTDC. The VSC-HVdc EMT model developed in this chapter will be used as a platform for the study in the later chapters of the thesis.

2.1 VSC-HVdc converter topologies

Mercury valves were used for early HVdc transmission converters [49][50]. The world's first commercial HVdc link using Mercury valves was built between mainland Sweden and Gotland Island in 1954 and eventually expanded in capacity and upgraded to thyristor valves between 1970 and 1987. The main problem with mercury valves was the ark-back fault which can destroy the rectifier valves and cause other issues [51]. This problem had been solved with the development of thyristor valves in the 1960s. In 1972, the first application of the HVdc system using thyristor valves was built at Eel River, providing an asynchronous connection between Quebec and New Brunswick.

The characteristic of the "on" and "off" state of thyristors is close to an ideal switch. In high voltage applications, thyristors are connected in series to share the high voltage and controlled as a single device. This arrangement is called a "thyristor valve". When a positive voltage bias is applied between the gate and the cathode, the thyristor can be turned with the application of a small positive voltage (firing pulse) between the gate and cathode. However, a reverse line to line voltage across the anode and cathode of the off-going valve is required for it to reach the "off" state and commutate the current into the next valve in the conduction sequence which was given the "on" firing pulse. Therefore, HVdc converters using Thyristor valves are called Line-Commutated Converters (LCC).

The primary limitation of LCC-HVdc is its requirement for a relatively stiff ac grid voltage i.e., a high Short-Circuit Ratio (SCR), to ensure successful commutation. However, this requirement may not always be met in the future grid, as the growing presence of renewable energy sources in the form of inverter-based resources (IBRs) can potentially reduce the equivalent Short-Circuit Ratio (SCR) of the connected ac system. With a weak ac system, the grid side voltage can easily fluctuate as the loading changes and could precipitate comm fail. A sudden active power change can also cause high temporary overvoltage (TOV) [52][53]. Also, the low-order harmonic resonance between a weak ac system and ac filters [54] can distort ac bus voltage. Additionally, the operation of an LCC Converter also demands a considerable supply of reactive power from the ac network.

Unlike the thyristor valves used in the LCC, which can only be controlled to turn on with a firing pulse, the Voltage Source Converter (VSC) uses self-commutating semiconductor switches such as Insulated Gate Bipolar Transistors (IGBTs). These switches can not only be turned on similar to a thyristor but also be ordered to turn off with a gate turnoff pulse. Hence, VSC-HVdc does not suffer from commutation failure, is flexible on power reversal, can provide reactive power support and can operate with weak ac grids. The first VSC-HVdc transmission scheme, commercially called "HVDC Light" was first commissioned in Sweden by ABB in the late 1990s [8].

For VSC-HVdc transmission, three topologies are mainly used: 2-level VSC, 3-level NPC (Neutral-Point Clamped) VSC and MMC (Modular Multilevel Converter).

2.1.1 Two-level VSC

Figure 2-1 shows the configuration of the IGBT modules in a 2-level VSC bridge, an anti-parallel diode is connected to the IGBT for the reverse current path. For high voltage applications, several IGBTs may be connected in series constituting an IGBT valve. The same firing pulses are given inside each valve. There is a total of 6 IGBT valves for a two-level VSC converter or inverter bridge. A bipolar sinusoidal PWM (SPWM) [55][95] shown in Figure 2-2 is usually used to generate firing pulses. In this approach, a sinusoidal modulating signal v_m at fundamental frequency f_m is compared with a triangular carrier signal v_c at frequency f_c, and firing pulses are issued at the intersection of v_m and v_c. More sophisticated modulation methods are also possible but not discussed here. The resulting VSC output is the bipolar PWM signal, whose harmonic spectrum contains a sinusoidal signal proportional to the modulating wave's amplitude and in phase with it. Harmonic components are moved to easy-to-filter at higher frequencies clustered around f_c. In some high voltage level applications, the highest voltage rating switches are selected for two-level VSC, requiring a large number of series devices in each valve. However, a major issue in this approach is the need for precise simultaneous firing pulses for the myriad of IGBT switches in the valve and the lossy snubber circuits for the switches to guarantee equal voltage sharing among the IGBTs [59].

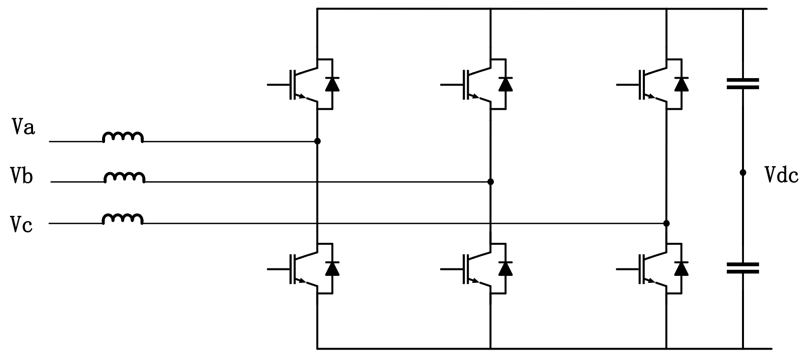

Figure 2-1 two-level VSC bridge

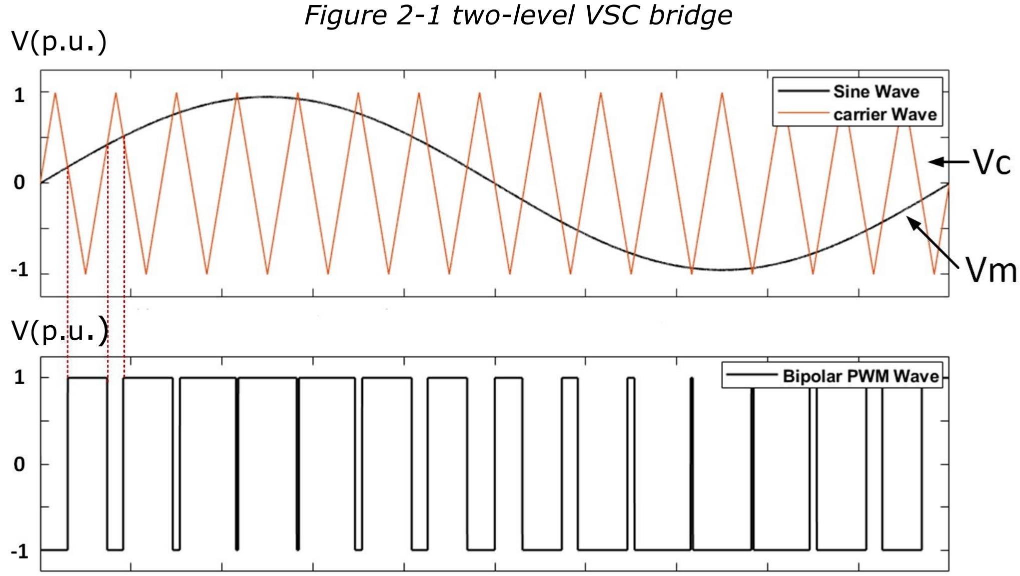

Figure 2-2 Bipolar PWM

2.1.2 Three-level NPC-VSC

Another approach for high-voltage applications is to use multilevel converters to reduce the number of series-connected switches. Figure 2-3 shows the configuration of the IGBT modules in a 3-level Neutral Point Clamped (NPC)-VSC bridge [58]. Here, the withstand voltage of each switching cell is half of the dc voltage. Moreover, NPC-VSC can reduce harmonics and lower switching loss compared with two-level VSC [61]. A unipolar SPWM [55] shown in Figure 2-4 is usually used to generate firing pulses. Compared with bipolar PWM, unipolar PWM and SVM have higher efficiency and lower THD (Total Harmonic Distortion). Sometimes Space Vector Modulation (SVM) [56][57] is also used. In SVM, the three-phase voltage waveform is represented by a rotating vector called the space vector. The magnitude and angle of the space vector represent the amplitude and phase angle of the voltage waveform, respectively. By manipulating the magnitude and angle of the space vector, the inverter output voltage can be controlled. However, the neutral-clamped diodes can make the insulation and cooling design of the converter complicated. Therefore, higher-level NPC topologies are not considered for HVDC applications [62].

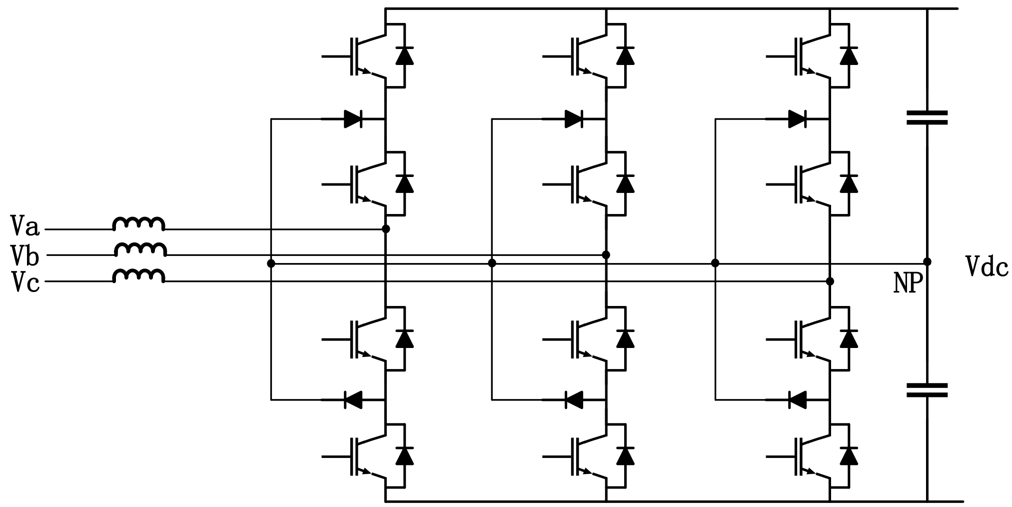

Figure 2-3 Three-level NPC bridge

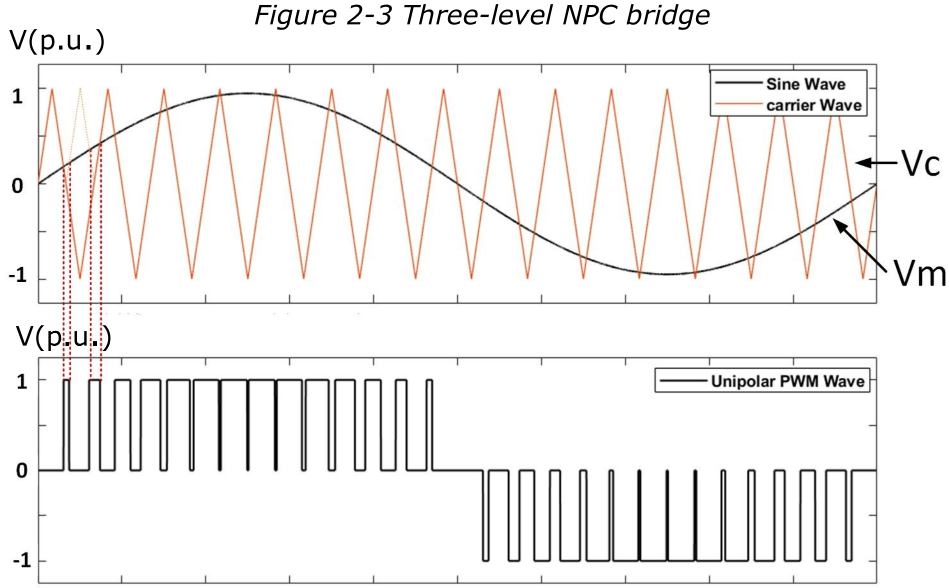

Figure 2-4 Unipolar PWM

2.1.3 Modular Multilevel VSC

The Multilevel converters approach can be further extended to the Modular Multilevel Converter (MMC) concept [63][64]. MMC with full-bridge submodules was used in the 1990s for static var compensator (STATCOM) for reactive power compensation [65][66], but not for HVdc transmission until 2002, which used half-bridge sub-modules [64]. By stacking identical low voltage rating submodules in series connection, MMC can be scaled to high voltage rating applications, such as offshore and onshore HVdc transmissions as well as HVdc grids in future [67]. Compared with two-level VSC and three-level NPC-

VSC, the most distinctive advantage of the MMC is that a very high voltage rating with excellent harmonic performance can be achieved at a low switching frequency, and thus, reducing the switching losses. Figure 2-5 shows an MMC bridge with a half-bridge submodule configuration.

No matter what topology is used for VSC-HVdc transmission, the converter is controlled as a voltage source. This is different from the LCC-HVdc converter which usually has a large dc side inductance, and so acts in the short period as a current source. The VSC control system can regulate the magnitude, frequency and phase angle of the converter output ac voltage waveform and make it either "follow" the external ac grid or "form" the ac grid to behave like synchronous machines when necessary. This extra control freedom of VSC-HVdc is attractive for future power systems since it could offer solutions to maintain the system stability in challenging network conditions.

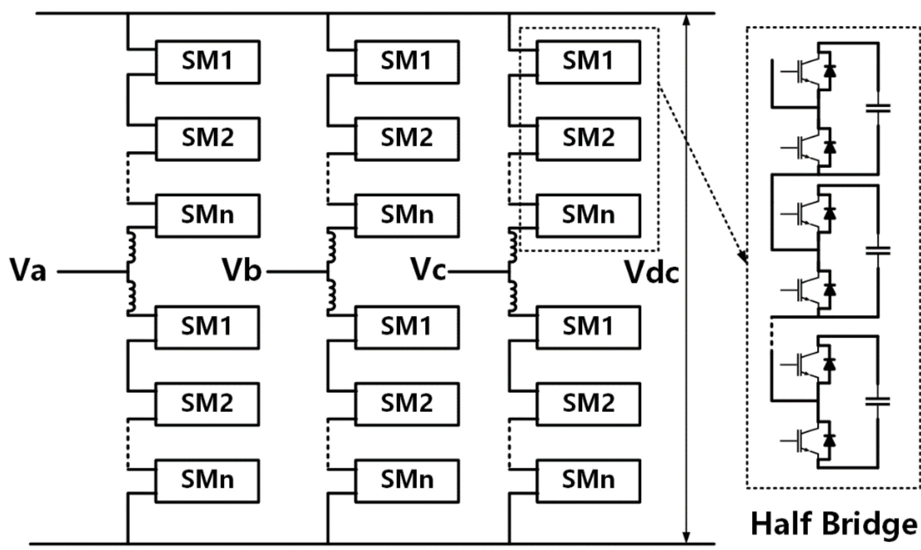

Figure 2-5 An MMC bridge (with a half-bridge submodule configuration)

2.2 Main circuit components of an MMC-HVdc system

Different VSC topologies are briefly introduced in Section 2.1. The advantages, such as built-in redundancy, higher efficiency, and lower harmonics, make MMC technology dominant in most of the new VSC-HVdc applications these days. In this and the following sections, the discussion of VSC-HVdc transmission will be focused on MMC-VSC.

The MMC-HVdc converter has monopolar and bipolar configurations. The monopolar configuration includes the symmetrical monopole, asymmetrical monopole with a metallic return, and symmetrical monopole with a ground electrode return as shown in Figure 2-6. The majority of monopolar VSC-based HVDC systems to date utilize the symmetrical configuration [60]. The bipolar configuration includes bipolar with a ground return and bipolar with a metallic return as shown in Figure 2-6. The main advantage of bipolar configuration is to improve system reliability. In the event of a converter or cable failure at one pole, the system can still operate with 50% of the transmission capacity from the healthy pole. To simplify the discussion, a symmetrical monopole configuration shown in Figure 2-7 will be used for later studies in this thesis, although the conclusions will be generally applicable to the other configurations.

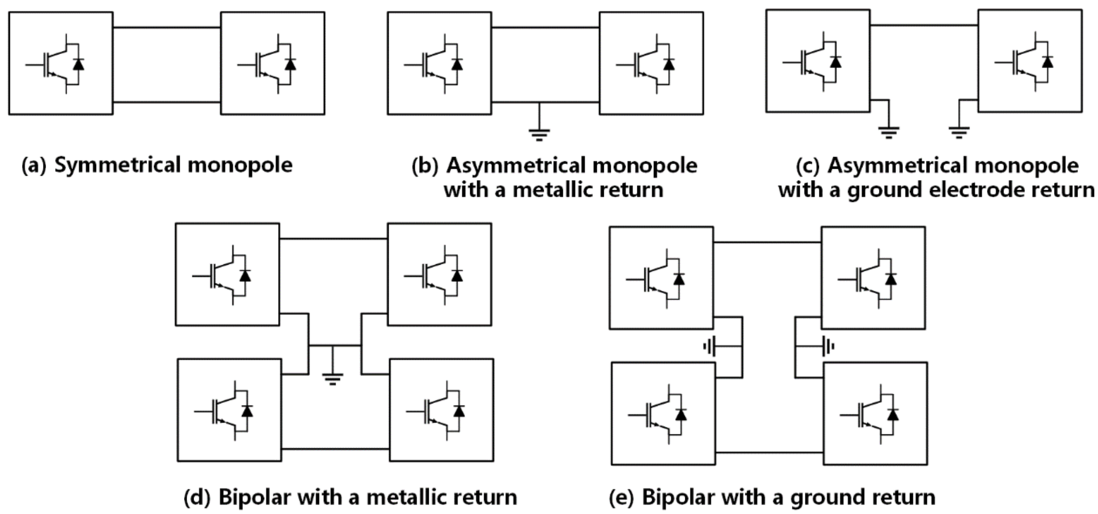

Figure 2-6 MMC station configurations

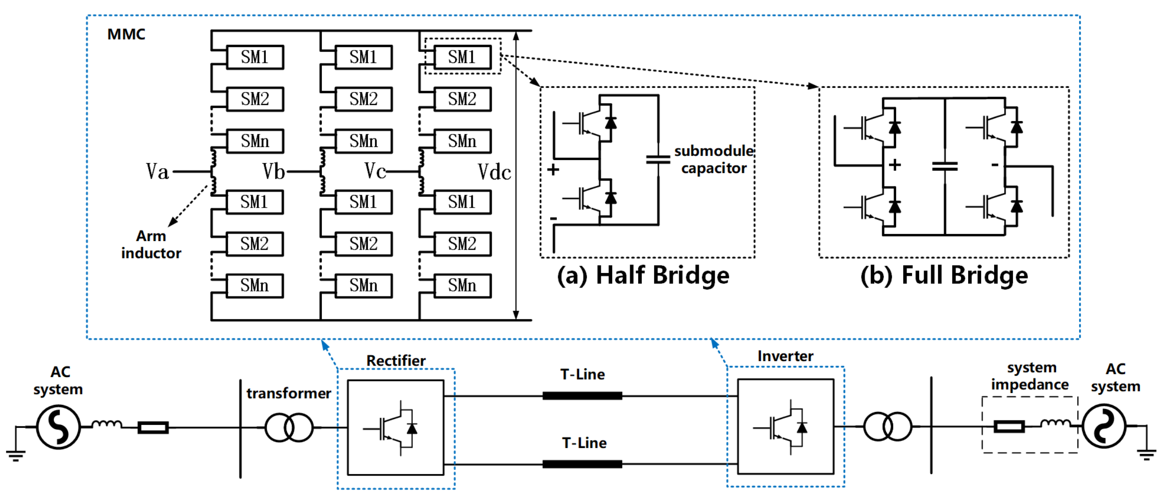

Figure 2-7 A symmetrical monopole MMC VSC-HVdc link

In the following sections, the circuit components of MMC viz., submodules, submodule capacitors and arm inductors are discussed.

2.2.1 Submodule configuration

The submodules of the MMC VSC-HVdc link shown in Figure 2-7 can be a half-bridge or full-bridge configuration (as shown in the inset). The half-bridge submodule has one two-level phase leg in parallel with the dc capacitor, and the output is taken at the junction of the two IGBT switches. In contrast, the full-bridge submodule has two switch legs in parallel to the dc capacitor; the external terminals are as shown in the inset in Figure 2-7. The full-bridge configuration has more flexibility in control as the submodule voltage can not only be added (as is the case for the half bridge), but also subtracted from that of the other submodules. It can also withstand higher ac voltages due to two IGBTs always being in series. The reverse voltage can help to mitigate the short circuit current from pole faults [69]. However, the disadvantage is that the increased number of semiconductor switches also results in a larger power loss in the converter. Since the half-bridge submodule configuration is almost universally used in erstwhile MMC-HVdc transmission schemes [60] in this thesis we consider only MMCs with half-bridge submodules.

Series connection of submodules forms submodule strings of each converter arm. For a string of N submodules, half-bridge submodules can have a total of N+1 voltage levels (N level and zero). Figure 2-8 shows the ac voltage reference and MMC output waveform for a 11-level half-bridge MMC. In high voltage applications, as the number of submodules can increase to hundreds to handle the high voltage, the MMC output voltage waveform has an extremely low harmonic content and can be considered to be sinusoidal. Thus, the ac filters which are mandatory for the LCC and 2 level-VSC are not necessary for the MMC.

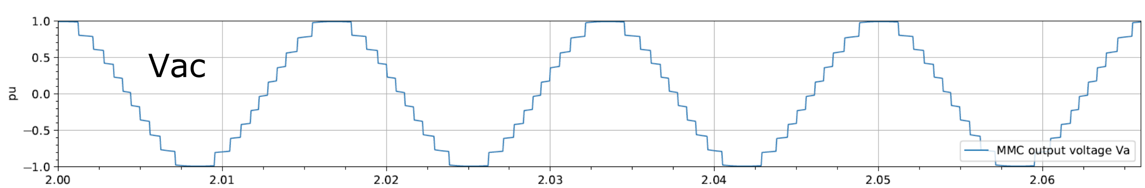

Figure 2-8 A 11-level Half-bridge MMC output ac voltage waveform

2.2.2 Submodule capacitors

Since the dc capacitors of MMC can be distributed in each submodule, the common dc capacitor is superfluous on the dc side. Moreover, the total energy stored in the MMC dc capacitors is larger, which gives extra freedom for the control system to offer auxiliary grid services such as dc fault fast recovery [68] or low-frequency power oscillation damping [70].

Typically, the submodule capacitance is chosen such that the total stored energy in all submodule capacitors of the converter E_{MMC} divided by the converter's rated MVA S_{MVA} is approximately $\tau = 30\ kJ/MVA$ to $40\ kJ/MVA$ (i.e., 30 ms to 40 ms) [79][80]. For a given value of τ the submodule capacitance C_{sub} can be calculated by (2.1); where N is the number of submodules in each converter arm (neglecting the redundant and faulted submodules), and v_{dc} is the total pole to pole dc voltage.

$$\tau = \frac{E_{MMC}}{S_{MVA}} = \frac{6 \cdot (\frac{1}{2} \cdot N \cdot C_{sub} \cdot \frac{v_{dc}^2}{N^2})}{S_{MVA}} \Rightarrow C_{sub} = \frac{\tau N S_{MVA}}{3 v_{dc}^2} \tag{2.1}$$

2.2.3 Arm inductors

The arm inductors of an MMC are typically dry-type air-core reactors [81]. The main purpose of the arm inductance is to filter high-frequency harmonics and smoothen the circulating current in the MMC. The arm inductors also help to limit the fault current flows from the ac to the dc side when a dc fault happens, thus, protecting the anti-parallel diodes of submodules. A typical arm inductance value is usually 0.1 pu to 0.15 pu [60] based on the converter's valve side voltage and MVA ratings.

2.3 Control of the VSC-HVdc system

The control of the VSC-HVdc in each converter station can be hierarchically divided into station dispatch controls, upper-level controls, and lower-level controls. At the station dispatch control level, the system operator issues the reference commands (e.g., P_{ref}, Q_{ref}, V_{acref}) for the upper-level controls. The upper-level controller takes in the orders from the dispatch controller and generates the d and q-axis current orders, then issues the d and q-axis voltage references (V_{dref} and V_{qref}) for each VSC pole. These are converted to the three-phase ac voltage references for the lower-level controller. Finally, the lower-level controls, which are specific to the valve topologies (2-level, 3-level VSC or MMC), generate the switching pulses to the IGBTs to achieve the ordered voltage. In the following sections, the details of upper-level controls and lower-level controls are discussed.

2.3.1 Upper-level controls

Depending on the type of connected ac system, the traditional VSC upper-level control can be customized for:

1) islanded control with passive load or limited generation,
2) non-islanded control, where the converter feeds a system with active synchronous generators or is connected to the wider ac grid.

Islanded control is also used when the VSC-HVdc converters are connected to a weak ac system or for black starting the ac system. In these situations, the VSC converter can actively control the ac system frequency and voltage. Figure 2-9 shows a control diagram of the islanded control. A voltage-controlled oscillator (VCO) generates the synchronization angle θ from the frequency reference ω_{ref}, and a proportional integral (PI) controller regulates the ac voltage magnitude. Note that, when the VSC is connected to an ac system with some synchronous generation, an $\omega - P$ droop D_p can be added to coordinate the power sharing between the VSC and ac generation, where the frequency is linearly varied as a function of the power injected to the ac system. Islanded control is an early version of "grid-forming (GFM)" [75] but has its limitation when the synchronous generation in the ac system becomes comparatively large. In later chapters, Virtual synchronous machine (VSM) type grid-forming control is shown to be a solution to this problem.

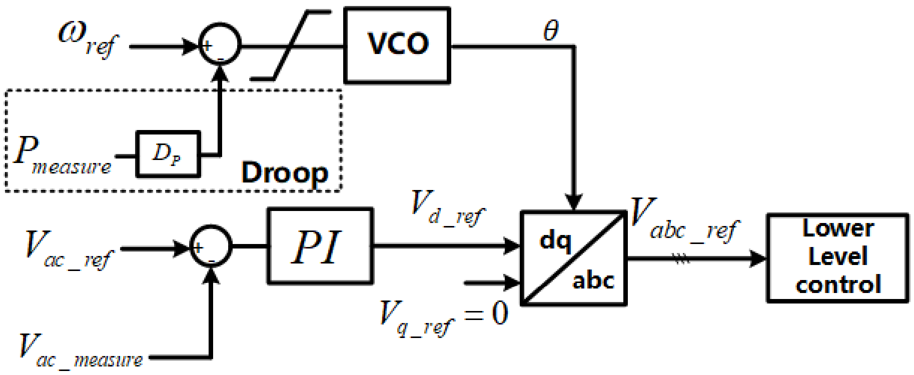

Figure 2-9 islanded control diagram of VSC-HVdc ("early grid-forming")

Non-islanded control typically transfers a three-phase VSC system into dq frame through Park's transformation [85]. A Phase-locked loop (PLL) [94] shown in Figure 2-10 is to obtain the synchronization angle θ from the ac system voltage for the transformation. Since the control relies on the PLL and "follows" the ac system voltage to synchronize to the connected ac system, it is also referred to as "grid-following (GFL) control" [2][3][4][5]. When connected to the weak ac system, it is challenging for the VSC to maintain synchronized in GFL control. The VSC may need to change from GFL control to GFM control for stable operation.

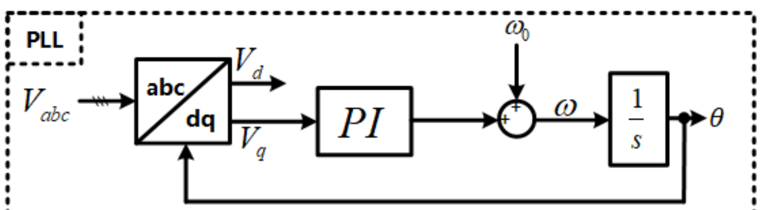

Figure 2-10 Phase-Locked Loop (PLL) control diagram

The VSC grid-following control diagram is shown in Figure 2-11. The control is decoupled into two loops in dq frame. In this thesis, the active power and dc voltage control are associated with the d-axis, while the ac voltage control and reactive control are associated with q axis. They generate the current reference I_{d1_ref} and I_{q1_ref} to the current controller. Inserting a current controller in tandem with the active power/dc voltage/reactive power/ac voltage controller allows one to limit the overcurrent by imposing maximum limits on the magnitudes of I_{dref} and I_{qref}.

2.3.1.1 Active power and dc voltage control

For a point-to-point VSC-HVdc link, one converter station should control the dc link voltage, and the other controls the transmitted active power. The active power controller regulates the VSC active power output and dc link voltage via I_{dref}. Similarly, the dc voltage controller regulates the dc side voltage and also uses I_{dref} to increase or decrease the active power into the dc side to boost or buck the dc voltage. For a multi-terminal VSC-HVdc grid, at least one converter station should take over the dc voltage control, while the other stations control the active power output at each station.

2.3.1.2 Reactive power and ac voltage control

Depending on the connected ac system's requirement, the VSC station can be selected to regulate the reactive power or alternatively the ac voltage at the point of common coupling (PCC) bus. The reactive power (or, alternatively ac voltage) controller operates by controlling the VSC's reactive current reference I_{qref}.

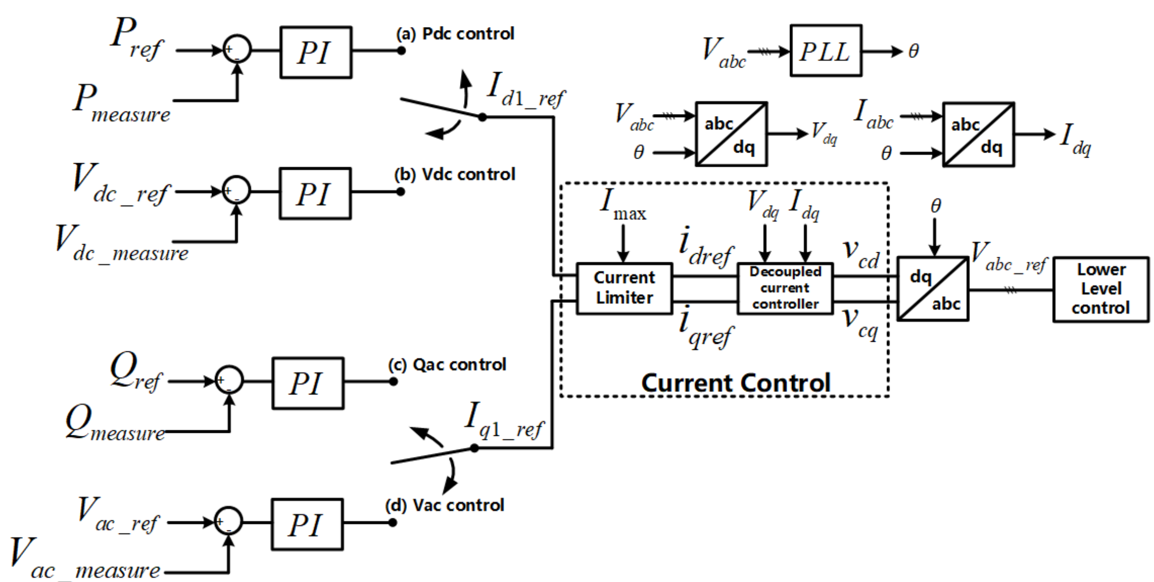

Figure 2-11 Grid-following control diagram of VSC-HVdc (a) active power control (b) dc voltage control (c) reactive power control (d) ac voltage control

2.3.1.3 Current control

Figure 2-12 shows the current controller diagram. The main purpose of the current control is to limit the converter current output during the fault, and thus protection the IGBTs. The current controller reference I_{d1_ref} and I_{q1_ref} generated from the controls in Section 2.2.2.1.1 and 2.2.2.1.2 first go through a current limiter. If the intention is to regulate the maximum current magnitude I_{max}, I_{dref_max} and I_{qref_max} are chosen such that $I_{dref\_max}^2 + I_{qref\_max}^2 = I_{max}^2$. However, to ride through faults, priority can be given to either the active or reactive currents [82][83][84]. For example, if the maximum allowed current magnitude during the fault is I_{max}, and the priority is given to active current on d-axis, then,

$$\begin{aligned} I_{dref\_\max} &= I_{\max}, I_{dref\_\min} = -I_{\max} \\ I_{qref\_\max} &= \sqrt{I_{\max}^2 - I_{dref\_\max}^2}, I_{qref\_\min} = -\sqrt{I_{\max}^2 - I_{dref\_\max}^2} \end{aligned} \tag{2.2}$$

If the priority is given to the reactive current on q-axis, then,

$$\begin{aligned} I_{qref\_\max} &= I_{\max}, I_{qref\_\min} = -I_{\max} \\ I_{dref\_\max} &= \sqrt{I_{\max}^2 - I_{qref\_\max}^2}, I_{dref\_\min} = -\sqrt{I_{\max}^2 - I_{qref\_\max}^2} \end{aligned} \tag{2.3}$$

The current references I_{dref} and I_{qref} after (application of any maximum limits by the current limiting function) are passed to a decoupled current controller that generates the voltage orders v_{cd} and v_{cq} for the VSC so that the ordered currents are indeed achieved as shown in Figure 2-12. The terms v_{td} and v_{tq} represent the d and q-axis voltages of the PCC, and ωL is the reactance between converter valves to the PCC bus. Including the v_{td} and v_{tq} helps in improving the ac disturbance rejection capability for the converter [59]. The feedforward terms $-\omega L i_q$ and $\omega L i_d$ help decouple the dynamics of i_q and i_d on d and q-axis controls, respectively, i.e., if a change in i_{dref} only results in a change in i_d with no transient in i_q, and likewise for a change in i_{qref}.

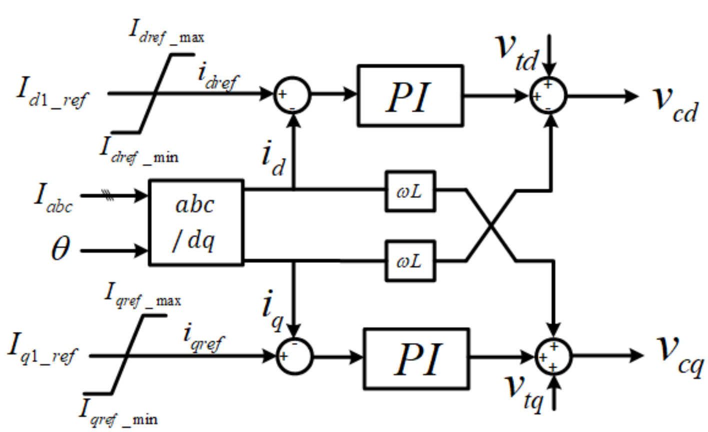

Figure 2-12 Current control diagram

2.3.2 Lower-level controls

The lower-level controls of MMC include a firing pulse modulation controller and a Circulating Current Suppression Controller (CCSC). Although the discussion of GFL and GFM control in the later chapters of this thesis is mainly focused on the upper-level control strategy of MMC, the common lower-level controls in MMC will be briefly introduced here.

2.3.2.1 Firing pulse generation

To generate the firing pulse of the output voltage waveform, there are several modulation techniques which can be used. The commonly used method for the MMC is "Nearest Level Control (NLC)" [74][76][77]. Given a desired sinusoidal modulation signal v_m which is from Upper-level controls, the aim of NLC is to generate a near-sinusoidal stepped waveform which is shown in Figure 2-8. In NLC, initially, the voltage amplitude v_{sm} for each desired level is pre-calculated based on the number of inserted submodules. Then, the reference voltage v_m for modulation is discretized with the step that equals the pre-calculated voltage amplitude v_{sm}, so that the number of submodules required for switching is estimated. Finally, a sorting and balancing algorithm is applied to select the submodules given switching signals. This ensures the capacitor of each submodule has equal opportunities for charging or discharging and thus maintains the average voltage of each submodule's capacitor. Other modulation techniques which have been proposed include Phase-Disposition Modulation (PD-PWM)[71], Phase-Shift Modulation (PS-PWM)[72], Space-Vector Modulation (SV-PWM)[8], and the improved Selective Harmonic Elimination method (SHE)[73][74]. However, as the number of levels increases in MMCs, PWM and SHE techniques become cumbersome [9].

2.3.2.2 Circulating current suppression control (CCSC)

If no special steps are taken, then, in addition to the dc component, the arm currents of the MMC can contain harmonics of even orders that do not enter the ac side, but circulate among the three bridge legs (each leg current is contributed equally from 2 arms, the upper and bottom arms) [60][9]. The presence of these even harmonics amplifies the current rating of the IGBT switches and contributes to additional power losses. The 2nd harmonic is the dominant component in the arm current harmonics and needs to be eliminated. Adding a second-harmonic elimination controller is an economical way to do this in comparison with the alternative option of adding 2nd harmonic blocking filter. Figure 2-13 shows the control diagram of such a "Circulating Current Suppression Controller (CCSC)". I_{Uabc} and I_{Babc} are the three-phase current in the upper and bottom MMC arms. The 2nd harmonic current i_{zabc} can be obtained as:

$$i_{zabc} = \frac{i_{Uabc} + i_{Babc}}{2} \tag{2.4}$$

Then, i_{zabc} can be transferred to the dq frame as i_{zd} and i_{zq}. A second harmonic controller acts on the error between these signals and their corresponding references I_{zdref} and I_{zqref}. It generates, firstly the d and q components of the required ac voltage and finally, on conversion to phase quantities, the corresponding additions V_{zabc_ref} to the three-phase modulation voltage signals V_{abc_ref} to yield the modulation signals $V_{abc\_ref\_U}$ and $V_{abc\_ref\_B}$ for the upper and lower arms. This produces 2nd harmonic voltage components in each arm, which cancel the circulating 2nd harmonic current. However, due to equal injections in each arm, the second harmonic does not appear on the ac side voltage. The references I_{zdref} and I_{zqref} are set to zero, as total annihilation is the goal.

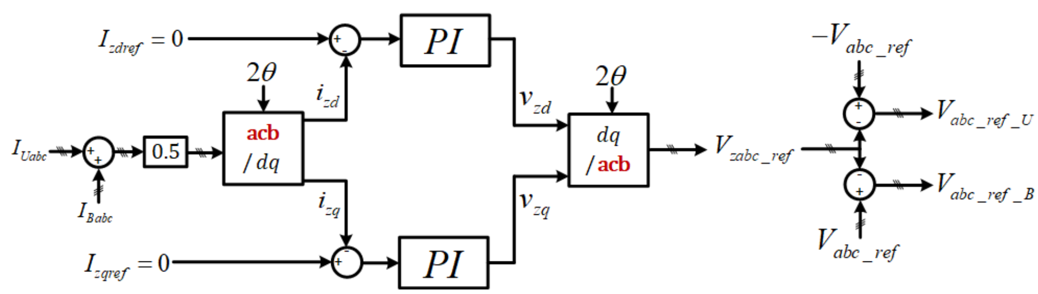

Figure 2-13 CCSC diagram

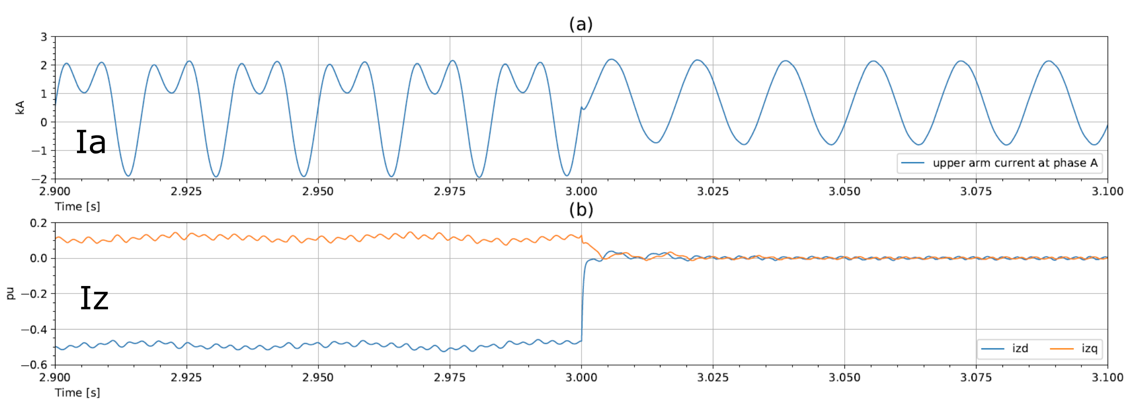

Figure 2-14 (a) The upper arm current in phase A (b) i_{zd} and i_{zq}

Figure 2-14 shows the EMT simulation waveforms of (a) the upper arm current in phase A as well as (b) i_{zd} and i_{zq} components. When CCSC is enabled at 3 s, the arm current contains essentially only the dc and fundamental frequency components, and i_{zd} and i_{zq} are controlled to zero, demonstrating the effectiveness of the CCSC.

2.4 EMT simulation for MMC VSC-HVdc system

In this section, the symmetrical monopole MMC-HVdc system shown in Figure 2-7 and with controls as in Figure 2-11 and Figure 2-13 is developed in PSCAD/EMTDC with parameters consistent with a realistic system. The transmission line structure and parameters are for an 806-A4-61 all aluminum alloy conductor (AAAC) configuration [78] shown in Figure 2-15. Other system control parameters and specifications are shown below in Table 2-1 and Table 2-2.

PLL gain (K_{ppll}, K_{ipll})	(300, 200)
Active power controller (K_{pp}, K_{ip})	(0.5, 0.1)
Dc voltage controller (K_{pdc}, K_{idc})	(10, 0.1)
Ac voltage controller (K_{pac}, K_{iac})	(1, 0.1)
Inner current control (K_{pi}, K_{ii})	(1, 0.01)
CCSC controller (K_{pccsc}, K_{iccsc})	(0.8, 0.01)

Table 2-1 MMC control parameters

MMC pole configuration	symmetrical monopole
DC link voltage	+/- 250 kV
Rated power	1000 MVA
MMC submodule number in each arm	200
Submodule capacitance	10.6 mF
transformer winding voltage	230kV/250kV
Transformer leakage reactance	0.18 pu
Arm inductor	24 mH
Transmission length	800km

Rated ac system voltage	230 kV, 60Hz
Ac system strength (short circuit ratio)	2.5

Table 2-2 MMC system specifications

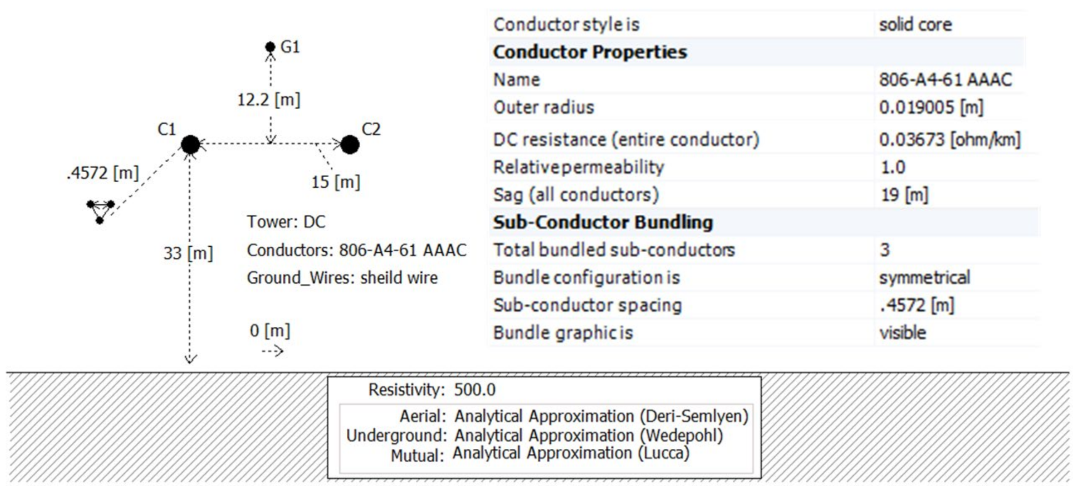

Figure 2-15 Transmission line configuration and parameters

The rectifier side VSC station controls the dc link voltage and the inverter side VSC station controls the active power output at 900MW to the ac system. Both the rectifier and inverter stations operate in ac voltage control mode. In the EMT simulation, a solid three-phase to ground fault is applied first on the inverter ac bus at 5 s, then on the rectifier ac bus at 9 s. The duration of both fault contingencies is 0.083 s (5 cycles in a 60 Hz system). Figure 2-16 shows the EMT simulation results of (a) measured active power at the rectifier and inverter ac bus, (b) measured reactive power at the rectifier and inverter ac bus, (c) pole to pole dc voltage, (d) ac voltage at rectifier and inverter as bus and (e) ac current flows from each VSC station to the ac system. For the fault current limiting, the maximum allowed current is 1.3 pu (4.6 kA) with priority on i_d, showing that current limiting is working properly. The system recovers to 80% power in 77 ms after the fault clears on the inverter ac bus. For the rectifier side ac fault, it recovers in 157 ms. This is because the terminal that controls the dc voltage is responsible for maintaining a stable dc voltage level across the dc link. In the event of an ac fault, the dc voltage can fluctuate, and the terminal needs to respond to stabilize the voltage level. The control strategy for this terminal will require a longer fault recovery time to ensure stable dc voltage recovery after the fault.

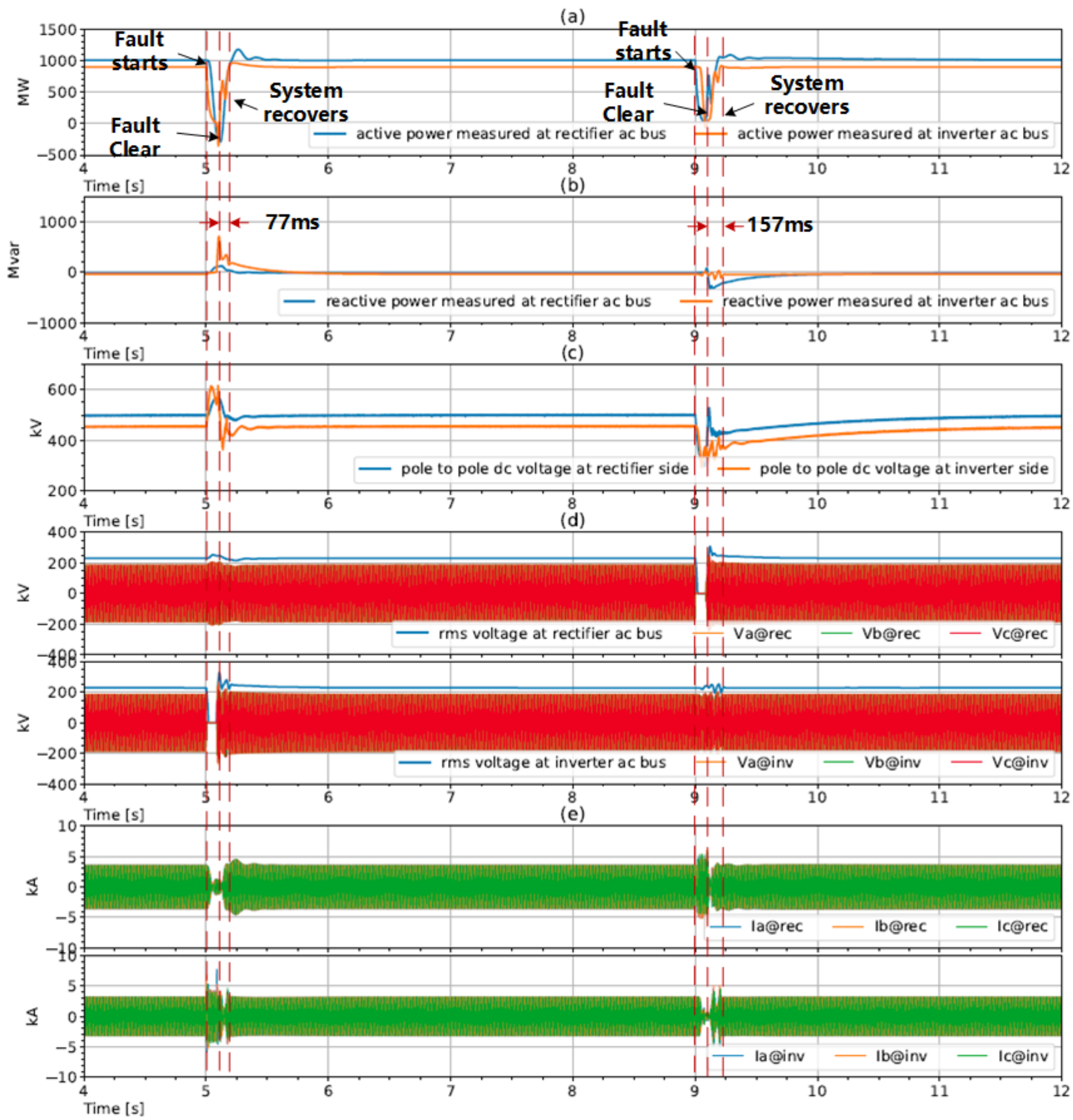

Figure 2-16 The MMC-HVdc link (a) active power (b) reactive power (c) dc voltage (d) ac voltage (e) ac current

2.5 Summary

This chapter discusses the operating principles and control of VSC-HVdc transmission systems. A symmetrical monopole MMC HVdc transmission system is developed in the EMT simulator PSCAD/EMTDC, whose basic structure will be used in future chapters. The developed HVdc systems can survive the solid three-phase to ground fault on each converter terminal with good dynamic performance, and thus the model is validated for the study in later chapters.

Chapter 3

Virtual Synchronous Machine Grid-Forming Control on VSC

This chapter presents the Virtual Synchronous Machine (VSM) Grid-Forming control strategy for the VSC-HVdc converter. Initially, the control strategy of VSM is introduced. Then, a test system is modelled on the EMT simulator PSCAD/EMTDC for implementing VSM control. The VSM dynamic response is compared with that of a synchronous machine and GFL converter. Next, two overcurrent limiting control methods of VSM, switchable and in-line cascaded current limiting control, are discussed. Their limitation when applied to a VSM connected to a strong ac system are revealed. Finally, an adaptive fault ride through method on VSM control is proposed to improve its disturbance ride through performance.

3.1 VSM control

As mentioned previously in Chapter 1, Section 1.2, A VSM can control the converter so that its behaviour is akin to that of a synchronous generator which generates the ac voltage phase angle reference itself and adjusts its real power in proportion according to the (sine of the) phase angle difference between the virtual source and the ac network's Thevenin equivalent source. Figure 3-1 shows the equivalence between a VSC converter station and a synchronous machine (SM). A prime mover whose speed is controlled by a governor is the mechanical input power source for the SM. In the same way, if a VSC is made to mimic the SM, its source of input power is the dc side rectifier or dc grid. The SM generates an internal voltage in proportion to its field current which is controlled by an excitation system. Its speed though nominally controlled by the governor, is transiently dependent on the accelerating power applied to its mechanical inertia. In the VSM, the control system mimics the electromechanical behaviour of the actual SM's electromechanical dynamics.

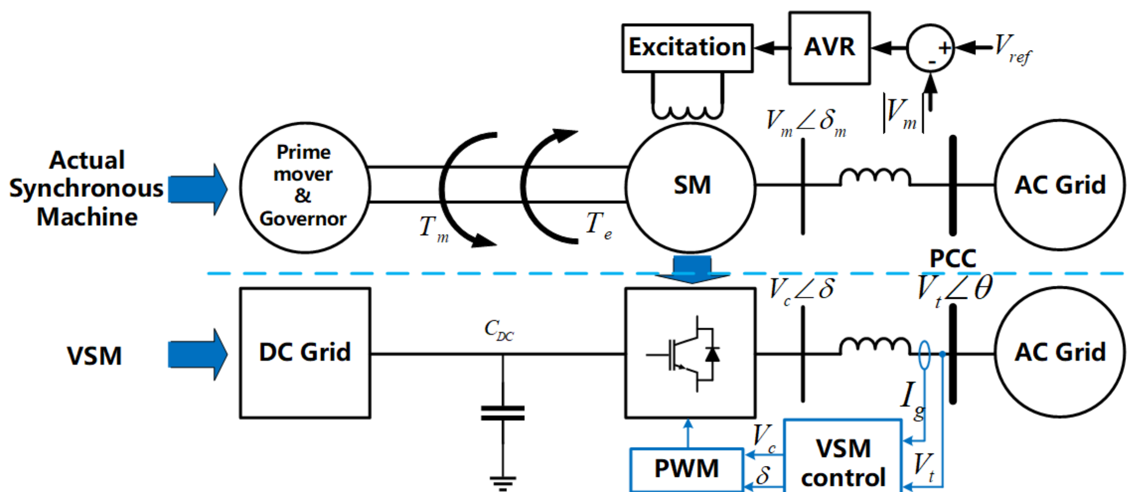

Figure 3-1 Equivalent between a VSM VSC station and Synchronous Machine

Various VSM models [17][18][19][20][21] have been proposed to emulate the behaviour of the real synchronous machine with different levels of accuracy, however, higher order synchronous machine model emulation could bring more undamped control interactions between different VSM VSC and increase the difficulty of controller design [19]. In this project, the discussion of VSM will focus on simplified synchronous machine emulation. The swing equation of a synchronous machine is used to regulate the power from the converter as expressed by equation (3.1).

$$J\ddot{\theta} = T_m - T_e - D\Delta\dot{\theta} = \frac{P_m}{\omega} - \frac{P_e}{\omega} - D\Delta\dot{\theta} \tag{3.1}$$

In equation(3.1), ω is the synchronous angular velocity, and θ is the synchronous phase angle. The mechanical power P_m of the synchronous machine is equivalent to the power order reference of the converter, and the electrical torque electrical power P_e is equivalent to the measurement of power at the PCC (point of common coupling). The mechanical torque T_m and electrical torque T_e are proportional to the corresponding mechanical and electrical powers, i.e., $Tm = P_m/\omega$, etc., but for a machine running close to synchronous speed as is the usual condition, $P_m \approx T_m$ and $P_e \approx T_e$ in per unit. J is the inertia constant and D is the damping coefficient. Note that, inertia and damping in a VSM are synthetic and can even be changed adaptively. This is different from a real synchronous machine where the inertia and damping are inherently due to the rotational mass, damper winding parameters, mechanical friction and windage loss; and can not therefore be arbitrarily selected. However, VSM does not have such a constraint and can offer extra control flexibility, including the possibility of adaptively changing these constants when in operation. More illustration of the dynamic response of different inertia and damping of VSM is shown by the EMT simulation in Section 3.2.1.

Figure 3-2 shows the VSM control diagram. The power synchronization loop emulates the swing equation of a synchronous machine. It generates the ac voltage synchronization angle θ at the PCC. It must be stressed that there is another mechanical damping coefficient D_m which accounts for the mechanical rotational loss due to mechanical windage and friction. However, the effect of D_m can be incorporated into the value of the damping coefficient D.

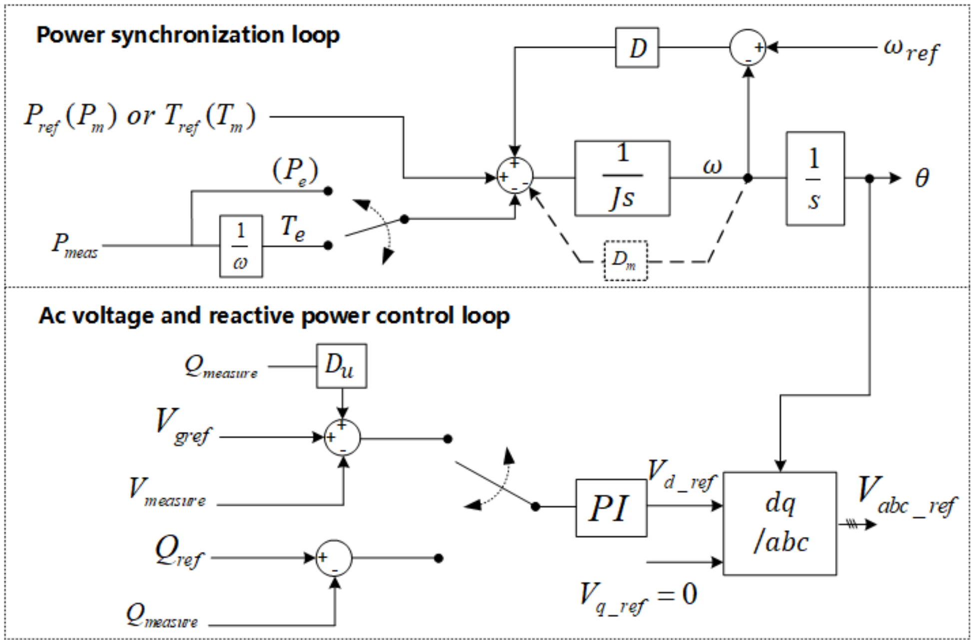

Figure 3-2 VSM control diagram

The PCC ac voltage magnitude $|e_{abc}|$ is generated by the ac voltage controller or reactive power controller that is similar to the function of an AVR (automatic voltage regulator) in a synchronous machine. In ac voltage control mode, a reactive power droop control is introduced to regulate the reactive power through the droop coefficient D_u by equation (3.2)

$$D_u = \frac{\Delta V}{Q} \tag{3.2}$$

The reactive power can also be directly regulated with a feedback control like the ac voltage controller. The ac voltage or the reactive power control loop generates the ac voltage reference magnitude $|e_{abc}|$. Together with and synchronization angle θ which is generated from the power synchronization loop, the ac voltage reference e is sent out to the lower-level modulation control to generate the firing signals for the converter.

It should be noted that the VSM has a tendency to have poor performance and even become unstable when connected a strong ac system. This can be attributed as due to the fact that the strong ac system has a much smaller ac side impedance, which can precipitate a large power and overcurrent transient even for a small phase angle difference between VSM and the ac system. However, as will be shown later in this thesis, careful tuning of the controller gains can achieve good performance when connected to both weak and strong systems.

3.1.1 Equivalence of VSM and Droop-based GFM control

Droop-based GFM control is another popular GFM technique widely used for VSC [13][14][15][16][78]. Figure 3-3 shows the power synchronization control loop of Droop-based GFM control. Here ω_{ref} is the setpoint for the grid angular frequency. The active power and angular frequency are made to follow a droop characteristic shown in equation (3.3).

$$m_p = \frac{\omega - \omega_{ref}}{P_{ref} - P_{mf}} \tag{3.3}$$

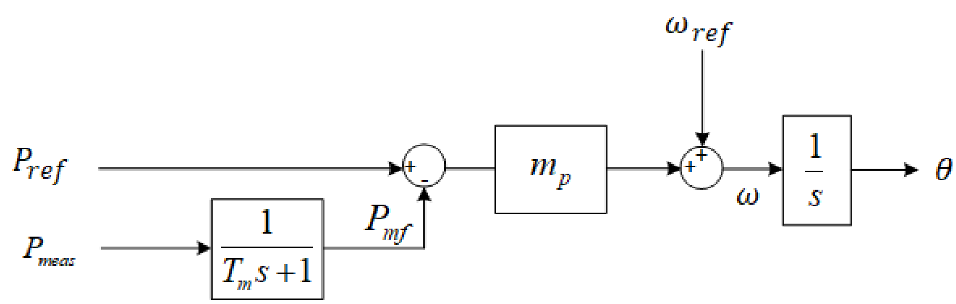

Figure 3-3 Droop-based GFM control power synchronization loop

As seen in the figure, the measured power P_{meas} is low pass filtered before being used as a feedback signal P_{mf} to the controller. The low pass filter is essential to filter out measurement noise. References [25][26] also show that this filter has a positive role in maintaining stability. From Figure 3-3, P_{meas} can be expressed by (3.4):

$$P_{meas} = (1 + T_m s)(P_{ref} + \frac{\omega_{ref} - \omega}{m_p}) \tag{3.4}$$

Expanding the equation (3.4) can result in:

$$P_{meas} = P_{ref} + T_m P_{ref} s + \frac{T_m \omega_{ref} s}{m_p} - \frac{T_m \omega s}{m_p} + \frac{\omega_{ref} - \omega}{m_p} \tag{3.5}$$

With P_{ref} and ω_{ref} constant, the derivative terms in (3.5) become zero to give (3.6):

$$\frac{T_m}{m_p}\omega s = P_{ref} - P_{mf} - \frac{1}{m_p}(\omega - \omega_{ref}) \tag{3.6}$$

According to the VSM control diagram shown in Figure 3-2, the mechanism of the power synchronization loop of VSM can be represented by the equation (3.7)

$$J\omega s = P_{ref} - P_{meas} - D(\omega - \omega_{ref}) \tag{3.7}$$

If the active power order P_{ref} and grid frequency ω_{ref} setpoint is the same for VSM and Droop-based GFM control, an equivalence is established between the inertia J and damping D with Droop-based GFM control if:

$$J = \frac{T_m}{m_p}, D = \frac{1}{m_p} \tag{3.8}$$

Thus, the damping D of the VSM is inversely related to the droop parameter m_p. The time constant T_m of the low pass filter on active power measurement for Droop-based GFM control represents the inertia J of the VSM. Due to the equivalence, for convenience, the GFM in the future discussion of this thesis represents a VSM if not specifically mentioned, but it is readily seen that it corresponds to a Droop-based GFM control with gain m_p and time constant T_m, as J and D related by (3.8).

3.2 EMT simulation Comparison of VSM with a synchronous machine or GFL converter

A test system shown in Figure 3-4 is developed on the EMT simulator PSCAD/EMTDC to demonstrate the behaviour of VSM. In the test system, a symmetrical monopole MMC-HVdc system is modelled with the specifications shown in Table 3-1. The rectifier side of the MMC-HVdc link is assumed to be connected to a strong ac grid and operated in GFL dc voltage control mode. Hence, in the following discussion, the dc link voltage is assumed to be constant. The inverter side of the MMC-HVdc link is connected to a weak ac grid and operated in VSM control mode to regulate the active power. The ac grid is represented by a Thevenin equivalent voltage source behind resistor R and inductor X. Selecting appropriate values for R and X allows any desired ac system strength, i.e., short circuit ratio (SCR). For this test case, the inverter side impedance is $264.5\angle 80^{o}\,\Omega$ and the SCR of the ac grid at the inverter side is

$$SCR_{inv} = \frac{S_{SCMVA}}{P_{RMW}} = \frac{V_{RkV}^2 / Z_{grid}}{P_{RMW}} = \frac{230^2 / 264.5}{200} = 1 \tag{3.9}$$

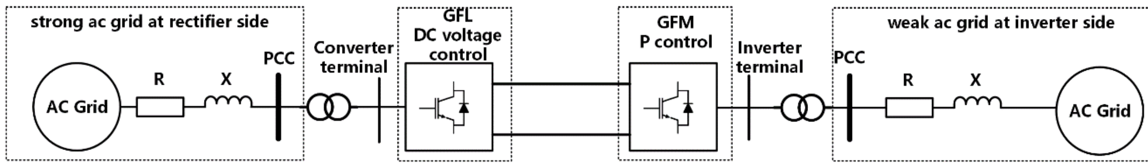

Figure 3-4 test system setup

MMC-HVDC pole configuration	symmetrical monopole
DC link voltage	+/- 120 kV
Transmission length	250 km
Rated power	200 MVA
Submodule number	200
Converter transformer winding voltage	230kV/116.7 kV
Converter transformer reactance	0.18 pu
MMC Converter equivalent arm reactance	0.055 pu
Transformer windings configuration	Yg (HV)/Delta (LV)
Rated ac system voltage	230 kV, 60Hz

Table 3-1 test system specifications

3.2.1 Comparison of VSM and synchronous machine

Based on the test system shown in Figure 3-4, an actual synchronous machine is connected to the same weak ac system (SCR=1) to be compared with VSM. The synchronous machine is rated at 200 MVA, which is the same as the nominal rating of the VSM.

3.2.1.1 Power order step change

Figure 3-5 shows the EMT simulation results of the synchronous machine active power response at the PCC to a mechanical torque order step change from 1 pu to 0.9 pu at 15s with different inertia J ($J = 1s$ and $5s$). It indicates that an increase in the synchronous machine inertia J decreases the transient oscillation frequency and increases the settling time to the new steady state.

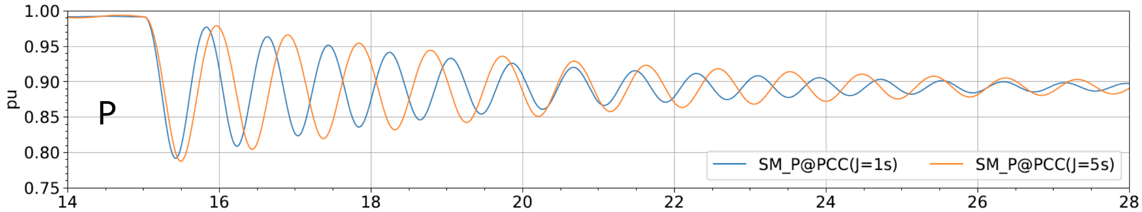

Figure 3-5 The synchronous machine active power response to the mechanical torque order step change with different inertia J.

To check the dynamic response of VSM, first, the active power response of the synchronous machine to a step change in the mechanical torque order is compared with that of VSM. Figure 3-6(a) shows the EMT simulation results of the active power step response for the synchronous machine and VSM. They can have similar dynamic behaviour if VSM ($J = 4s, D = 4\,pu$) has the same inertia and close damping to the synchronous machine ($J = 4s, D \approx 1pu$).

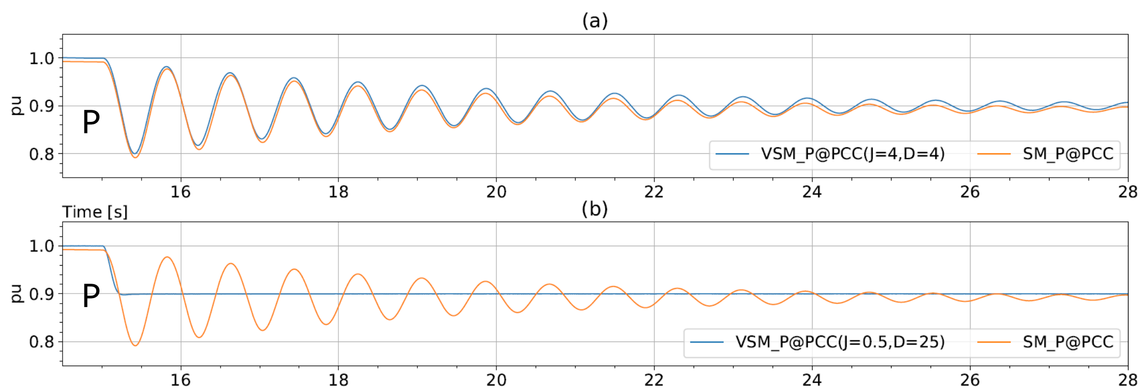

Figure 3-6 Comparison of the synchronous machine and VSM active power response to the mechanical torque or active power order step change. (a)VSM J=4, D=4 (b)VSM J=0.5, D=25

As mentioned previously in Section 3.1, the inertia and damping of VSM can vary from the typical values (i.e., $J = 1 \sim 20s$ [48]) in the synchronous machine. This allows VSM to select a wider range of inertia constant J and damping coefficient D than the actual synchronous machine does and achieve better control dynamic behaviour compared with the synchronous machine shown in Figure 3-6(b) when VSM uses $J = 0.5\ s, D = 25\ pu.$

Next, a further comparison of VSM dynamic behaviour with different key control parameters is shown in the EMT simulation results in Figure 3-7. It shows the VSM response to the active power order step changes from 1.0 pu to 0.5 pu at 5 s, then to 0.75 pu at 8 s, with different inertia J and damping D. The results show VSM has a faster dynamic response for smaller J, as seen by comparison the blue ($J = 0.5\ s$) and green ($J = 5\ s$) curves. Likewise, larger D makes the step response more damped, as seen by the comparison of the blue ($D = 25\ pu$) and orange ($D = 100\ pu$) curves. It also indicates that when the ratio D/J remains the same ($D/J = 5$), larger J and D combination have slower dynamic response but more damped, while smaller J and D combination have a faster dynamic response but more undamped, as seen by comparison the red ($J = 1\ s, D = 5\ pu$) and green ($J = 5\ s, D = 25\ pu$) curves.

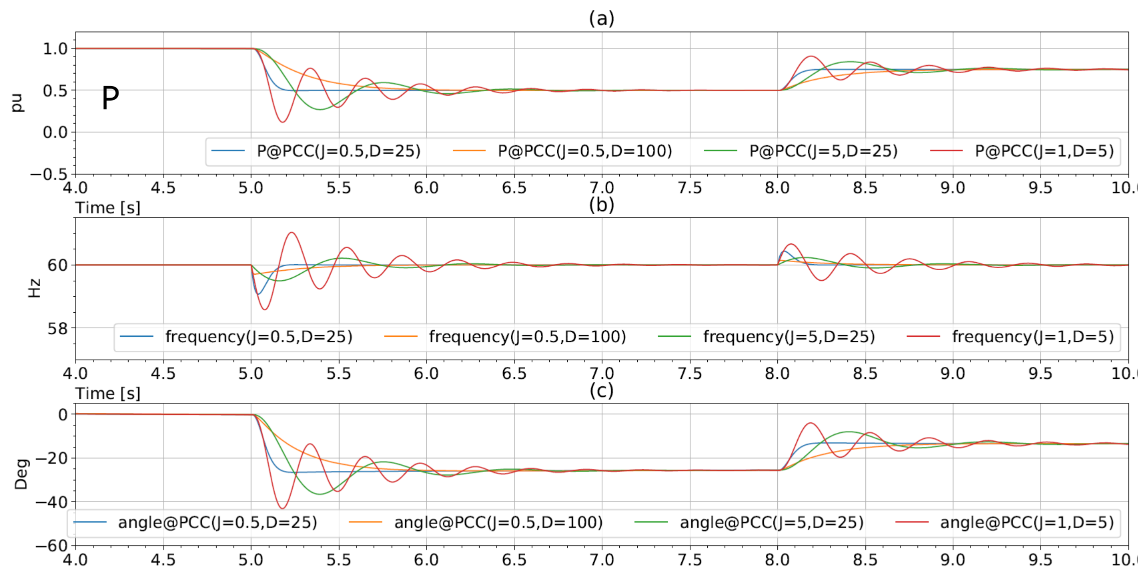

Figure 3-7 VSM response to the active power order step changes with different inertia J and damping D. (a) active Power response at inverter side PCC. (b)inverter side frequency response. (c) ac voltage angle response at inverter side PCC.

3.2.1.2 Ac system frequency change

Now let us see what happens to the real synchronous machine and VSM if the ac system frequency changes. Consider a real synchronous machine without a speed governor. Assume that the input mechanical torque is kept constant and the ac system frequency drops from 60 Hz to 59 Hz with a ROCOF of 2 Hz/s. Initially, there is a momentary increase in the output power of synchronous machine which is required to slow it down and resynchronize to the new system frequency of 59 Hz. The machine then achieves a virtual rotor speed of $2\pi \cdot 59\ rad/s$, and consequently, the output power P_e which is a product of torque and speed also decreases. Eventually, in the new steady state, the electrical torque T_e again will equal to the mechanical torque T_m, but both the mechanical power P_m and the electrical power P_e will decrease, with the machine now running at the new synchronous speed corresponding to 59 Hz. This is because for a synchronous machine, the rotating magnetic field rotates at synchronous speed which is linked to the system frequency and thus the system frequency change is intrinsically tracked. The relation between output electrical power and electrical torque considering a small deviation (denoted by prefix Δ) from the initial values (denoted by subscript 0) can be expressed by

$$P_{e0} + \Delta P_e = (\omega_0 + \Delta\omega)(T_{e0} + \Delta T_e) \tag{3.10}$$

The relationship between the perturbed values with higher-order terms neglected is given by

$$\Delta P_e = \omega_0 \Delta T_e + T_{e0} \Delta\omega \tag{3.11}$$

In the new steady state, $\Delta T = 0$. Therefore, in pu form,

$$\Delta P_{epu} = \Delta\omega_{pu} \tag{3.12}$$

In this case, as the ac system frequency drops from 60 to 59Hz (i.e., 1.67 % drop) and the active power output change is given:

$$\Delta P_{epu} = \Delta\omega_{pu} = \frac{60-59}{60} = 0.0167\,pu \tag{3.13}$$

Thus, the active power output from the synchronous machine changes marginally by about 1.67% equal to the 1.67% frequency drop in system frequency.

In contrast, the simplified VSM control shown in Figure 3-2, reasonably simulates the synchronous machine's swing equation dynamics, but does not automatically track the system frequency change. This is because frequency reference ω_{ref} is fixed at 1pu, and when there is a change in the network frequency, there is a damping coefficient related change in the output power in the steady state. This is because in the steady state,

$$\Delta P_{pu} = D \cdot (\omega_{ref} - \omega_{pu}) = D \cdot (1 - \omega_{pu}) \tag{3.14}$$

Thus, if the system frequency drops to 59 Hz and the VSM damping coefficient $D = 10\ pu$, then this power deviation is $\Delta P_{pu} = 0.167\ pu$ or 16.7% which is much larger than the change with a real synchronous machine.

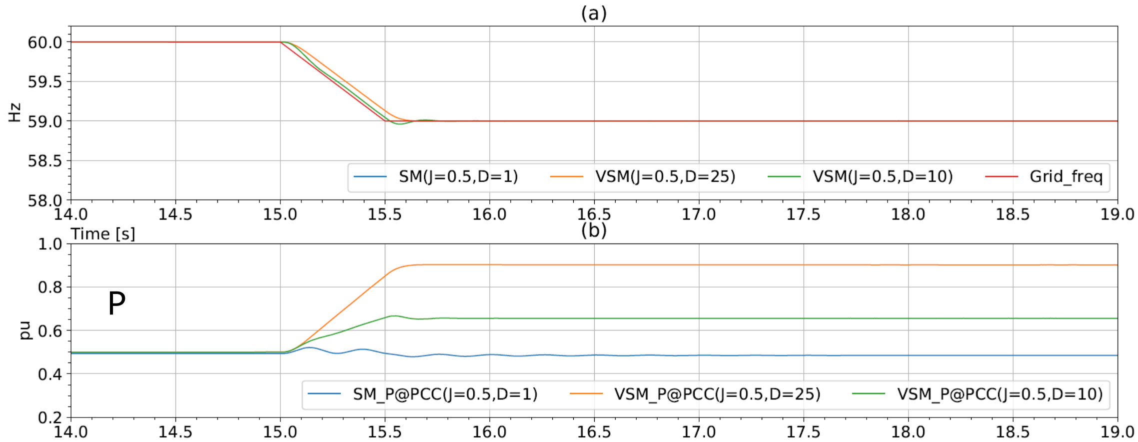

Figure 3-8 VSM and synchronous machine response to system frequency ramp of -2 Hz/s (a) response of synchronous speed (b) response of active Power output

Figure 3-8 shows the EMT simulation of VSM and synchronous machine response to the grid frequency change. The SM has an inertia constant of $J = 0.5\,s$, and damping coefficient D is 1pu. The VSM options of inertia and damping are (0.5, 25) and (0.5, 10). The ac system frequency is changed from 60 Hz to 59 Hz at 15 s with a rate of change of frequency (RoCoF) = -2 Hz/s. Figure 3-8 (a) shows the frequency of the VSM and the synchronous machine with the changing system frequency. Figure 3-8 (b) shows the active power output of the synchronous machine changes very marginally (1.67%). On the other hand, the power of the VSM changes more significantly from 0.5 pu to 0.667 pu (16.7%) when $D = 10\,pu$. For a larger damping coefficient $D = 25\,pu$, it is even larger change from 0.5 pu to 0.92 pu (42%).

This active power output deviation can be detrimental to VSM. When the converter operates at rated power, the grid frequency drop can cause an increase in active power output and may overload the converter. However, this problem can be solved by tracking the grid frequency instead of giving a fixed reference ω_{ref}, such as using a PLL, or a low pass filtered synchronous speed feedback. Figure 3-9 shows the VSM power synchronization loop with grid frequency tracking. The grid frequency ω_{ref} can be made equal ω_{fil}, which is obtained by low pass filtering the signal ω generated by the swing equation as in Figure 3-2 or from the tracked system frequency ω_{PLL} generated via a PLL. Note that, for VSM islanded applications or transient disturbance ride through, the VSM frequency reference would be fixed at $\omega_{ref} = 1\,pu$.

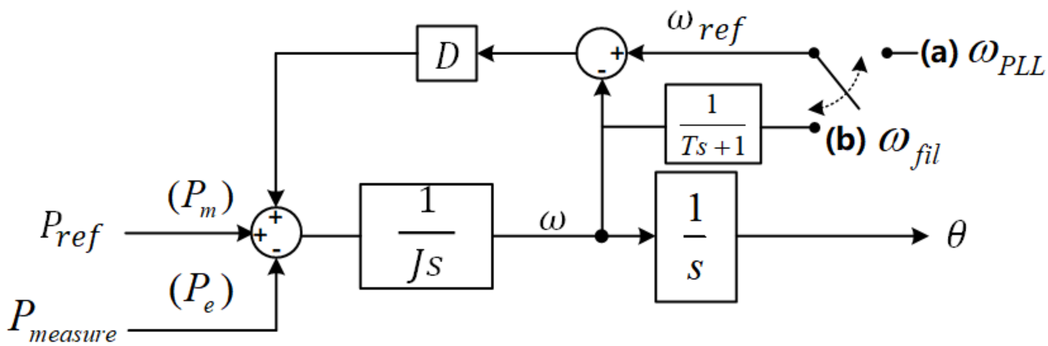

Figure 3-9 Power synchronization loop with grid frequency reference from (a)PLL ($k_p = 10, k_i = 20$) (b)Low pass filtered feedback ($T = 0.1s$)

Figure 3-10 shows the EMT simulation of VSM with grid frequency tracking and the synchronous machine response to the grid frequency changing with a RoCoF of -2 Hz/s. When the system frequency starts to drop from 60 Hz to 59 Hz at 15 s, there is no damping coefficient related active power output deviation in the new steady state for VSM if the grid frequency is tracked.

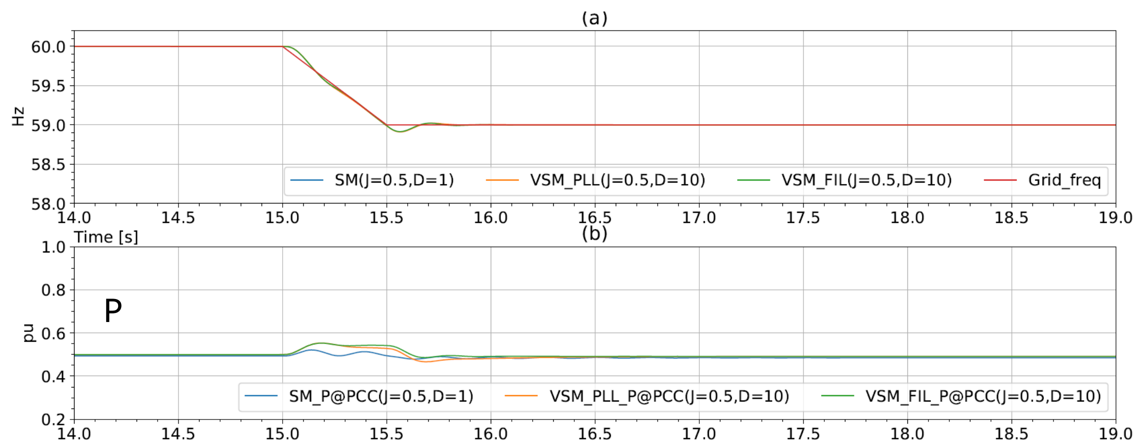

Figure 3-10 VSM with grid frequency tracking and synchronous machine response to system frequency ramp of -2 Hz/s (a)response of synchronous speed. (b)response of active Power output.

It should be mentioned that if the electrical torque T_e ($= P_{measure}/\omega$) is used as the feedback signal there will be a slight difference from the response of the model which used electric power, as shown in Figure 3-11. The active power output will then be slightly different after the system frequency changes to a new value. For convenience in this thesis, the VSM is implemented with active power measurement P_{meas} as the control feedback.

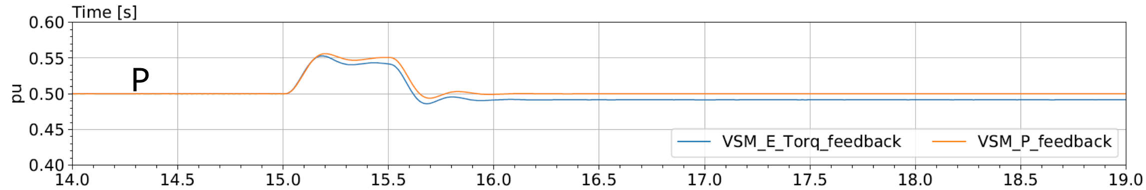

Figure 3-11 VSM active power response to the system frequency change with different control feedback (blue line: electrical torque, orange line: active power)

3.2.2 Comparison of VSM and GFL converter operation

3.2.2.1 Performance with a weak ac system

Based on the test scenario shown in Figure 3-4, an EMT simulation is conducted to compare GFL and VSM converter operation when connected to a weak system (SCR=1). Figure 3-12 shows the EMT simulation results of the HVdc inverter response to the active power order step changes in both VSM and GFL control modes. The power order changes from 1pu to 0.5 pu at 5 s then changes from 0.5 pu to 0.75 pu at 8 s. Figure 3-12 shows (a) the inverter side measured power at PCC, (b) the measured frequency and (c) the voltage angle at the inverter PCC bus for the GFL and VSM mode operation. For VSM, the frequency is directly obtained from the swing equation in the power synchronization control loop, whereas for the GFL it is measured using a phase-locked loop (PLL). The PLL gains are optimized for the weak ac system as the SCR is 1 ($k_p = 0.5$, $k_i = 1$). For such a weak ac system, if the inverter is operated in GFL control mode to control the active power, instability is observed when the power order changes; however, if the inverter is operated in VSM control mode, it can maintain stable operation, and its performance is greatly improved.

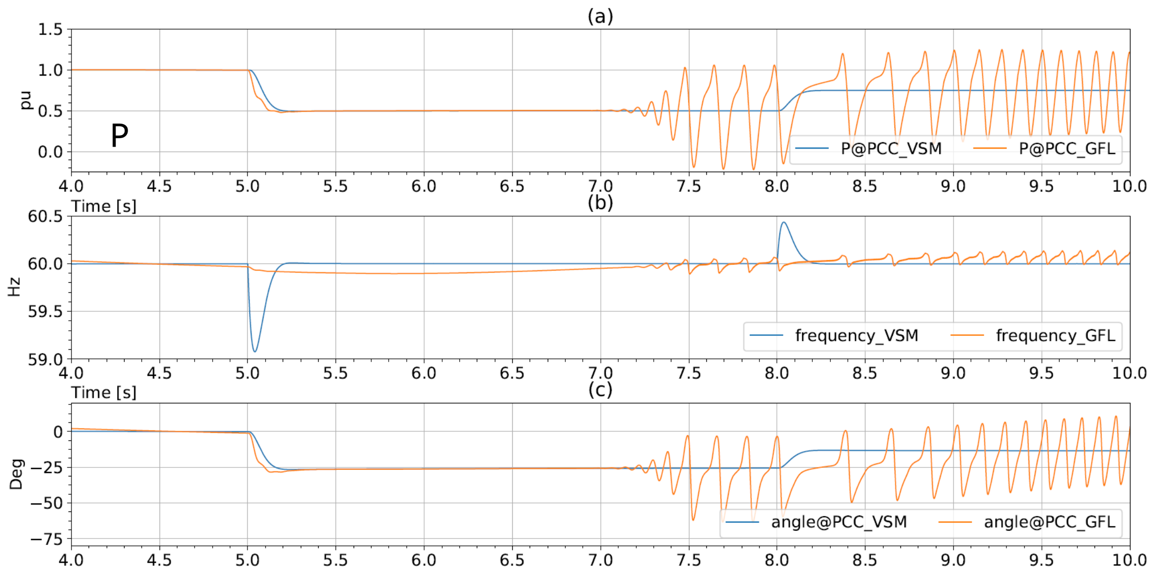

Figure 3-12 VSM (J=0.5s, D=20 pu) and GFL VSC response to the active power order step changes in a weak grid scenario (SCR=1). (a) measured Power at inverter side PCC. (b)inverter side ac system frequency. (c)measured ac voltage angle at inverter side PCC.

3.2.2.2 Performance with a jump in the phase of the ac voltage

Next, the SCR of the inverter side ac system is increased to 2.5 but other system specifications remain the same. This permits the GFL converter to maintain stable operation with a good dynamic response which was not possible with the weaker ac system.

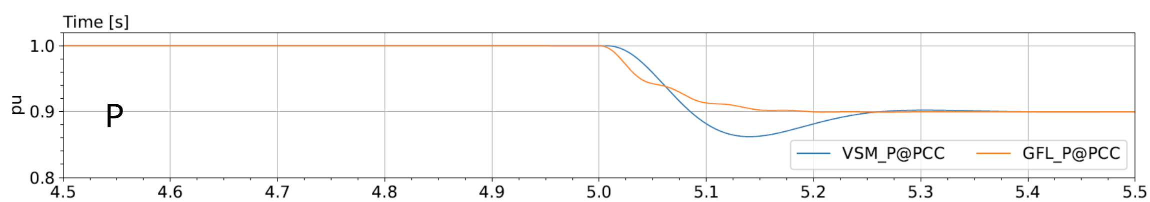

Figure 3-13 VSM and GFL VSC active power step change response

An active power order step change from 1 pu to 0.9 pu in the simulation is applied at $t = 5\ s$ for VSM and GFL scenarios. The VSM ($J = 0.5\ s, D = 20\ pu$) demonstrates a slightly underdamped response with a settling time of 0.22 s to 90% of the order change compared with the GFL converter which has a well-damped response with a settling time of 0.12 s as in Figure 3-13. The VSM's underdamped response could be accounted for by oscillations generated by its virtual inertia.

The VSM inertia behaviour can be also observed in a case where a sudden change to the phase angle of the ac voltage. In this test, a 30 degrees phase shift is applied to the Thevenin equivalent voltage source to emulate the ac voltage phase angle change close to the PCC bus, which could be precipitated by some grid events e.g., power flow change. The VSM responds to this phase angle change as dictated by the swing equation and the associated inertia inherent in the model, and hence gives a sluggish response. In contrast, the GFL synchronizes through a PLL (i.e., no inertia in the model) and shows a much faster response than the VSM as seen in Figure 3-14(a). The transient active power change of VSM is larger than that of the GFL converter since the active power output is directly linked to the phase angle according to the swing equation, which can be observed in Figure 3-14(b).

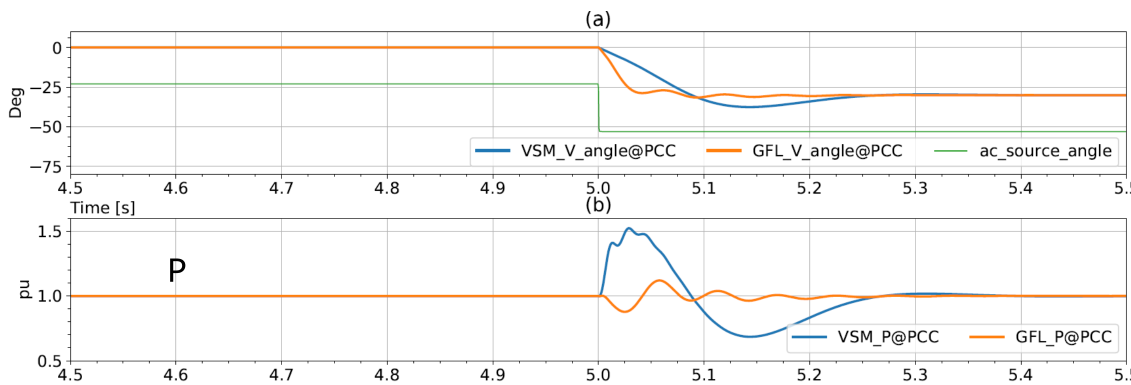

Figure 3-14 GFM and GFL VSC (a)controlled PCC voltage phase and (b)active power response to the connected ac voltage source phase angle jump

Another case that shows the inertia response from VSM is the system frequency change test. In this test, the ac system frequency drops from 60 Hz to 59 Hz at 5 s with ROCOF of -2 Hz/s shown in Figure 3-15(a). Figure 3-15(b) shows the active power output from VSM and GFL converter. The active power output from the GFL converter does not respond to this frequency change. The VSM, however, experiences a transient active power increase, showing that it is trying to add energy to the ac network to counteract the frequency ramp down.

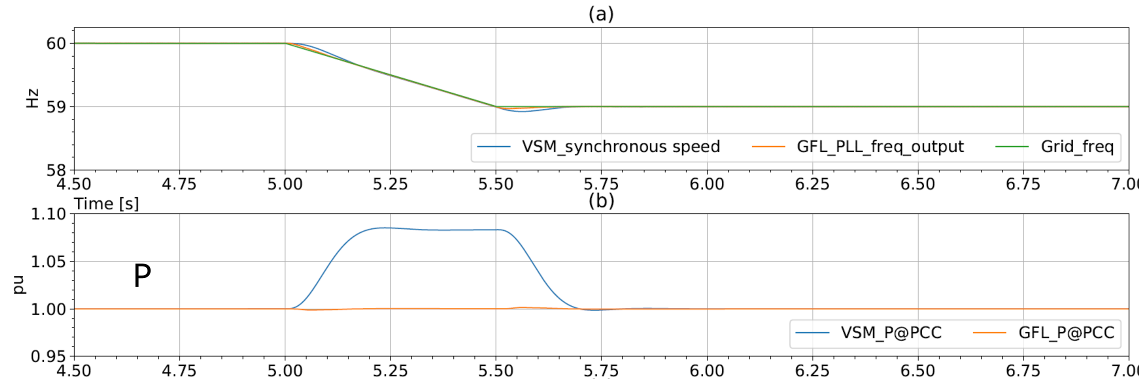

Figure 3-15 VSM and GFL response to ac voltage frequency ramp of -2 Hz/s (a)response of Frequency output. (b)response of active Power output

3.3 Overcurrent limiting on VSM

As VSM in Figure 3-2 was made to emulate a real synchronous machine which has no inherent current limiting controller, it too is not equipped with such a controller. Figure 3-16 shows the instantaneous current obtained by an EMT simulation of a solid three-phase to ground fault on VSM at its PCC bus. The fault starts at 5 s and lasts for 5 cycles (0.083 s). The short circuit current is 6.5 pu which could damage the converter's IGBT values whose overcurrent capability is usually limited to about 2 pu [27]. Although the converter could be designed to have a larger short circuit current capacity, it is unadvisable due to the increased cost. Thus, an overcurrent limiting control is required for VSM. Two current limiting control options will be discussed in the following sections.

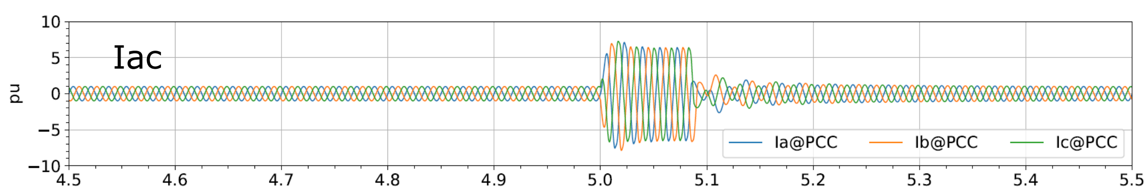

Figure 3-16 short circuit current from VSM without current limiting

3.3.1 Switchable current limiting control

In the switchable current limiting control, during overcurrent, VSM's ac voltage control loop is switched out and replaced by a fast current control loop. When the current magnitude returns to normal, this current controller is switched out and the VSM ac voltage control resumes.

The control diagram of this current limiting method is shown in Figure 3-18. The VSM control for normal operation is shown on the left side of the figure, while the current limiting control is shown on the right side of the figure. The converter current magnitude is readily obtained from the d and q current components as:

$$i_{dq,mag} = \sqrt{i_d^2 + i_q^2} \tag{3.15}$$

In the equation (3.15), i_d and i_q are current in d-q frame on the converter side, which can be acquired from the measured three-phase current and VSM control synchronization angle through Park's transformation [85]. The control mode switch compares this current magnitude with the predetermined threshold current I_{max}. If $I_{max} \leq i_{dq,mag}$, then i_d and i_q will be held at their values at that moment and the current limiter will be activated. The current limiter generates the d-q current reference i_{dref} and i_{qref} for the current control loop, which can be expressed by:

$$\begin{aligned} \varphi &= \tan^{-1}\frac{i_d}{i_q} \\ i_{d,ref} &= \min(I_{\max}, \sqrt{i_d^2 + i_q^2}) \cdot \sin\varphi \\ i_{q,ref} &= \min(I_{\max}, \sqrt{i_d^2 + i_q^2}) \cdot \cos\varphi \end{aligned} \tag{3.16}$$

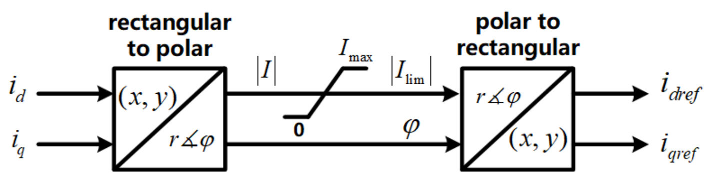

Figure 3-17 Current limiter diagram

This ensures that the reference current's phase angle is maintained at φ, but its magnitude is limited to I_{max} as shown in Figure 3-17. With this current reference, the current control loop shown in the black box in Figure 3-18 regulates the VSM output current by generating the required voltages e_{abc} during the fault transient. Once the fault is cleared and the control mode switch detects $I_{max} > i_{dq,mag}$, the control will switch back to normal operation mode and the voltage magnitude reference will again come from the ac voltage and reactive power control loop.

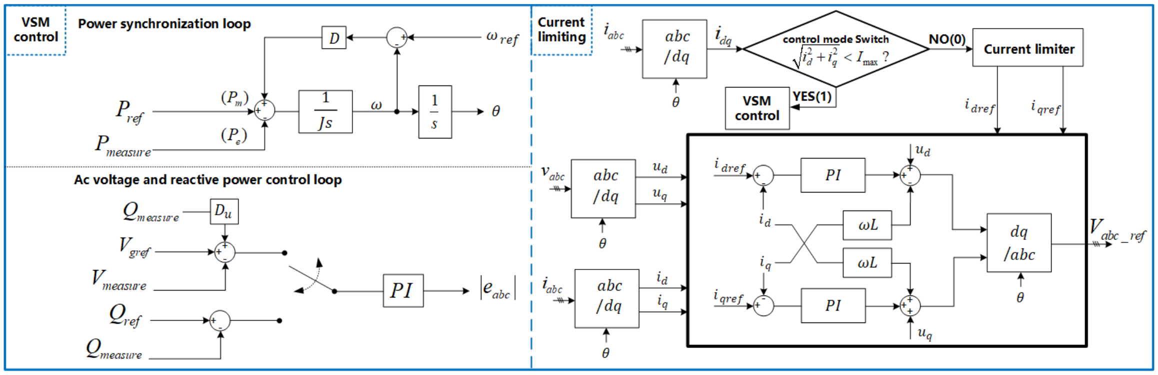

Figure 3-18 VSM control with switchable current limiting control

To test the performance of the switchable current limiting control, a 12-cycle (200 ms) long solid three-phase to ground fault is applied at the inverter side PCC bus of the test system shown in Figure 3-4 at t = 5 s. The VSM's inertia constant and damping coefficient are $J = 0.5\ s$ and $D = 20\ pu$. In general, the solid three-phase to ground fault should be cleared in about 5 cycles, but here the fault period is extended to 12 cycles to test the current limiting performance in some extreme cases such as protection failure. The overcurrent limit I_{max} is set at 1.3 pu which is a sufficiently safe value for the VSC's semiconductor components.

First, the weak system case is simulated, with the VSM connected to an ac system of SCR=1.0. Figure 3-19 shows the EMT simulation results of (a) instantaneous current from VSM, (b) RMS current from VSM, (c) RMS voltage at the PCC bus, (d) active power and reactive power output from VSM and (e) switch control mode selection from VSM with switchable current limiting. During the fault, the current control loop is selected and the short circuit current from VSM is limited at 1.3 pu. After the fault, the control switches back to ac voltage control and the system recovers in normal operation (80% power) after a 140 ms transient.

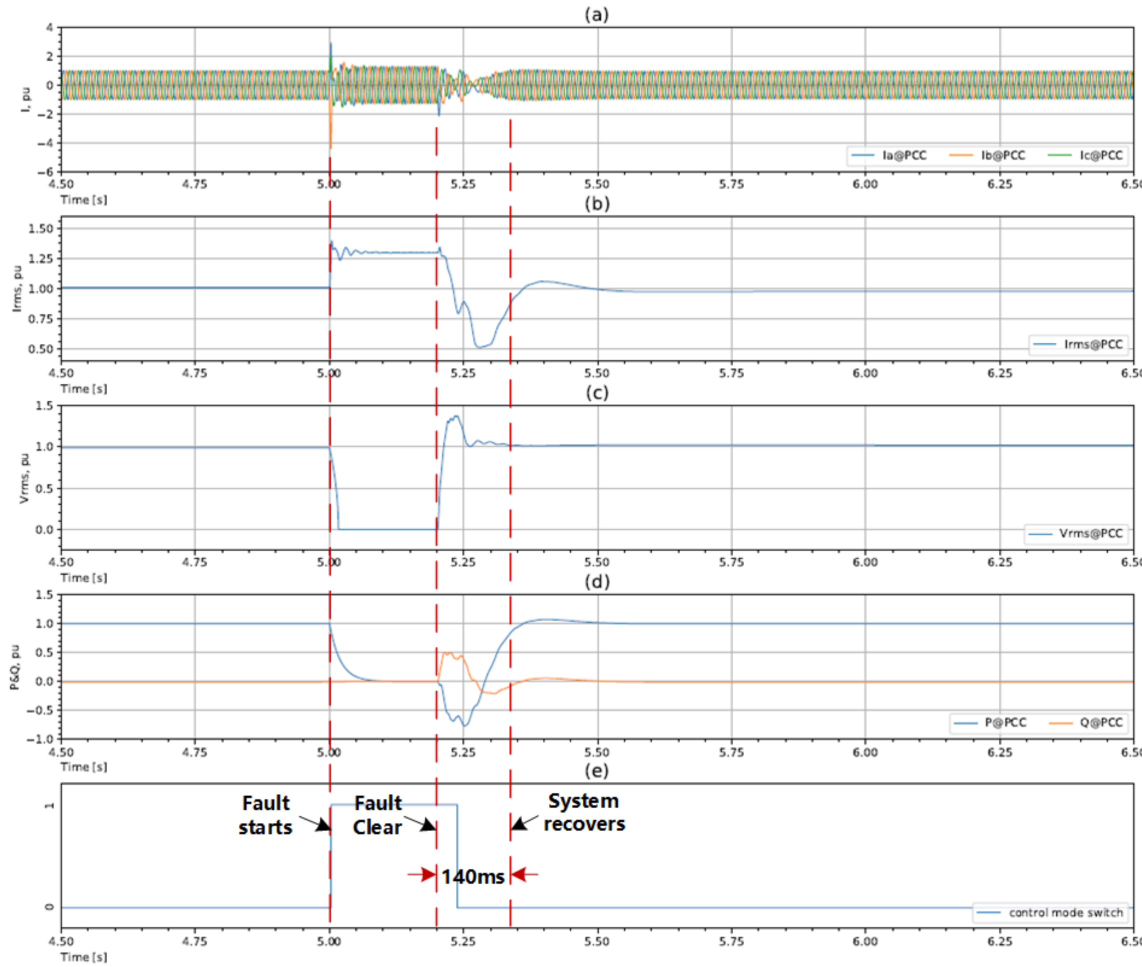

Figure 3-19 VSM with switchable current limiting control for a solid three-phase to ground fault at PCC bus.(SCR=1) (a) Instantaneous current from VSM (b)RMS current (c)RMS ac voltage at PCC (d)active and reactive power output (e) control mode switch (1=current limiting, 0=normal)

As can be seen in Figure 3-19(c) and Figure 3-19(d), although the current limiting control loop works well during the fault, there is an overvoltage (up to 1.4 pu) and reverse power transient (up to -0.8 pu) during post fault recovery period. This is due to that the voltage angle generated by the VSM power synchronization loop has a large variation during the fault. This can be observed in Figure 3-26(a) where it changes from 0 to -155 degrees. Since the voltage angle change goes beyond -90 degrees, the active power direction is changed transiently.

Now we investigate what happens when the connected ac system becomes stronger. The performance of VSM switchable current limiting with connected ac systems ranging from weak (SCR =1) to very strong (SCR=10) are shown in Figure 3-21. In Figure 3-21, (a) is the ac voltage at PCC, (b) is the active power output from the converter and (c) is the current control loop (CCL) switch signal (CCL=0 meaning current control is not active, CCL=1 means current control is activated.). Note for a strong ac system, e.g., SCR = 5 or 10, the system fails to ride through the ac fault. This can be attributed as due to the fact that the strong ac system has a much smaller ac side impedance, which can precipitate a large power and overcurrent transient even for a small phase angle difference between VSM and the ac system's Thevenin equivalent voltage source. This makes the switchable control loop accidentally switch in and out during the post fault period and causes system to become unstable. The solution to this problem will be discussed in Section 3.4.

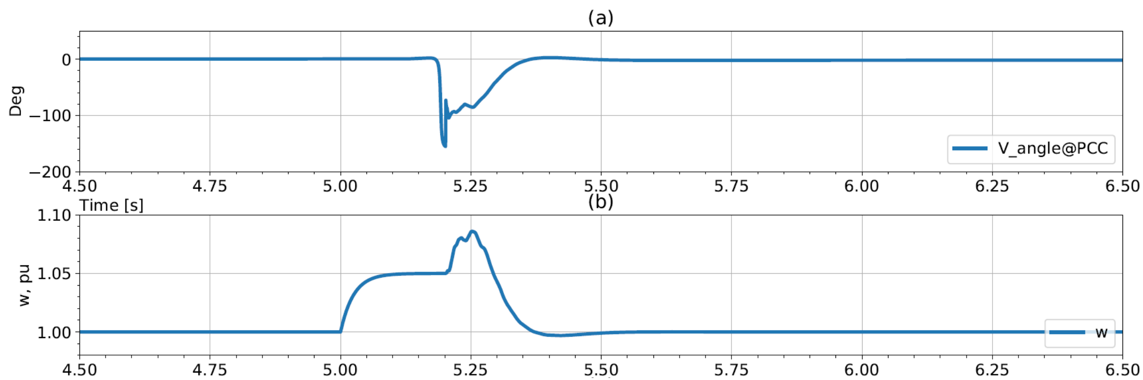

Figure 3-20 VSM with switchable current limiting control (SCR=1) (a)ac voltage angle at PCC and (b)synchronous speed measured from VSM power synchronization loop

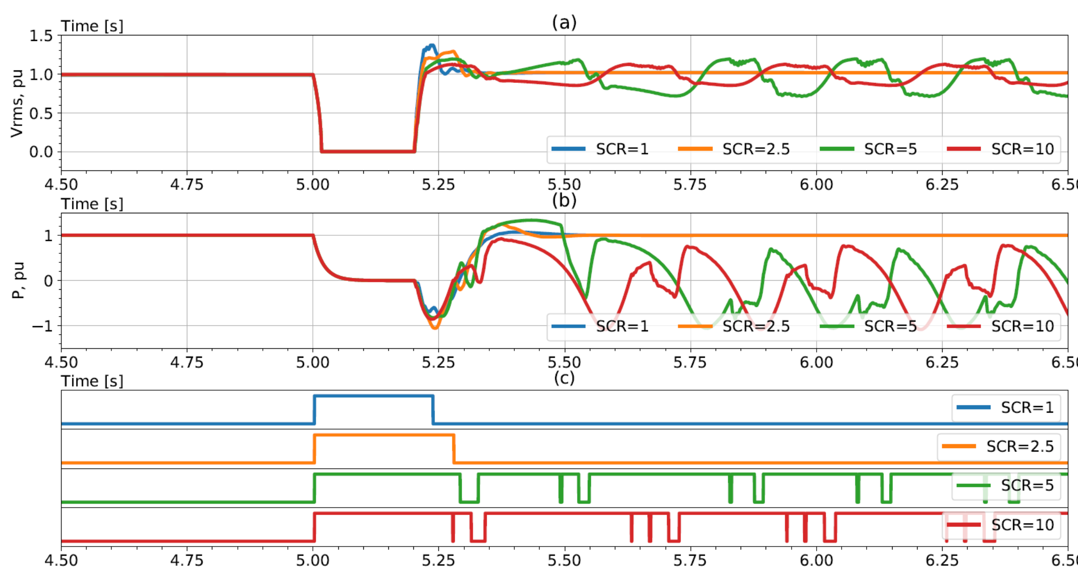

Figure 3-21 VSM with switchable current limiting control under different system strength (a) ac voltage at PCC (b)active and reactive power output (c) control mode switch (1=current limiting, 0=normal)

3.3.2 In-line cascaded current liming control

The switchable current limiting technique discussed in the previous section switches the main voltage control function with a current controlling loop on detection of overcurrent. Even if the switching functions well, the control mode switch also needs a short period to react when a fault is detected. This may cause the overcurrent still to be present for the first or second cycle after fault inception, as can be observed in Figure 3-19 (a).

An alternative approach which overcomes the above drawback is to embed the current limiting control in-line VSM voltage controller as shown in Figure 3-22. Since the current limiting loop is always in-line for normal as well as faulted operation, the approach does not require very fast fault detection and control mode switching.

Compared with the basic VSM control shown in Figure 3-2, a cascaded current control loop in the d-q frame is added in-line with the ac voltage and reactive control loop to generate the ac voltage magnitude reference. The q-axis voltage reference V_{qref} of the current control loop can be set to 0, while the d-axis voltage reference can be equal to the grid voltage reference (a droop control is added to the voltage reference to regulate the reactive power) in ac voltage control mode or generated from an outer reactive power control loop in reactive power control mode. The voltage control loops generate the current reference to the current limiter. Then, the current limiter (see Figure 3-17) generates the current references i_{dref} and i_{qref} for the inner current control loops. Different limiting approaches are possible, such as circular limiting, where the magnitude $\sqrt{i_d^2 + i_q^2}$ of the ac current is limited, but the phase angle $\tan^{-1}(i_d/i_q)$ retained shown in Figure 3-17. Alternatively, i_d or i_q priority control is often employed. In the thesis, the controller uses i_d priority which is often used in HVdc systems for better recovery from ac faults [86]. Finally, the inner current control loops generate the voltage magnitude reference for modulation.

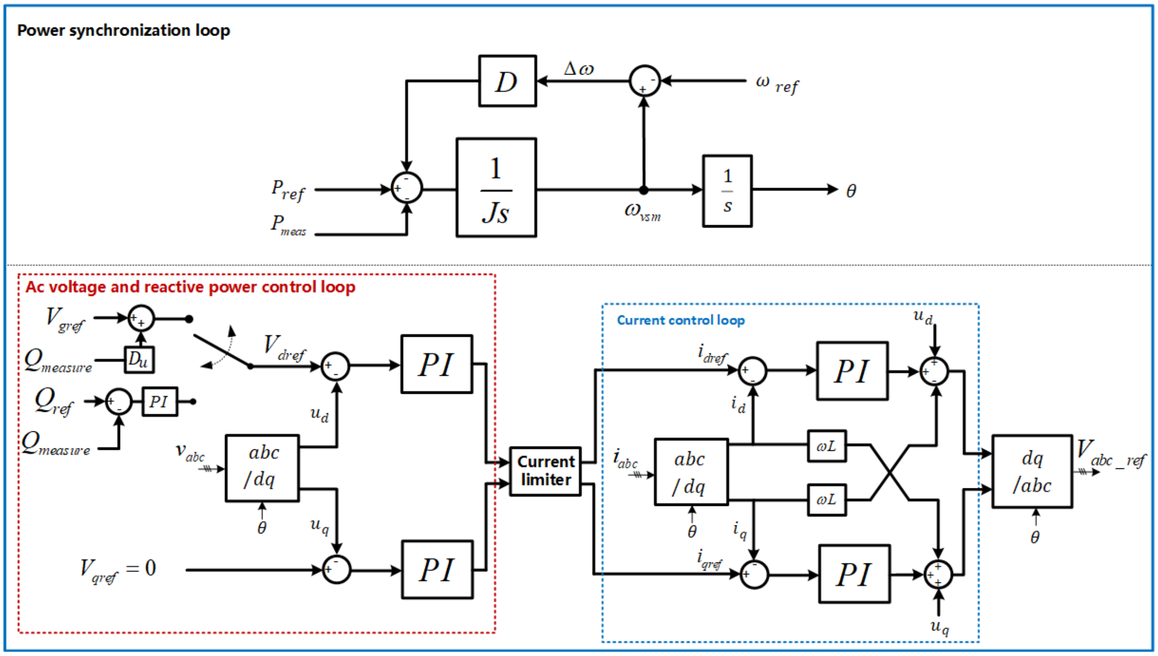

Figure 3-22 VSM control with in-line cascaded current limiting control

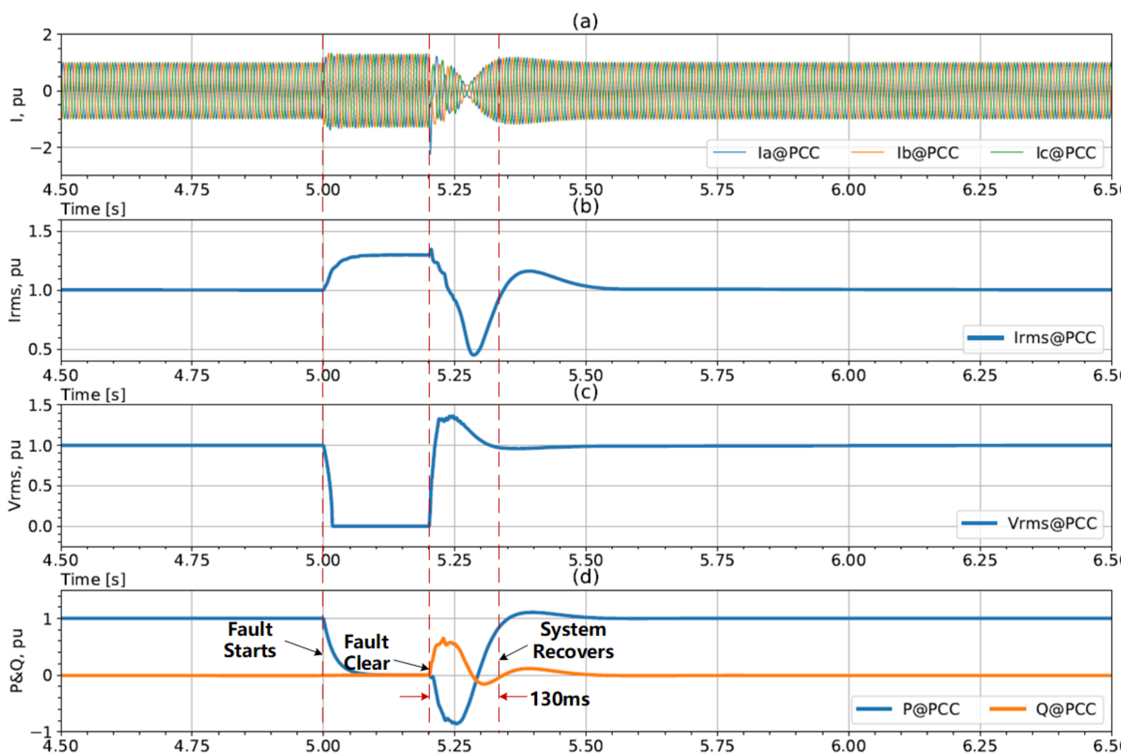

Figure 3-23 VSM with cascaded current limiting control (SCR=1) (a) Instantaneous current from VSM (b)RMS current from VSM (c)RMS ac voltage at PCC (d)active and reactive power output

The same fault test in Section 3.3.1 is applied to VSM with in-line cascaded current limiting. When the connected ac system has an SCR=1, Figure 3-23 shows the EMT simulation results of (a) instantaneous current from VSM, (b) RMS current from VSM, (c) RMS voltage at the PCC bus and (d) active power and reactive power output from VSM with in-line cascaded current limiting. During the fault, the fault current is limited to 1.3 pu. The system recovers in normal operation (80% power) after a 130 ms transient. Although Comparing Figure 3-19 (a) with Figure 3-23 (a) demonstrates the advantage of the in-line current limiting method, solving the overcurrent problem at the beginning of the fault that the switchable current liming brings, the post-disturbance transient reversal of power direction is still noticeable (up to – 0.8 pu) in Figure 3-23 (c).

The performance of VSM in-line cascaded current control with connected ac systems ranging from weak (SCR =1) to very strong (SCR=10) are shown in Figure 3-24. In Figure 3-24, (a) is the RMS ac voltage at PCC and (b) is the active and reactive power output form the converter. Again, for the strong ac network, (e.g., SCR= 10), a loss of synchronism is observed.

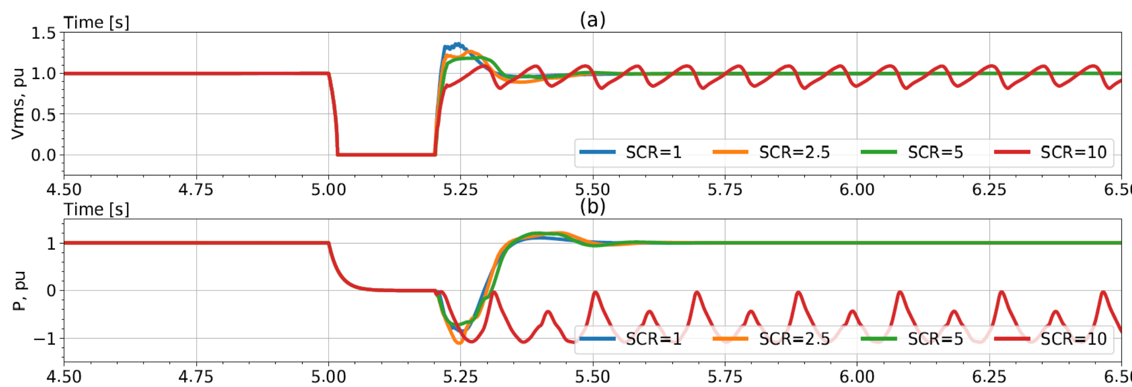

Figure 3-24 VSM with cascaded current limiting control under different system strength (a)RMS ac voltage at PCC (b)active and reactive power output

3.4 Proposed adaptive fault ride through control on VSM

The undesirable transient reverse power and overvoltage observed in Section 3.3.1 and 3.3.2 can be avoided by limiting the voltage angle change to a small range. This can be achieved by limiting the change of the synchronous speed from the VSM power synchronization loop during the fault.

During a solid three-phase to ground fault, the active power output from VSM is close to 0. According to the swing equation, the synchronous speed will increase until

$$P_{ref} - D\Delta\omega = J\frac{d\omega}{dt} = 0 \qquad (3.17)$$

Thus, decreasing the active power order P_{ref} and increasing the damping coefficient D in the VSM can decrease the virtual synchronous speed change $\Delta\omega$ during the fault. If $\Delta\omega$ is small, the voltage angle change can be limited to a small range during the current limiting period. Then the large resynchronization transient of VSM in the post-fault period can be avoided.

It should be noted that the virtual synchronous machine gives more flexibility than a real machine, because the VSM's parameters can be changed at will and even dynamically. Thus, in this thesis, an adaptive fault ride through control mode shown in Figure 3-25 is proposed targeting cancelling the post-fault transient. When an overcurrent is sensed by the VSM, its power order P_{ref} is transiently decreased, and its damping coefficient D is transiently increased. When the overcurrent diminishes, P_{ref} and D are returned to their normal setting values.

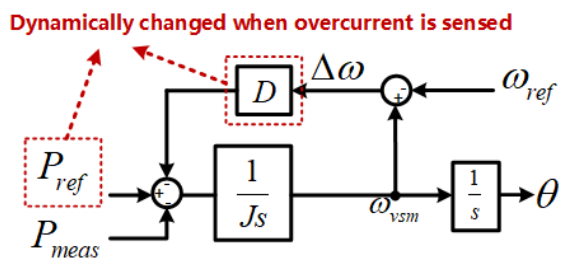

Figure 3-25 Proposed adaptive fault ride through control mode

The proposed adaptive change method is tested on a VSM with in-line cascade current control. The active power order P_{ref} and damping coefficient D transiently changes from 1 pu to 0.5 pu and from 20 pu to 220 pu respectively when the ac current is over 1.3 pu. When the connected ac system SCR=1, Figure 3-26 compares the voltage angle and the synchronous speed for the case with adaptive control (orange) and without adaptive control (blue). Instead of a phase angle change in the range of $[-140, 15]$ degrees, the phase change is much improved and confined to a smaller interval of $[-20, 20]$ degrees.

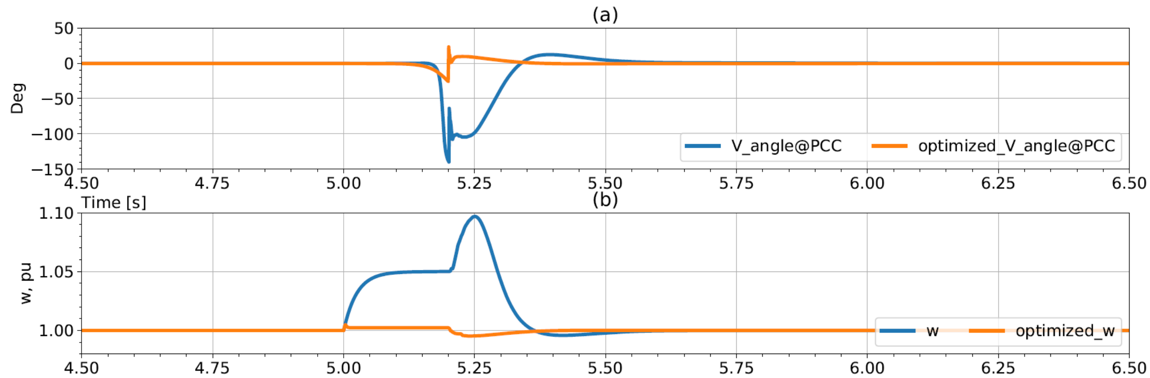

Figure 3-26 Improved (a)ac voltage angle at PCC and (b)synchronous speed measured from VSM power synchronization loop, with proposed adaptive control method(orange).

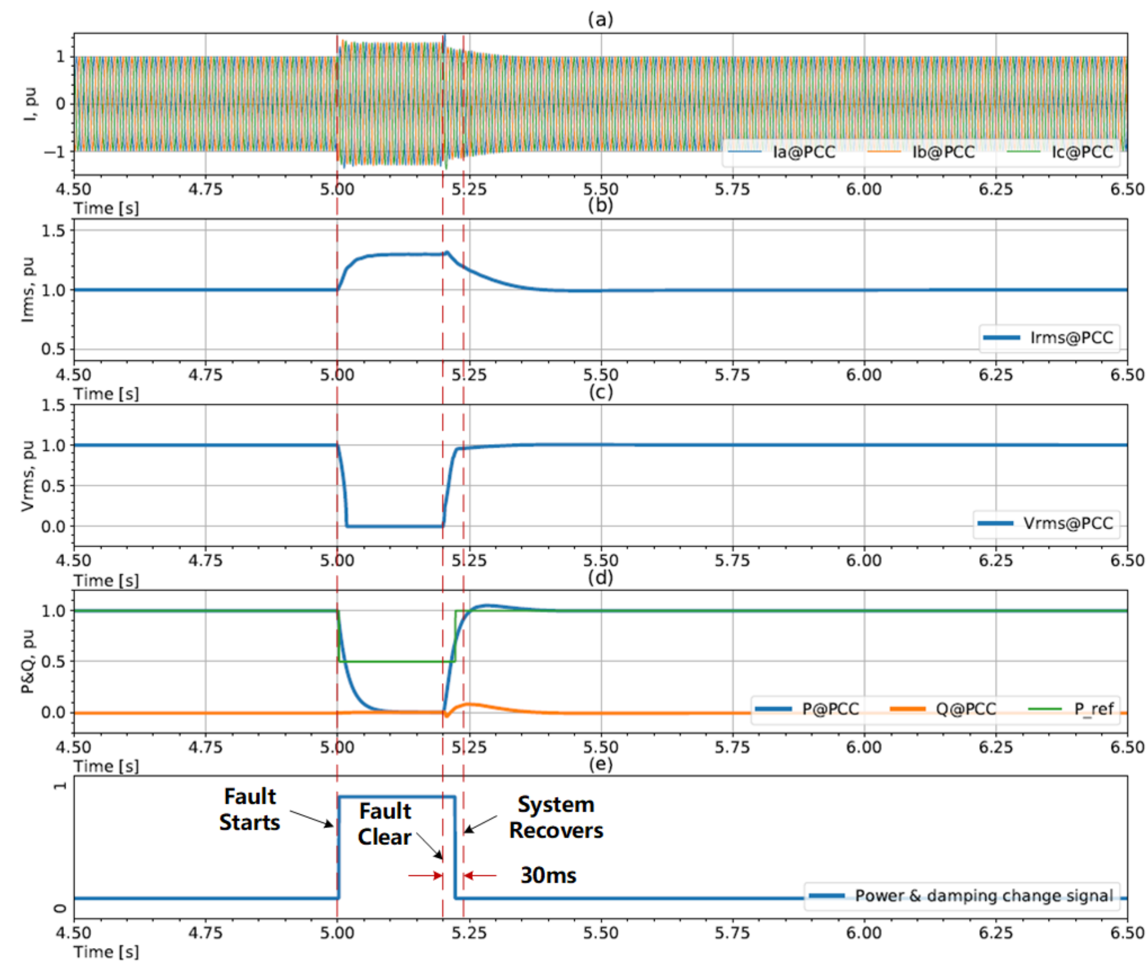

Figure 3-27 Adaptive fault ride through control on VSM with in-line cascaded current limiting control (SCR=1) (a) Instantaneous current from VSM (b)RMS current from VSM (c)RMS ac voltage at PCC (d)active and reactive power output (e)adaptive control switch signal (1=ON, 0=OFF)

With the proposed adaptive fault ride through control, Figure 3-27 shows (a) instantaneous current from VSM, (b) RMS current from VSM, (c) RMS voltage at the PCC bus, (d) active power and reactive power output and (e) the proposed adaptive control switch on signal (1=ON, 0=OFF) for VSM with in-line cascaded current limiting when the connected ac system SCR=1. Compared with the conventional cascaded current limiting results shown in Figure 3-23, there is no transient reverse power and overvoltage problem during post-fault recovery as shown in Figure 3-27 (c) and (d).

Figure 3-28 shows the EMT simulation results of (a) ac voltage at the PCC bus, (b) active power output and (c) adaptive control switched-on signal for SCRs ranging from 1 to 10. It is evident that the ac voltage and active power recovery are much smoother with the adaptive fault ride through control.

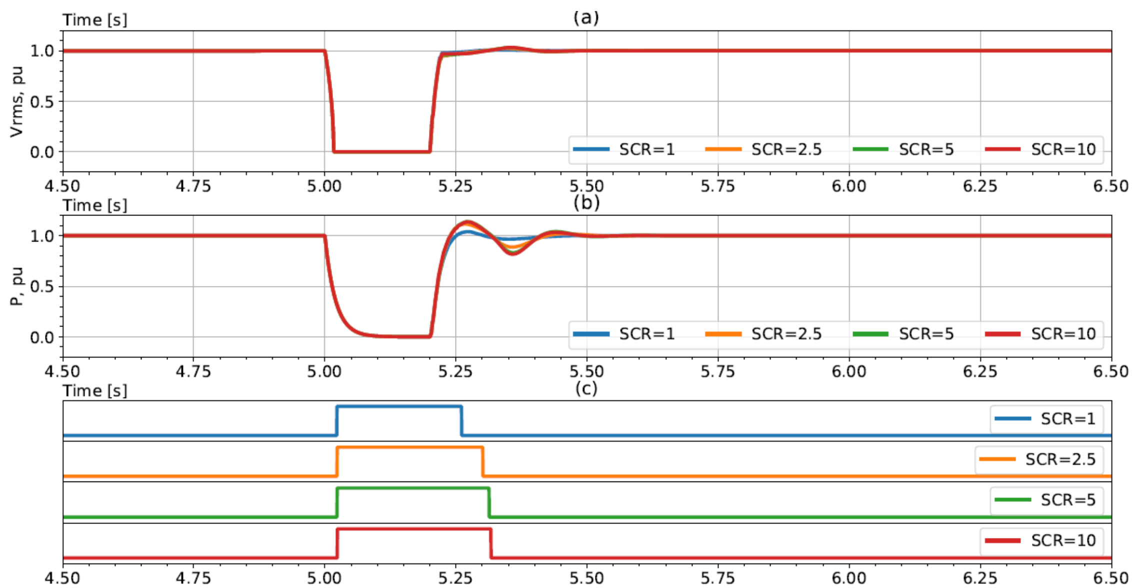

Figure 3-28 Adaptive fault ride through control on VSM with in-line Cascaded current control (a) ac voltage at PCC (b) active power output and (c) adaptive control switched on signals.

If adaptive fault ride through control is implemented with switchable current limiting, a similar improvement also accrues. The adaptive fault ride through control is activated when the current control loop is switched in. Figure 3-29 shows the results for SCRs ranging from 1 to 10, when the adaptive fault ride through control is used. Compared with the conventional switchable current limiting results shown in Figure 3-21, the proposed adaptive control method greatly improves the fault ride though performance of VSM with switchable current control connected to both weak and strong systems.

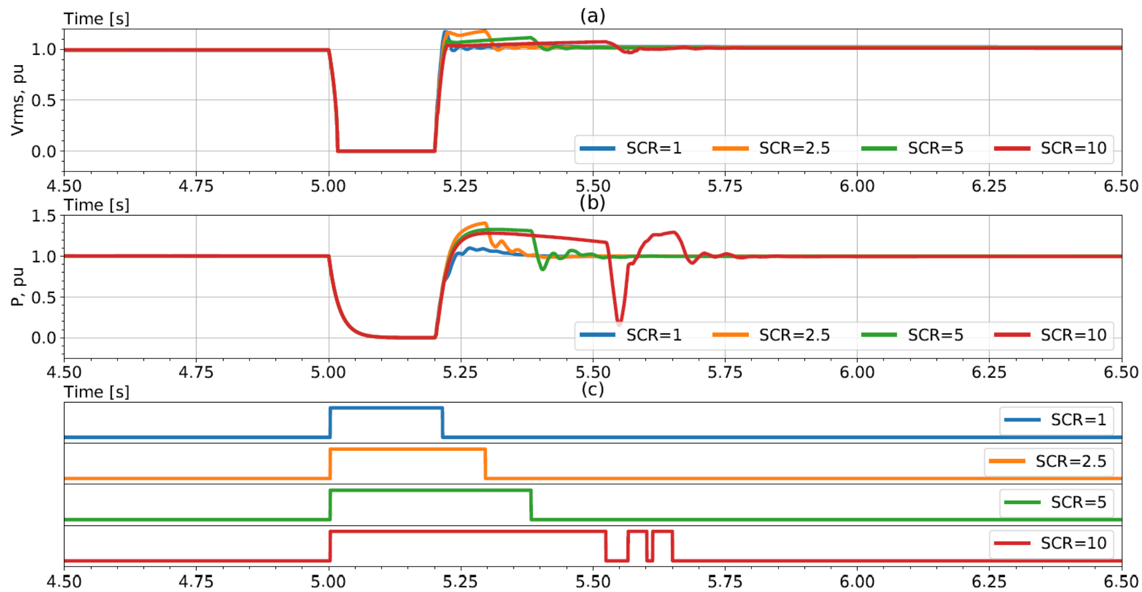

Figure 3-29 Adaptive fault ride through control on VSM with Switchable current control (a) ac voltage at PCC (b) active power output and (c) current control loop switch signal

3.5 Propose adaptive control method on VSM voltage phase angle shift ride through

In the previous section 3.2.2, the comparison of VSM and GFL response to the voltage phase angle shift has shown that the GFL shows fast-tracking behaviour, but VSM has a sluggish response with more oscillation and larger settling time. IEEE Standard 2800-2022 [27] demands that any VSC should be able to ride through a phase change in ac voltage of +/- 25 degrees.

Consider the same test system of Figure 3-4 used in the previous sections with SCR = 2.5. A phase angle shift is applied to the Thevenin equivalent voltage source to emulate the ac voltage phase angle change close to the PCC bus, which could be precipitated by some grid events e.g., power flow change. The phase of the ac source is reduced by 30 degrees at $t = 5\ s$, and then increased back to 0 degree at 7 s.

First, consider the case without the proposed adaptive control. and the in-line cascaded current control limiter set to 1.3 pu . In Figure 3-30, (a) is the voltage phase angle at PCC, (b) the ac current output and (c) the active power output from the converter. During the phase angle jump, overcurrent occurs, and when the current limiting remains on for too long, the controller loses the ability to lock synchronization voltage angle θ, VSM can lose synchronization and the system becomes unstable. In this case, the VSM inertia constant J is 5 s. The transient active power and ac current output change of VSM is large and the current limiting is activated starting at t = 5 s. The voltage angle loses synchronism and becomes unstable due to the current limiting shown in Figure 3-30 (a), (b) and (c).

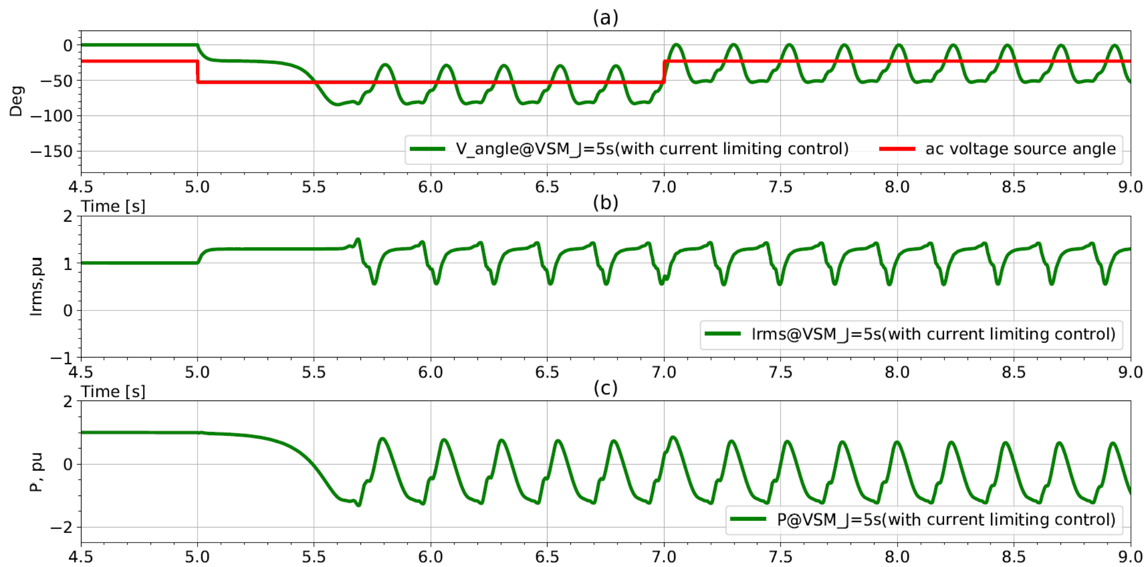

Figure 3-30 (without adaptive control) VSM (J=5 s) with cascaded current controls response to the connected ac voltage source phase jump. (a) ac voltage phase angle (b) ac current output and (c) active power output

Since the proposed adaptive fault ride through control can limit the synchronization voltage angle change during the overcurrent transient, it can also improve the VSM phase angle ride through performance. The simulation results with the proposed adaptive control are shown in Figure 3-31. The system is able to ride through the disturbance successfully, unlike the case without adaptive control in Figure 3-30. The voltage angle is frozen when the adaptive control is switched on during the overcurrent limiting period. When the overcurrent limiting is over, the inertia behaviour of the VSM resumes, and thus not jeopardizing the GFM functionality during normal operation. Same qualitative conclusion can be drawn if current limiting is achieved by switchable current limiting control.

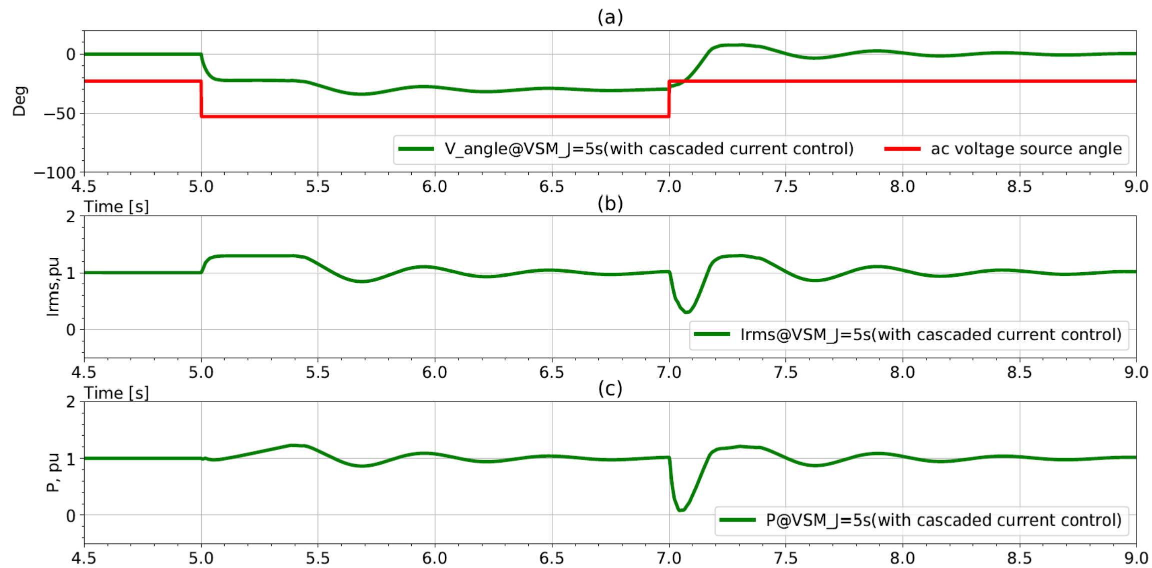

Figure 3-31 VSM (J=5 s) with cascaded current limiting and adaptive fault ride through controls response to the connected ac voltage source phase jump. (a) PCC voltage phase angle (b) ac current output (c) active power output and (d) adaptive fault ride through switched on signal

3.6 Summary

This chapter presents the VSM control for a VSC-HVdc link. A test system is developed on the EMT simulator PSCAD/EMTDC with VSM control on the HVdc inverter side. It shows that VSM control can have a similar inertia response as the synchronous machine and is supreme to GFL when connected to a weak ac system. However, VSM can introduce a damping coefficient related active power output deviation after system frequency changes, which actual synchronous machines do not. In comparison to a GFL converter, VSM can exhibit a slower response following a phase angle jump. The performance of two different VSM current limiting control strategies, switchable and in-line cascaded current control, are discussed. It shows that VSM with these two current limiting methods can fail to ride through the ac fault when the connected ac system is strong. Furthermore, due to the sluggish response of VSM, it can also fail to ride through when there is a sudden voltage phase angle shift. An adaptive control method dynamically changing the control gains is proposed in this thesis to improve both VSM ac fault and voltage phase angle ride through performance.

Chapter 4

Small Signal Stability Analysis of VSM

In this chapter, a linearized state-space VSM small-signal model is proposed and validated with the EMT model to investigate the control stability margin of VSM with and without a current limiting loop under various grid conditions and different ranges of control parameters. This analysis helps in the selection of VSM controller gains.

4.1 Equivalent circuit for the small-signal stability study

In most cases, one of the converters of an HVdc link is controlled to regulate the voltage on the interconnecting dc link. Assume that the remote converter is tasked thus then the local converter can be regarded as being connected to a constant dc voltage. Assuming that this converter is operating as an inverter as a VSM, the equivalent circuit for such operation is shown in Figure 4-1. This equivalent circuit is used for the small-signal stability study. The VSM system shown in the blue box can be represented as a voltage source $V_c\angle\delta$ connected to an equivalent reactance X which is the sum of the transformer leakage reactance X_t and the MMC arm reactance X_{arm}:

$$X = X_t + X_{arm} \tag{4.1}$$

On the grid side, the point of common coupling (PCC) bus voltage is $V_t\angle\theta$. And the ac grid is represented by a Thevenin equivalent voltage source $V_s\angle\varphi$ behind resistor R_s and inductor X_s. Changing R_s and X_s allows one to change the system strength as well as the impedance X/R ratio. The current and power flow positive direction is defined from the converter to the ac grid.

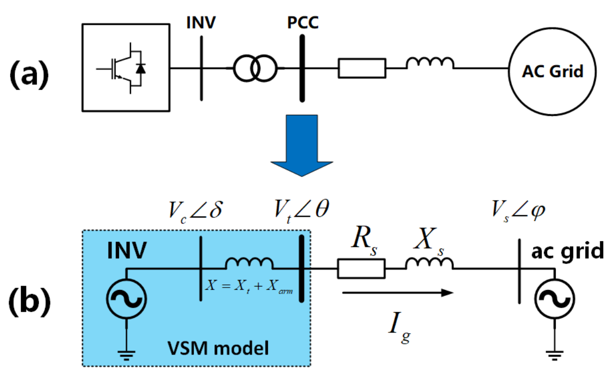

Figure 4-1 (a) VSM inverter arrangement and (b) small signal equivalent circuit

For the convenience of analysis, the voltage and current variables in the abc domain shown in Figure 4-1 are transferred into variables in dq domain as in Figure 4-2 using the Park's transformation matrix presented in Appendix A.1.

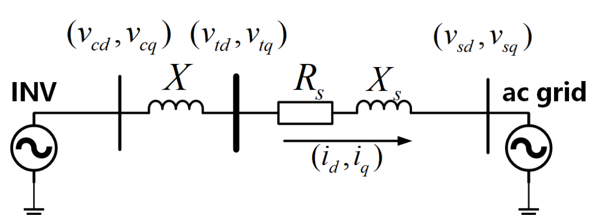

Figure 4-2 the Equivalent circuit in dq domain

4.2 State-space VSM model

The mathematical description of the dynamical behaviour of the system described in Section 4.1 contains both differential equations and algebraic equations. They are called differential-algebraic equations (DAEs), also known as descriptor systems [87]. DAEs are much easier to formulate as compared to classical state equations, as they can be formulated without eliminating algebraic equations [88]. The mathematical framework, descriptor state-space equations can be written as

$$\begin{aligned} E\dot{x} &= Ax + Bu \\ y &= Cx \end{aligned} \tag{4.2}$$

In (4.2), x presents the state, u is the input, and y is the output of the system, and the matrix E is generally singular and therefore non-invertible. Modern CAD tools such as Matlab allow to generate system eigenvalues of this system automatically using the matrix pencil (A, E) [89]. The matrix pencil eigenvalue set contains essential eigenvalues of finite magnitude that impact system dynamics and some additional eigenvalues of infinite magnitude the number of which equals the number of algebraic equations [90]. The essential eigenvalues are exactly the same as that would be obtained from a classical state variable formulation of the same system.

Based on the mathematical model described above, the system with a VSM can be linearized around the operating setpoint (e.g., $P_{ref} = 1\ pu, V_{ref} = 1\ pu$). The linearized stability analysis model for VSM with and without in-line cascaded current limiting control will be developed in the following sections.

4.2.1 Linearized model of VSM

The control diagram of VSM without current limiting control is shown in Figure 4-3. Initially, at an operating point $P_{ref} = 1\ pu, V_{ref} = 1\ pu$, the power synchronization controller can be linearized as

$$\frac{d\Delta\theta}{dt} = \Delta\omega_{vsm} \cdot \omega_0 \tag{4.3}$$

$$J\frac{d\Delta\omega_{vsm}}{dt} = \Delta P_{ref} - \Delta P_{meas} - D\Delta\omega_{vsm} \tag{4.4}$$

Note that, ω_0 is the nominal angular velocity at 376.99 rad/s, and the unit of θ is rad.

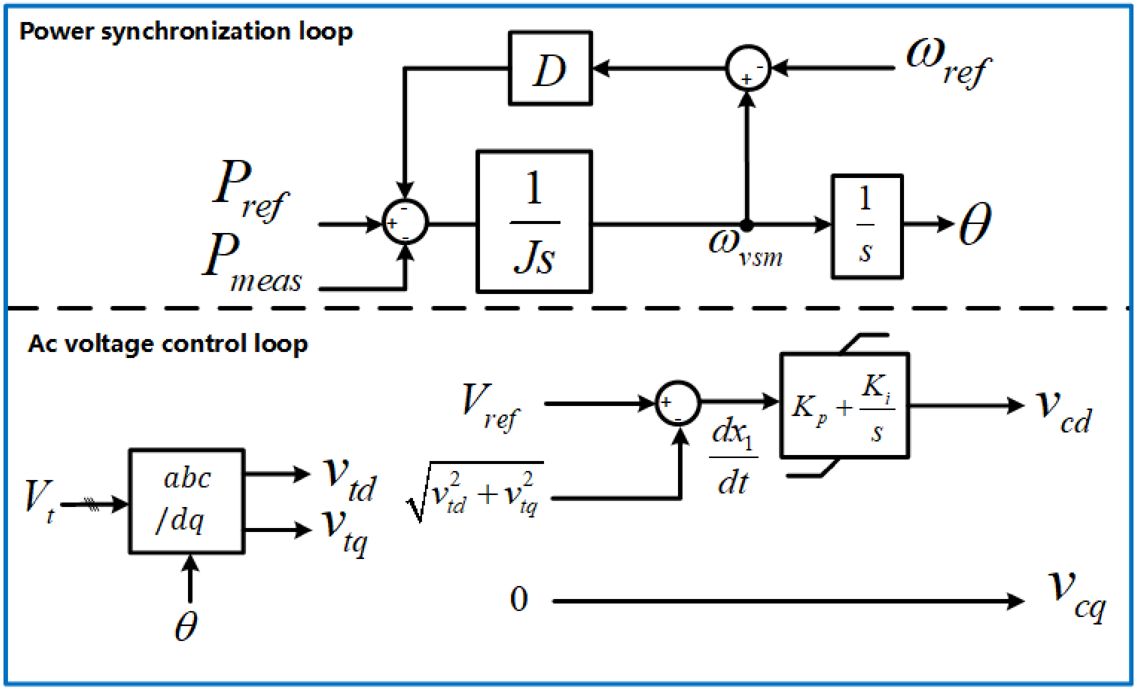

Figure 4-3 control diagram of VSM without in-line cascaded current control

Then, the network dynamic from the converter terminal to the PCC bus in dq domain can be expressed by

$$\frac{L}{\omega_0}\frac{d\Delta i_d}{dt} = \Delta v_{cd} - \Delta v_{td} - L i_q \Delta\omega_{vsm} - L\omega_{vsm}\Delta i_q \tag{4.5}$$

$$\frac{L}{\omega_0}\frac{d\Delta i_q}{dt} = \Delta v_{cq} - \Delta v_{tq} + L i_d \Delta\omega_{vsm} + L\omega_{vsm}\Delta i_d \tag{4.6}$$

In (4.5) and (4.6), L is the inductance in pu from VSM terminal to PCC bus. As in Figure 4-2, i_d, i_q is the current flow from the converter to the network, v_{cd}, v_{cq} is the voltage at the converter terminal, and v_{td}, v_{tq} is the voltage at PCC bus.

Similarly, the network dynamics from the PCC bus to the Thevenin equivalent voltage source in dq domain can be expressed by the following equations:

$$\frac{L_s}{\omega_0}\frac{d\Delta i_d}{dt} = \Delta v_{td} - \Delta v_{sd} - L_s i_q \Delta\omega_{vsm} - L_s\omega_{vsm}\Delta i_q - R_s\Delta i_d \tag{4.7}$$

$$\frac{L_s}{\omega_0}\frac{d\Delta i_q}{dt} = \Delta v_{tq} - \Delta v_{sq} + L_s i_d \Delta\omega_{vsm} + L_s\omega_{vsm}\Delta i_d - R_s\Delta i_q \tag{4.8}$$

In (4.7) and (4.8), L_s and R_s are the equivalent grid inductance and resistance from PCC bus to the Thevenin equivalent voltage source at V_{sd}, V_{sq}. The derivation of equations (4.5) to (4.8) is presented in Appendix A.2.

The voltage controller's input error is fed to Proportional Integral (PI) controller. The output x_1 of the PI's integrator is a useful state variable to use, and hence the input error is more conveniently represented as a derivative dx_1/dt. Next, if the VSM ac voltage controller input error is dx_1/dt and the proportional and integral gains of the PI controller are K_p and K_i, the controller can be linearized as

$$\frac{d\Delta x_1}{dt} = \Delta V_{ref} - \left(\frac{v_{td}}{\sqrt{v_{td}^2 + v_{tq}^2}} \Delta v_{td} + \frac{v_{tq}}{\sqrt{v_{td}^2 + v_{tq}^2}} \Delta v_{tq}\right) \tag{4.9}$$

$$0 = K_p\left(\Delta V_{ref} - \frac{v_{td}}{\sqrt{v_{td}^2 + v_{tq}^2}} \Delta v_{td} - \frac{v_{tq}}{\sqrt{v_{td}^2 + v_{tq}^2}} \Delta v_{tq}\right) + K_i \Delta x_1 - \Delta v_{cd} \tag{4.10}$$

$$0 = \Delta v_{cq} \tag{4.11}$$

After that, the relationship between v_{td}, v_{tq}, i_d, i_q and the measured active power P_{meas} at PCC bus can be linearized as

$$0 = v_{td} \cdot \Delta i_d + \Delta v_{td} \cdot i_d + v_{tq} \cdot \Delta i_q - \Delta P_{meas} \tag{4.12}$$

Finally, the relation between θ and v_{sd}, v_{sq} at ac voltage source can be linearized as

$$0 = V_m \sin(\varphi - \theta)\Delta\theta - \Delta v_{sd} \tag{4.13}$$

$$0 = V_m \cos(\varphi - \theta)\Delta\theta - \Delta v_{sq} \tag{4.14}$$

The derivation of (4.13) and (4.14) is shown in Appendix A.2.

Combining the equations from (4.3) to (4.14) in order can obtain the linearized model of GFM VSC without in-line cascaded current control in the linearized form $E\Delta\dot{x} = A\Delta x + B\Delta u$, where,

$$\Delta x = [\Delta\theta, \Delta\omega_{vsm}, \Delta i_d, \Delta i_q, \Delta x_1, \Delta v_{cd}, \Delta v_{cq}, \Delta v_{td}, \Delta v_{tq}, \Delta v_{sd}, \Delta v_{sq}, \Delta P_{meas}]^T \tag{4.15}$$

$$\Delta u = [\Delta P_{ref}, \Delta V_{ref}]^T \tag{4.16}$$

The E, A and B matrices are presented in Appendix B.1.

4.2.2 Linearized model of VSM with in-line cascaded current limiting control

Figure 4-4 shows the control diagram of VSM with in-line cascaded current control as described in section 3.3.2. Compared with the linearized model of VSM described in Section 4.2.1, the linearization process of the power synchronization controller and network dynamics remain the same for VSM with in-line cascaded current control. However, the linearization process of the ac voltage control loop is different when the cascaded current control loop is added. Note that in the linearized small signal model, the current control loop is assumed not to be limiting the current. If the current gets limited to a ceiling, the model is no longer valid.

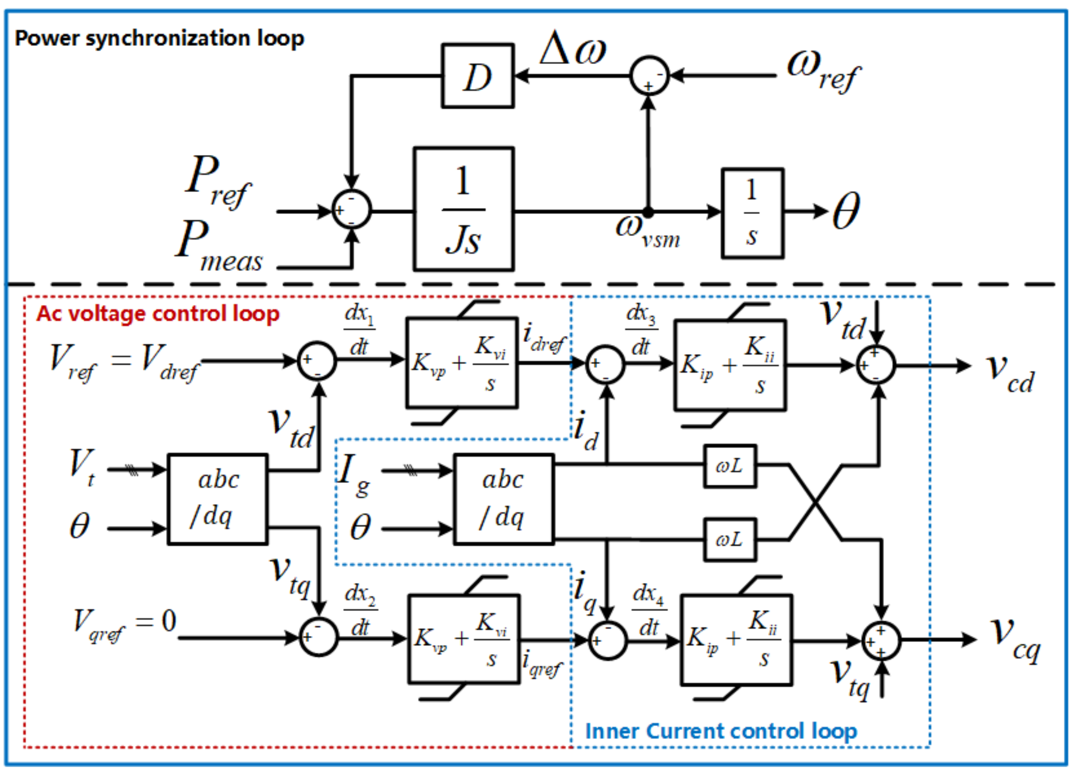

Figure 4-4 control diagram of VSM with in-line cascaded current control

Define dx_1/dt, dx_2/dt, dx_3/dt, dx_4/dt as the cascaded PI controller input errors which is shown in Figure 4-4, the outer loop controller can be linearized as

$$\frac{d\Delta x_1}{dt} = \Delta V_{ref} - \Delta v_{td} \tag{4.17}$$

$$\frac{d\Delta x_2}{dt} = -\Delta v_{tq} \tag{4.18}$$

$$0 = K_{vp}(\Delta V_{ref} - \Delta v_{td}) + K_{vi}\Delta x_1 - \Delta i_{dref} \tag{4.19}$$

$$0 = -K_{vp}\Delta v_{tq} + K_{vi}\Delta x_2 - \Delta i_{qref} \tag{4.20}$$

K_{vp} and K_{vi} are the proportional and integral gains for the outer loop PI controller.

Likewise, the inner loop controller can be linearized as

$$\frac{dx_3}{dt} = \Delta i_{dref} - \Delta i_d \tag{4.21}$$

$$\frac{dx_4}{dt} = \Delta i_{qref} - \Delta i_q \tag{4.22}$$

$$0 = K_{ip}(\Delta i_{dref} - \Delta i_d) + K_{ii}\Delta x_3 - \omega_0 L\Delta i_q + \Delta v_{td} - \Delta v_{cd} \tag{4.23}$$

$$0 = K_{ip}(\Delta i_{qref} - \Delta i_q) + K_{ii}\Delta x_4 + \omega_0 L\Delta i_d + \Delta v_{tq} - \Delta v_{cq} \tag{4.24}$$

Then, Combining the equations (4.17), (4.18), (4.21), (4.22), (4.3) to (4.8), (4.19), (4.20), (4.23), (4.24), (4.13), (4.14) in order can obtain the linearized model of VSM with in-line cascaded current control in the linearized form $E\dot{\Delta x} = A\Delta x + B\Delta u$, where,

$$\begin{aligned}\Delta x = [&\Delta x_1, \Delta x_2, \Delta x_3, \Delta x_4, \Delta\theta, \Delta\omega_{vsm}, \Delta i_d, \Delta i_q, \\ &\Delta v_{cd}, \Delta v_{cq}, \Delta v_{td}, \Delta v_{tq}, \Delta v_{sd}, \Delta v_{sq}, \Delta i_{dref}, \Delta i_{qref}, \Delta P_{meas}]^T\end{aligned} \tag{4.25}$$

$$\Delta u = [\Delta P_{ref}, \Delta V_{ref}]^T \tag{4.26}$$

The E, A and B matrices are presented in Appendix B.2.

4.2.3 Model verification

The time domain response of the linearized models of VSM developed without a current controller (Section 4.2.1) and with a in-line cascaded current controller (Section 4.2.2) can be obtained by numerically integrating the state equations. MATLAB is used for this purpose. To validate the linearized models, their precise time domain responses are compared with the time domain responses of the detailed models including all non-linearities. EMT simulator PSCAD/EMTDC is used for conducting the detailed simulations.

First consider VSM without current limiting as in Section 4.1, assuming the dc link voltage is constant. the MMC HVdc system shown in Figure 3-4 is modelled in the EMT simulator and used to validate the linearized model. The system parameters are presented earlier in Table 3-1, and the control parameters are presented below in Table 4-1. The operating point is initially selected at $P_{ref} = 1pu, V_{ref} = 1pu$. Then, at 5 s of the simulation, P_{ref} changes from 1 pu to 0.9 pu.

Inertia constant	5 s
Damping coefficient	20 pu
Ac voltage controller (K_p, K_i)	(0.1, 5) pu

Table 4-1 VSM control parameters

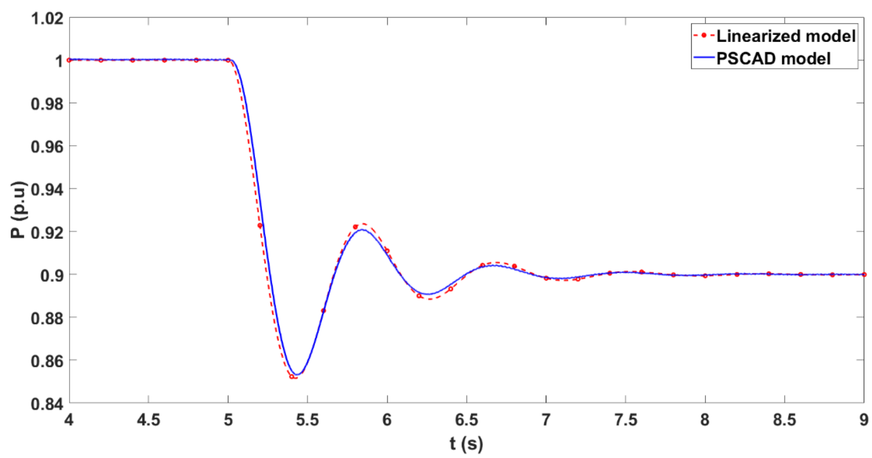

Figure 4-5 VSM active power output response to active power order step change from 1pu to 0.9pu for a weak system (SCR=1)

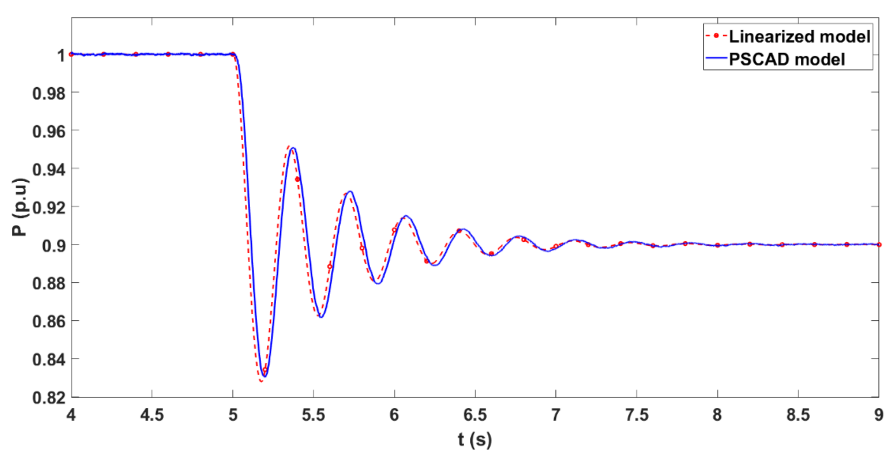

Figure 4-6 VSM active power output response to active power order step change from 1pu to 0.9pu for a strong system (SCR=10)

Figure 4-5 and Figure 4-6 show that the linearized model of VSM matches with the EMT model well connecting to both strong and weak ac systems. Figure 4-5 shows linearized and EMT model of VSM active power output response to the power order step change from 1 pu to 0.9 pu, the connected ac system is weak at SCR=1. Figure 4-6 shows the active power output responses when the connected ac system is strong at SCR=10.

Next, the linearized small-signal model of VSM with in-line cascaded current limiting controller presented in Section 4.1.2 is also validated similarly. The control parameters are shown below in Table 4-2.

Inertia constant	5 s
Damping coefficient	20 pu
Ac voltage controller (K_{vp}, K_{vi})	(7, 10) pu
Inner current controller (K_{ip}, K_{ii})	(0.5, 100) pu

Table 4-2 VSM with in-line cascaded current limiting control parameters

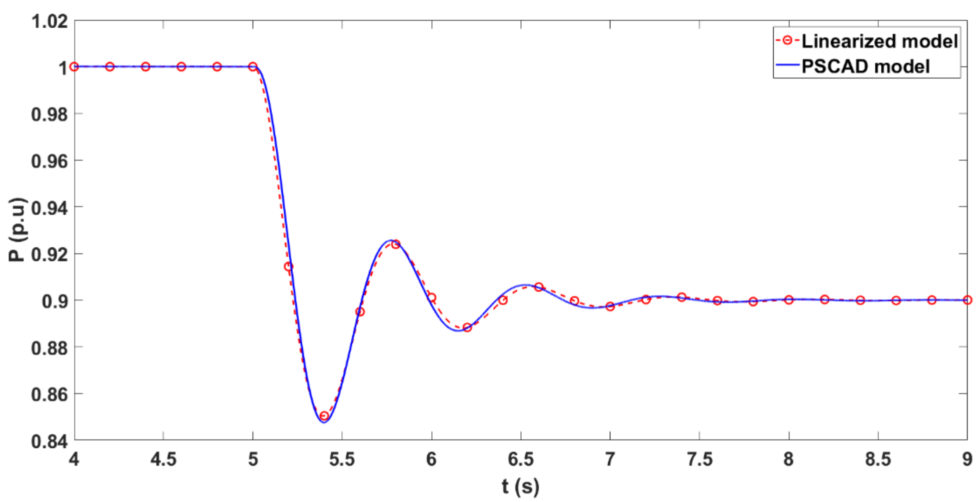

Figure 4-7 VSM (with in-line cascaded current control) active power output response to active power order step change from 1pu to 0.9pu for a weak ac system SCR=1

The linearized model of the VSM with in-line cascaded current control also matches well with the EMT model as shown in Figure 4-7 and Figure 4-8. However, it is interesting to see that the VSM controller is more undamped in strong grid conditions with the same control parameters. This is different from the GFL VSC applications that controls which are stable in weak grids are likely to be stable in strong grids as well. As mentioned earlier in Section 3.1, the VSM acts as a voltage source, which makes it challenging to connect to a strong ac network that also behaves as a voltage source. Even a slight deviation in the VSM source's phase angle results in a significant current change, which contributes to reduced stability when operating within a strong system. However, when employing an in-line cascaded current control, this problem becomes more serious as it introduces additional transfer function blocks in series, potentially resulting in a slower response. In the following sections, more details of the VSM control characteristics are shown by the eigenvalue analysis.

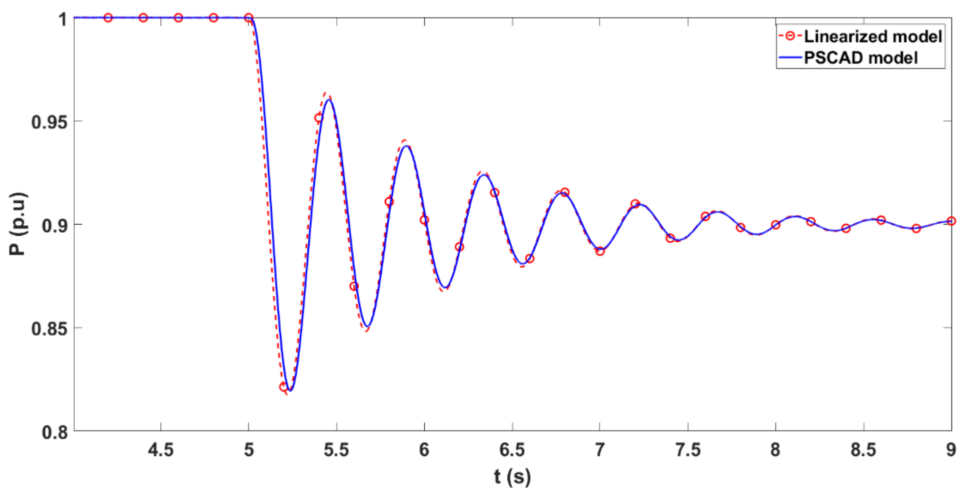

Figure 4-8 VSM (with in-line cascaded current control) active power output response to active power order step change from 1pu to 0.9pu for a strong ac system SCR=10

4.3 Impact of the ac system impedance on VSM stability

The impact of the equivalent ac system impedance R_s and X_s shown in Figure 4-1 on VSM will be explained in Sections 4.3.1 and 4.3.2. For an impedance $Z_s = |R_s + jX_s|\angle\sigma$, the ac system strength is inversely proportional to the impedance magnitude $|R_s + jX_s|$. A large impedance implies a low SCR and makes the system weak. The impedance angle σ can be represented by the X/R ratio $R_{X/R}$, where $R_{X/R} = \tan\sigma$. High impedance X/R ratio means large impedance angle.

4.3.1 System strength (system impedance magnitude)

To check the impact of the system strength or the system impedance magnitude on VSM stability, the SCR is used as the system strength indicator. The system operating point is at $P_{ref} = 1pu, V_{ref} = 1pu$. The system impedance angle is selected at 80º ($R_{X/R} = 5.67$). Other system and controller parameters remain the same as in section 4.2.2. Figure 4-9 shows the eigenvalues locus of VSM ***without*** in-line cascaded current control when SCR changes from 1 to 10. Although some of the eigenvalues move towards the right half plane (RHP), the system maintains stability in a strong grid condition. However, the system becomes more undamped when the ac system becomes stronger, this can be observed by comparing the time domain responses in Figure 4-5 and Figure 4-6.

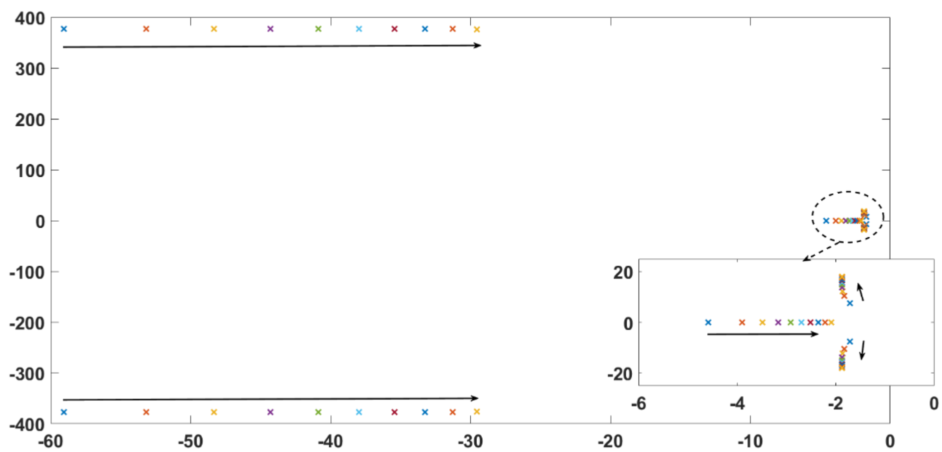

Figure 4-9 eigenvalue locus of VSM when SCR changes from 1 to 10

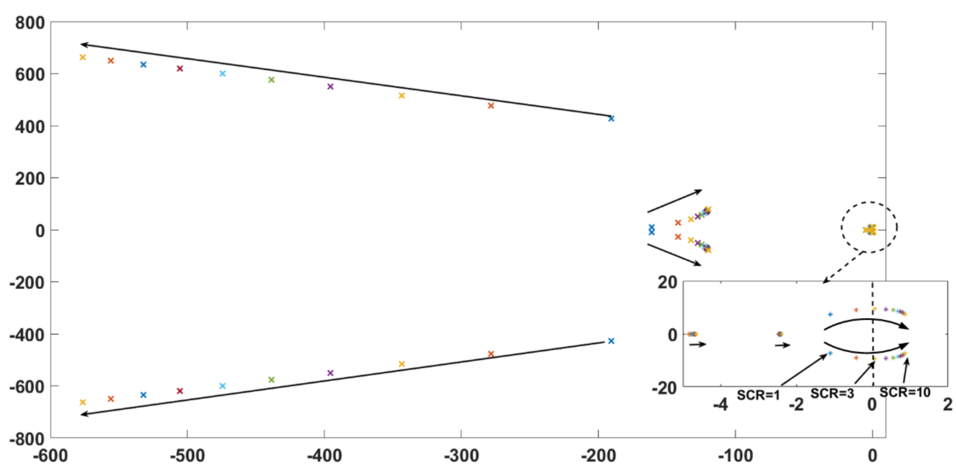

Figure 4-10 eigenvalue locus of an unstable VSM design ***with*** *in-line cascaded current control when SCR>2.8 (J=5s, D=20 pu, Kvp=3, Kvi=10, Kip=0.5, Kii=100)*

Next, the eigenvalue locus of VSM ***with*** in-line cascaded current control is also obtained as in Figure 4-10. When SCR changes from 1 to 10, some of the eigenvalues close to the origin cross into RHP as the SCR approaches 2.8. This implies that the system is only stable when connected to a weak grid. Thankfully, as shown in Figure 4-11, the controller can be retuned with gains that give stable operation at low SCR values. Compared with the VSM ***without*** the current control, the control parameters for VSM ***with*** in-line cascaded current controller must be more cautiously selected to avoid instability in a strong ac grid condition.

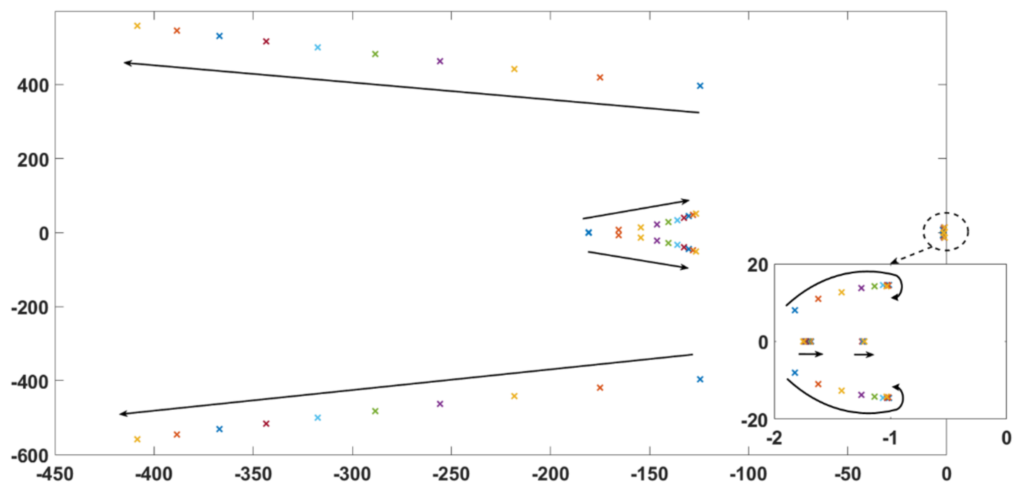

Figure 4-11 eigenvalue locus of VSM ***with*** *in-line cascaded current control when SCR changes from 1 to 10*

4.3.2 X/R ratio (grid impedance angle)

This section investigates the stability of the system as a function of the ratio of the real and reactive parts of the ac system's Thevenin impedance. Figure 4-12 and Figure 4-13 show the eigenvalue loci of VSM ***with*** and ***without*** the in-line cascaded current controller when the ac grid impedance angle changes from 0 to 90º(i.e., X/R ratio changes from 0 to ∞), with the ac system's SCR magnitude retained at 1.5, and other system and controller parameters remain the same.

The eigenvalue analysis shows both VSM ***with*** and ***without*** in-line cascaded current control maintain stability with the full range of impedance X/R ratio. However, when the system is almost completely resistive ($R_{X/R} = 0$, or angle $\sigma = 0^o$) or almost completely inductive ($R_{X/R} = \infty$, or angle $\sigma = 90^o$), a critical pole is very close to the RHP, but never crosses over. In high SCR situations, the eigenvalue locus has an identical trend and is thus not repeated here.

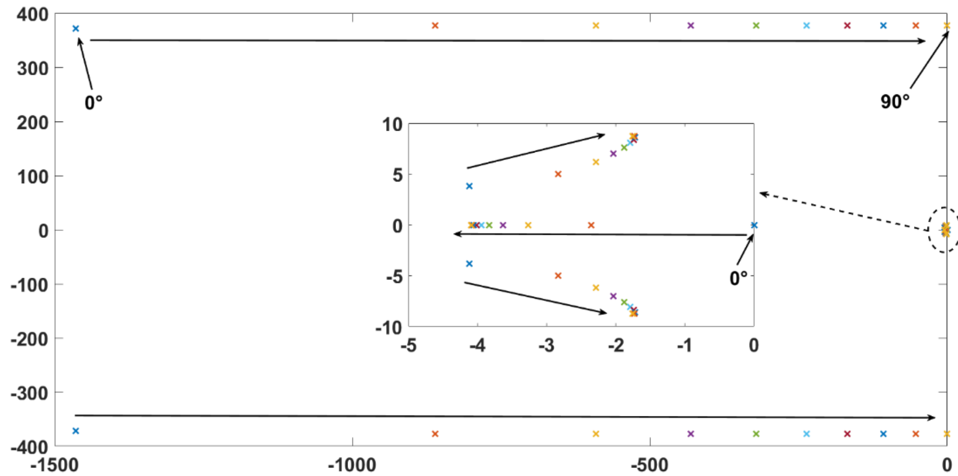

Figure 4-12 eigenvalue locus of VSM when grid impedance angle changes from 0 to 90^o (X/R changes from 0 to ∞)

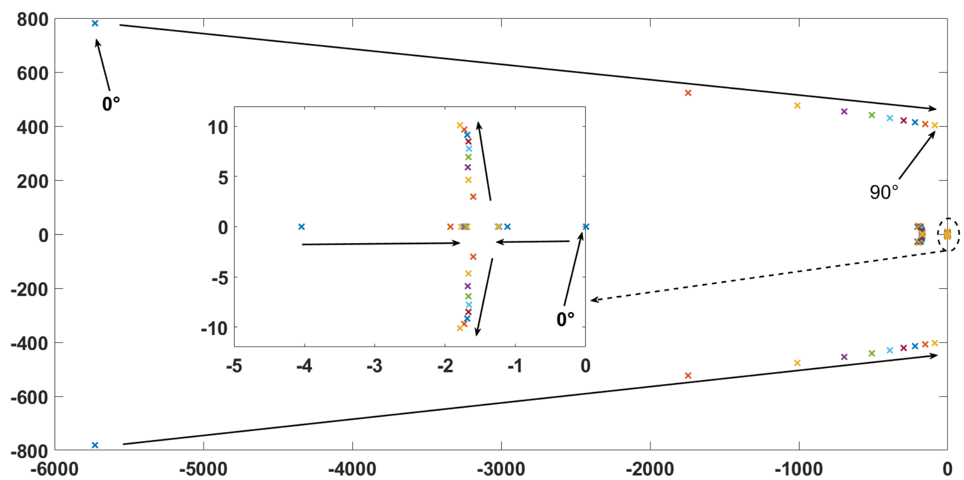

*Figure 4-13 eigenvalue locus of VSM **with** in-line cascaded current control when grid impedance angle changes from 0 to 90^o (X/R changes from 0 to ∞)*

4.4 Impact of control parameters on VSM stability

In the previous section 4.3, the impact of the ac system impedance on VSM was investigated. This section will investigate the impact of controller parameters on the system stability. In the study, if not mentioned specifically, the system operating point is at $P_{ref} = 1\ pu, V_{ref} = 1\ pu$. The ac system SCR is at 1 and the system impedance angle is 80º. The initial control parameters of VSM ***with*** and ***without*** current control are selected as in Table 4-1 and Table 4-2.

4.4.1 inertia constant J

Figure 4-14 and Figure 4-15 show the eigenvalue locus when the inertia constant J in Figure 4-3 and Figure 4-4 changes from 0 to 20 s. The plots are shown for VSM ***with*** and ***without*** the in-line cascaded current limiter. Some eigenvalues move closer to the origin for the case ***without*** in-line cascaded current control as J becomes larger. The same trend happens for VSM ***with*** in-line cascaded current limiting. This implies that the inertia constant for VSM should not be made excessively large as this can lessen the system damping.

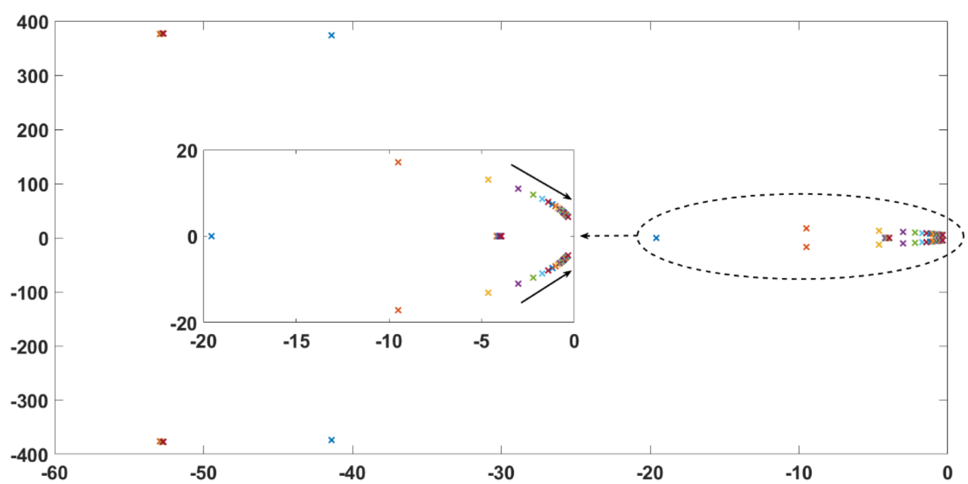

Figure 4-14 eigenvalue locus of VSM when the virtual inertia constant J changes from 0 to 20

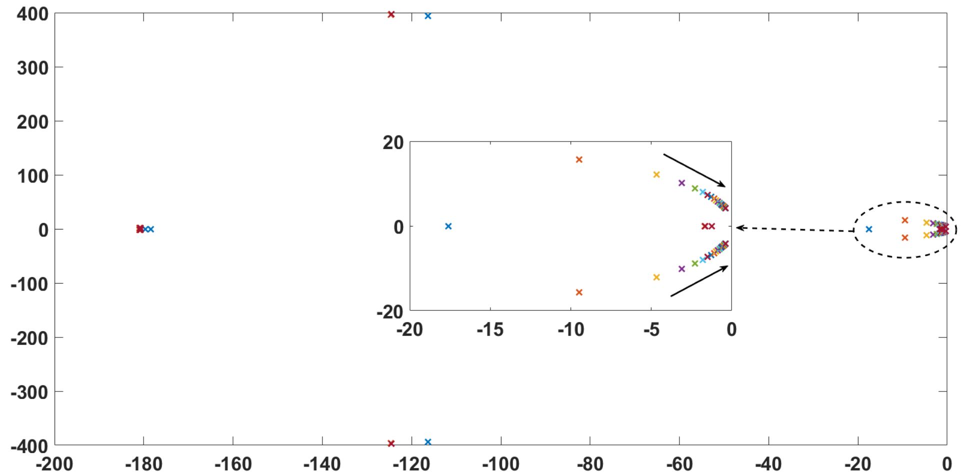

*Figure 4-15 eigenvalue locus of VSM **with** in-line cascaded current control when the virtual inertia constant J changes from 0 to 20*

4.4.2 Damping coefficient *D*

Figure 4-16 and Figure 4-17 show the eigenvalue loci when the damping coefficient D of VSM changes from 0 to 200 pu for a weak system (SCR=1). From the figures, the eigenvalues associated with a small damping coefficient lie on the RHP for both VSM with and without in-line cascaded current control (D<3 in Figure 4-16 and D<2 in Figure 4-17). Thus, to avoid system instability, the damping coefficient D of VSM controller should not be too small. This is different from the case in a real synchronous machine in which the damping coefficient is usually smaller than 1 pu [48].

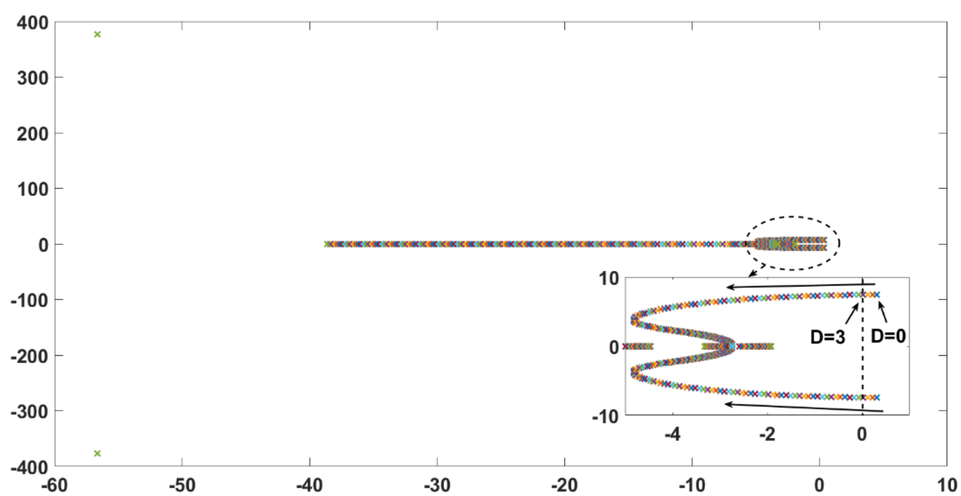

*Figure 4-16 eigenvalue locus of VSM when the damping coefficient D changes from 0 to 200 for a **weak** system (SCR=1)*

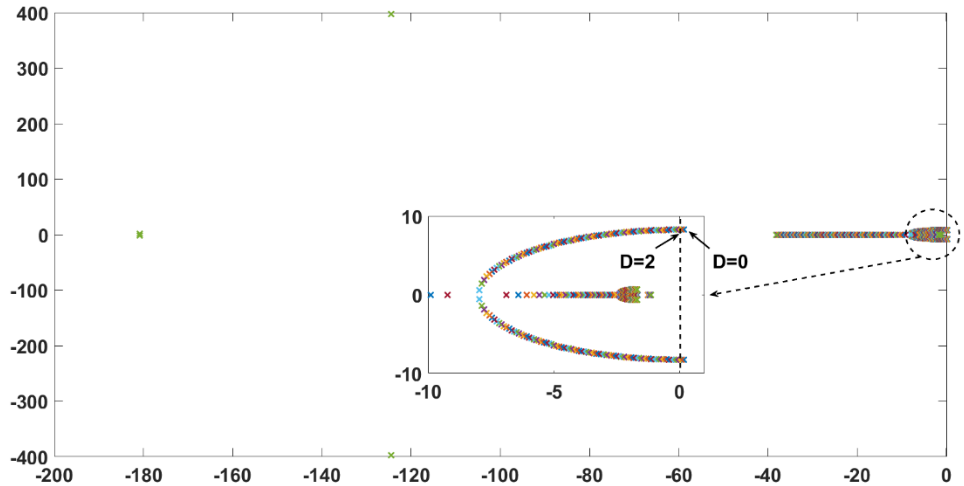

*Figure 4-17 eigenvalue locus of VSM **with** in-line cascaded current control when the damping coefficient D changes from 0 to 200 for a **weak** system (SCR=1)*

Figure 4-18 and Figure 4-19 show the eigenvalue loci when the damping coefficient D changes from 0 to 200 pu for a strong system (SCR=10). The critical D required to keep the system stable must be at least 1 pu for VSM ***without*** current control as in Figure 4-18. Thus, increasing system strength will slightly decrease the critical D for VSM ***without*** current control. However, for VSM ***with*** current control, the critical D must be greater than 9 pu as in Figure 4-19. Hence, a larger system strength requires a larger damping coefficient to remain stable compared with the case ***without*** current control. So, a VSM ***with*** current control should be designed with an appropriately large D (20-50 pu).

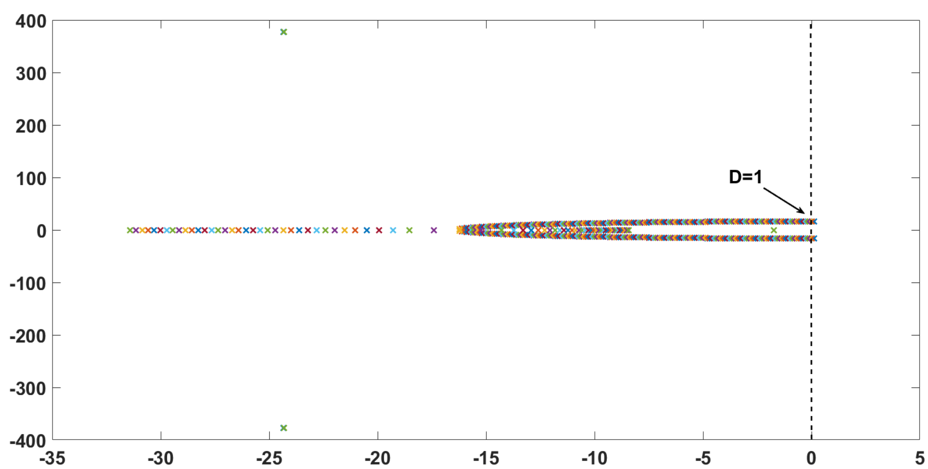

*Figure 4-18 eigenvalue locus of VSM when the damping coefficient D changes from 0 to 200 for a **strong** system (SCR=10)*

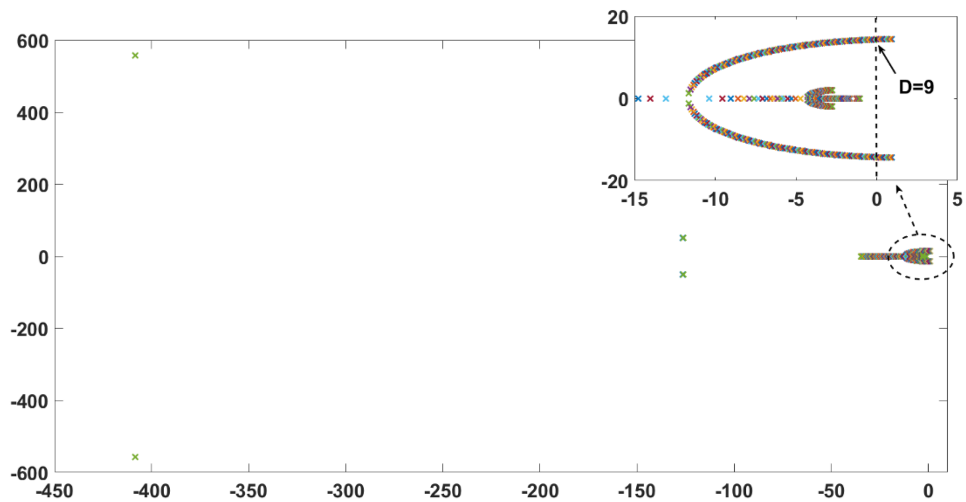

*Figure 4-19 eigenvalue locus of VSM **with** in-line cascaded current control when the damping coefficient D changes from 0 to 200 for a **strong** system (SCR=10)*

4.4.3 Ac voltage controller gains

This section investigates the impact of ac voltage controller gains of VSM ***with*** and ***without*** in-line cascaded current control on system stability.

Figure 4-20 and Figure 4-21 show the eigenvalue loci of VSM ***without*** in-line cascaded current control for a weak system (SCR =1) with varying ac voltage controller gains varying over a wide range. The proportional gain K_p changes from 0 to 10 in Figure 4-20 and the integral gain K_i changes from 0 to 100 in Figure 4-21. The system is stable for all gain values as no eigenvalue crosses to the RHP.

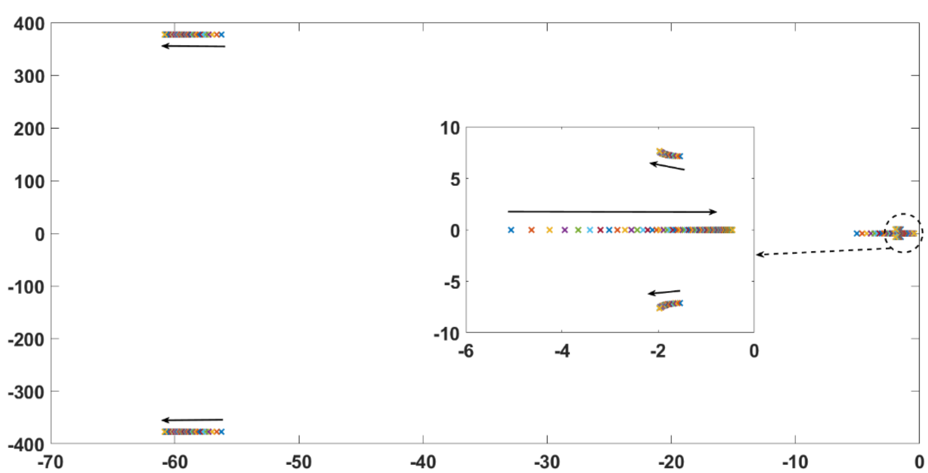

*Figure 4-20 eigenvalue locus of VSM with ac voltage controller proportional gain Kp ranges from 0 to 10 for a **weak** system (SCR=1) **without** Current Controller*

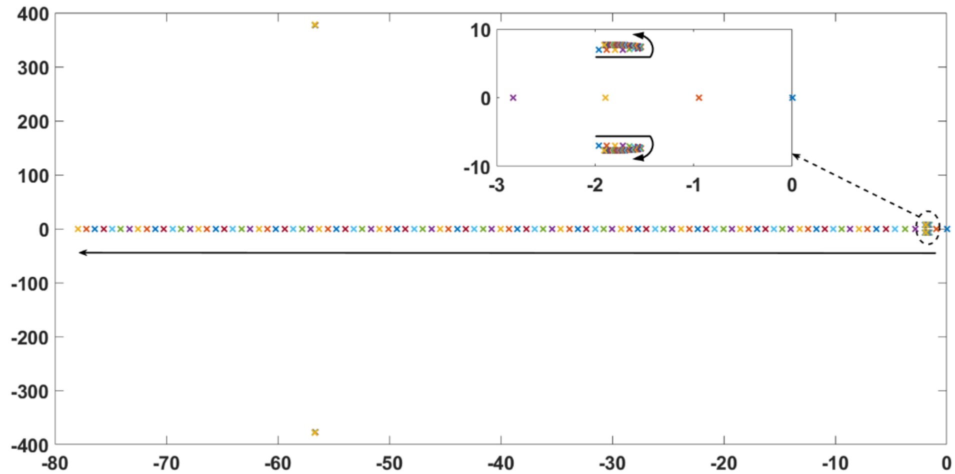

*Figure 4-21 eigenvalue locus of VSM with ac voltage controller integral gain Ki ranges from 0 to 10 for a **weak** system (SCR=1) **without** Current Controller*

The control diagram ***with*** the cascaded in-line current controller is shown in Figure 4-4. It has two loops. the outer loop is a voltage controller which generates the d and q-axis current references for the inner current control loop.

when the connected ac system is weak (SCR=1), to avoid system instability, the outer loop proportional gain K_{vp} needs to be larger than 1.8 and the outer loop integral gain K_{vi} can be selected in a much wider range (0-100). This can be observed in the eigenvalue loci of Figure 4-22 and Figure 4-23.

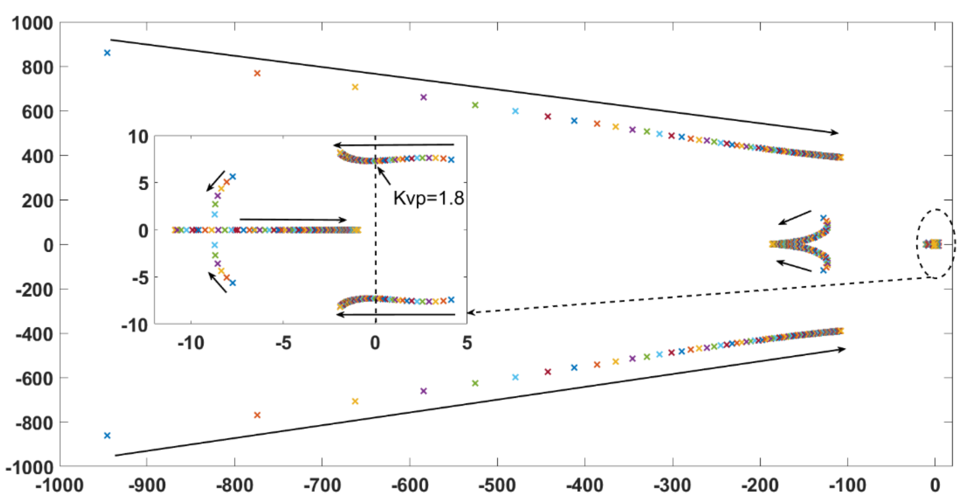

*Figure 4-22 eigenvalue locus of VSM with ac voltage controller gain Kvp ranging from 0 to 10 for a **weak** system (SCR=1) **with** Current Controller*

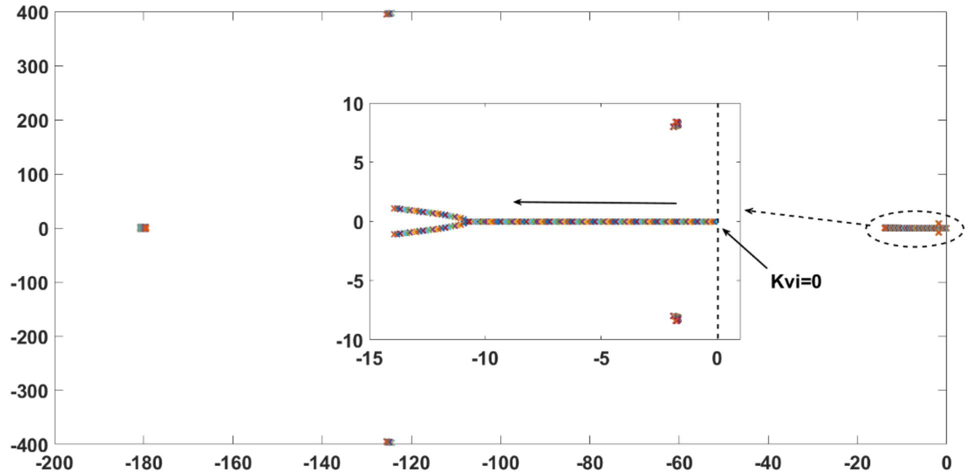

*Figure 4-23 eigenvalue locus of VSM with ac voltage controller gain Kvi ranging from 0 to 100 for a **weak** system (SCR=1) **with** Current Controller*

However, ***with*** the cascaded current control, the ac voltage controller gains of VSM for the strong system (SCR = 10) should be tuned more carefully to avoid instability. Figure 4-24 and Figure 4-25 show the eigenvalue loci of VSM for this condition as K_{vp} and K_{vi} change. K_{vp} should be larger than 4 and K_{vi} should be smaller than 21 to avoid the RHP eigenvalues. Nevertheless, as shown by in Figure 4-11 derived in section 4.3.1 for $K_{vp} = 7$ and $K_{vi} = 10$, it is still possible to select appropriate K_{vp} and K_{vi} which will provide stable operation in the strong system and will still provide stable operation in the weak system.

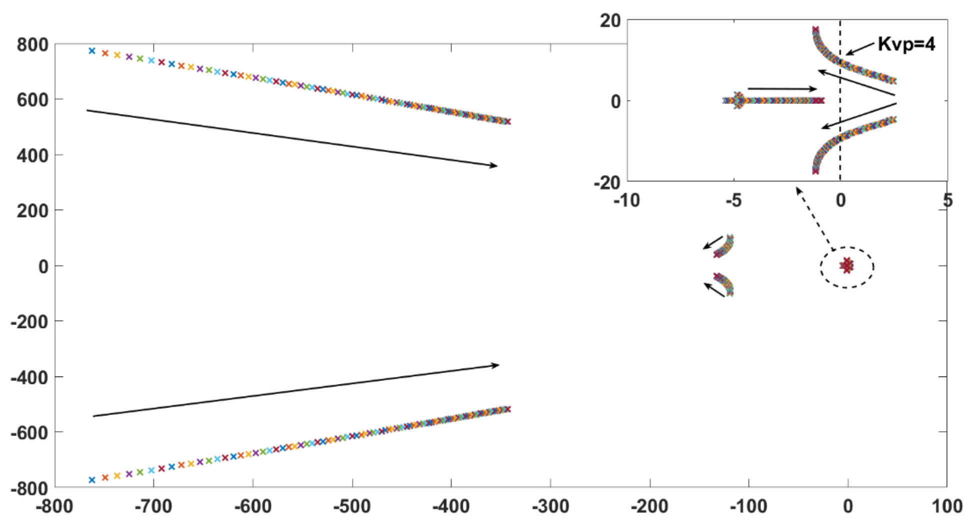

*Figure 4-24 eigenvalue locus of VSM with ac voltage controller gain Kvp ranging from 0 to 10 for a **strong** system (SCR=10) **with** Current Controller*

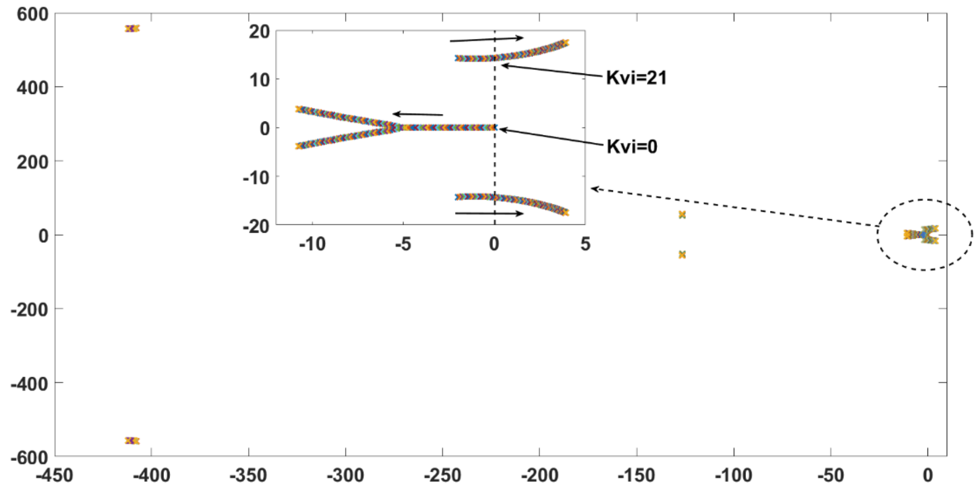

*Figure 4-25 eigenvalue locus of VSM with ac voltage controller gain Kvi ranging from 0 to 100 for a **strong** system (SCR=10) **with** Current Controller*

4.4.4 Inner current controller gains

Figure 4-26 and Figure 4-27 show the eigenvalue loci with changing inner current controller gains for VSM with in-line cascaded current control as shown in Figure 4-4 when the converter connects to a weak ac system (SCR=1). The proportional gain K_{ip} changes from 0 to 10 in Figure 4-26, and the integral gain K_{ii} changes from 0 to 1000 in Figure 4-27. Although some eigenvalues move closer the origin, they never cross over the RHP. Thus, the system is stable in the tested range of the inner current controller gains K_{ip} and K_{ii}.

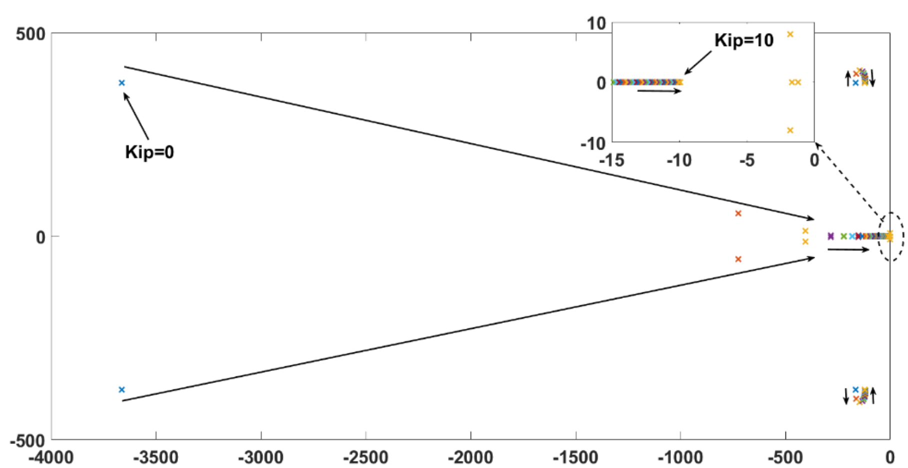

*Figure 4-26 eigenvalue locus of VSM with the current controller proportional gain Kip ranging from 0 to 10 for a **weak** system (SCR=1)*

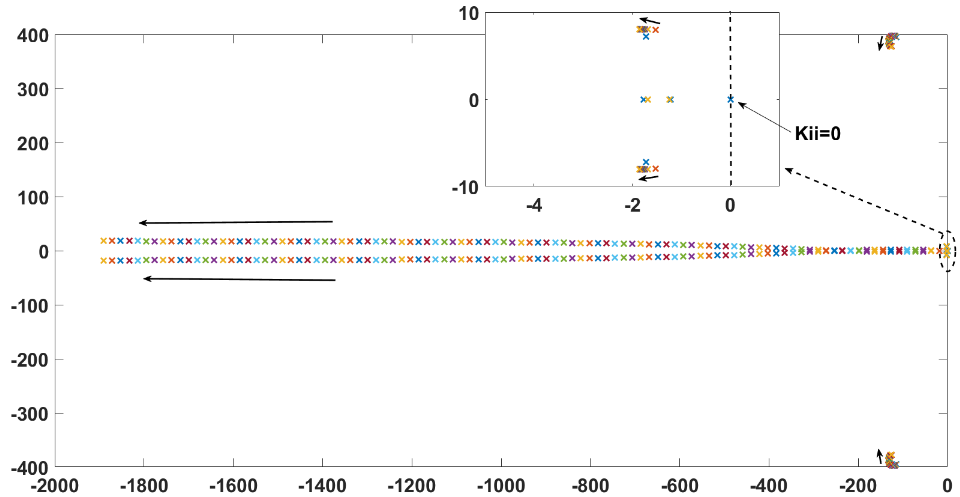

*Figure 4-27 eigenvalue locus of VSM with the current controller integral gain Kii changes from 0 to 1000 for a **weak** system (SCR=1)*

Figure 4-28 and Figure 4-29 show the situation for connecting to a strong system (SCR=10). The system also remains stable in the tested range of K_{ip} and K_{ii}, as some of the eigenvalue move closer to the origin but never cross over the RHP. Hence, for both strong and weak systems, the inner current controller can have a wide range of controller gains and maintain system stability.

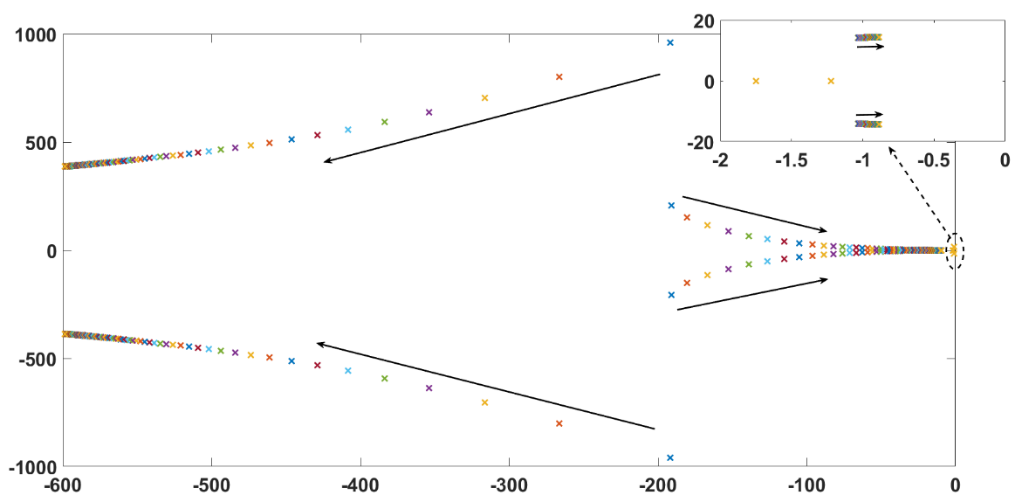

*Figure 4-28 eigenvalue locus of VSM with the current controller proportional gain Kip changes from 0 to 10 for a **strong** system (SCR=10)*

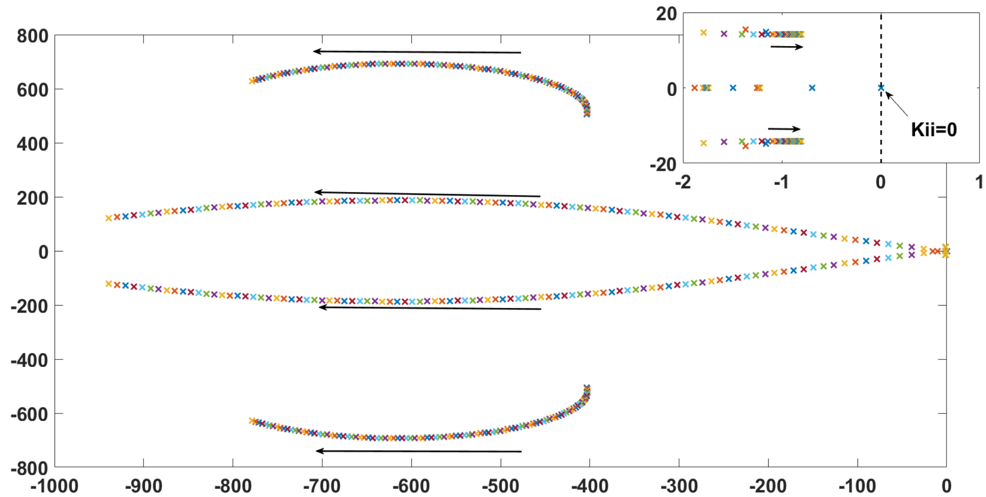

Figure 4-29 eigenvalue locus of VSM with the current controller integral gain Kii changes from 0 to 1000 for a ***strong*** *system (SCR=10)*

4.5 Suggested VSM control parameters

It is beneficial to have one set of gains that gives stable performance over the range of expected SCRs, without having to adaptively change them if the SCR changes. Based on the eigenvalue studies in the previous sections of this chapter, the suggested VSM control parameters range are shown below in Table 4-3. They give stable performance for SCRs ranging from 1.0 to 10.0, but if a particular inertia is selected, then the other parameters may have to tuned within their range to get good damping.

GFM control parameters	Suggested values
Inertia J	0.5 – 10 s
Damping coefficient D	20 – 50 pu
Voltage controller K_{vp}	5 – 7 pu
Voltage controller K_{vi}	10 – 20 pu
Current controller K_{ip}	0.5 – 1 pu
Current controller K_{ii}	100 - 600 pu

Table 4-3 Suggested VSM control parameters

4.6 Summary

This chapter developed linearized models of the VSM with and without in-line cascaded current control for system small-signal stability analysis. The proposed linearized model is thoroughly validated using detailed EMT simulation, thereby unequivocally establishing its applicability. The eigenvalues analysis shows that the stability of VSM becomes poorer with a large inertia constant. Thus, the inertia constant for VSM should not be made excessively large. When the in-line cascaded current controller is present, the VSM is more stable for the weak system and can experience unstable operation with a stronger system strength. However, the excellent news is that a single suitable gain parameter set can nevertheless be found to allow stable operation when connected to weak as well as strong ac systems.

Chapter 5

Inertia Measurement of an IBR System

This chapter proposes a new method to measure the inertia from IBRs and discusses the frequency support provided to a low inertia ac system by VSM and GFL HVdc converters. First, a new probing frequency injection-based method is proposed to measure synchronous machine inertia. Then, the proposed new method is further tested on a VSM to quantify its inertia. Next, a low inertia IBR system is developed first to investigate the inertia contribution provided by a GFL and then to do the same for a VSM, so that the two contributions can be compared. Finally, the proposed probing frequency injection method is used on the IBR system with a mix of actual and virtual synchronous machines.

5.1 Synchronous machine inertia

System inertia refers to the property of a power system that opposes changes in the rate of change of its rotational kinetic energy caused by a mismatch between the generation and consumption of active power.

Inertia in a synchronous machine is related to the kinetic energy stored in the rotating mass. This stored energy can be used to help maintain the stability and frequency of the power system in the event of disturbances such as sudden changes in power generation or consumption. The higher the synchronous machine inertia, the more energy is stored in the rotating masses and the better the system can resist changes in power generation or consumption. In [48], the inertia constant H (unit: second in per unit) is defined by

$$H = \frac{stored\ energy\ at\ rated\ speed\ in\ MW \cdot s}{MVA\ rating} = \frac{J}{2} \cdot \frac{\omega_0^2}{VA_{base}} \tag{5.1}$$

In the preceding chapters of this thesis, the swing equation used the moment of inertia J. However, in this chapter, for the sake of consistency with the conventional definition, the measured or calculated inertia constant is represented by the per-unit quantity $H = J/2$.

In some cases, the mechanical structure and the kinetic energy stored in a synchronous machine are not always known. However, the inertia constant H of a synchronous machine can also be measured from the system dynamics. Two methods are proposed in the following two sections.

5.1.1 Proposed probing frequency injection method

In a synchronous machine, the transfer function between electrical power deviation $\Delta P(s)$ and speed variation $\Delta\Omega(s)$ is

$$\frac{\Delta\Omega(s)}{\Delta P(s)} = -\frac{1}{Js + D} = -\frac{1}{2Hs + D} \tag{5.2}$$

Thus, in the frequency domain, equation (5.2) can be rewritten as

$$\frac{|\Delta P(\omega)|}{2\omega|\Delta\Omega(\omega)|} = \left| H + \frac{D}{2j\omega} \right| \tag{5.3}$$

Here, ω is the frequency deviation from the fundamental frequency ω_0. The damping coefficient D for a synchronous machine is usually very small and so $\frac{D}{2j\omega} \approx 0$. Thus, equation (5.3) can be used to estimate the inertia constant H. A small voltage signal V_h or current signal I_h at a probing frequency ω_h is injected at the terminal of the synchronous machine as shown in Figure 5-1. This results in the power deviation $\Delta P(\omega_0 - \omega_h)$ and a speed deviation $\Delta\Omega(\omega_0 - \omega_h)$ at frequency $\omega = \omega_0 - \omega_h$ and is then used to estimate $H \approx \frac{|\Delta P(\omega)|}{2\omega|\Delta\Omega(\omega)|}$. Since the purpose of the probing frequency injection is to get the power and system at a frequency ω, either current or voltage injection can fulfil this task.

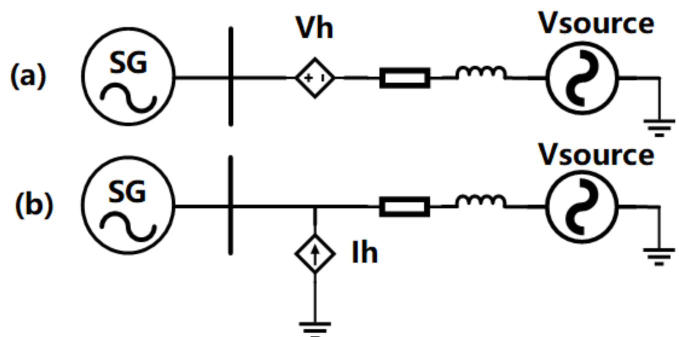

Figure 5-1 Probing frequency injection (a) Voltage injection (b) Current injection

To test this probing frequency injection method, a 100MVA synchronous machine with inertia constant $H = 3s$ connecting to a 10kV voltage source at a nominal frequency of $f_0 = \omega_0/2\pi = 60Hz$ is simulated in PSCAD/EMTDC. A small voltage signal tuned at $f_h = 10Hz$ and 10% of the voltage source magnitude is injected as shown in Figure 5-1 (a). Figure 5-2 shows the measured synchronous machine active power output P and rotating speed ω. After performing a Discrete Fourier Transform (DFT) on the measured power and frequency signals, frequency content of $f_0 - f_h = 50Hz$ is observed, with $|\Delta P(\omega)| = 2.4\,pu$ and $|\Delta\Omega(\omega)| = 0.00128\,pu$ as shown in Figure 5-3. According to equation (5.3), the inertia constant H can be calculated by

$$H \approx \frac{|\Delta P(\omega)|}{2\omega|\Delta\Omega(\omega)|} = \frac{2.4}{2\cdot(2\cdot\pi\cdot 50)\cdot 0.00128} s = 3s \qquad (5.4)$$

This measurement completely agrees with the inertia H of 3s of the machine, thereby validating the approach. A small current probing signal injection shown in Figure 5-1(b) also gives the same inertia constant of 3 s (not shown).

Compared with RoCoF observation method, the advantage of using this probing frequency injection method to measure inertia is that no load or generation change is required to check system RoCoF. The system inertia can be measured online at steady-state operation.

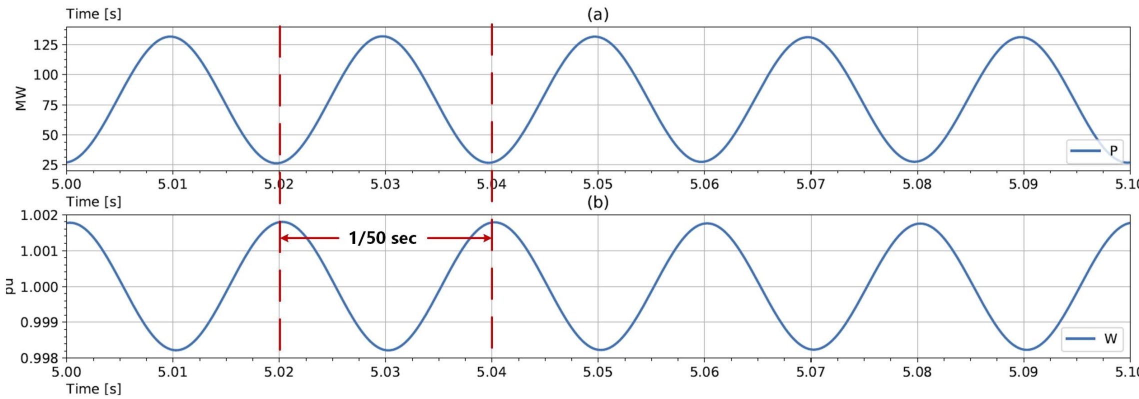

Figure 5-2 measured (a) the synchronous machine active power output (b) synchronous machine rotating speed.

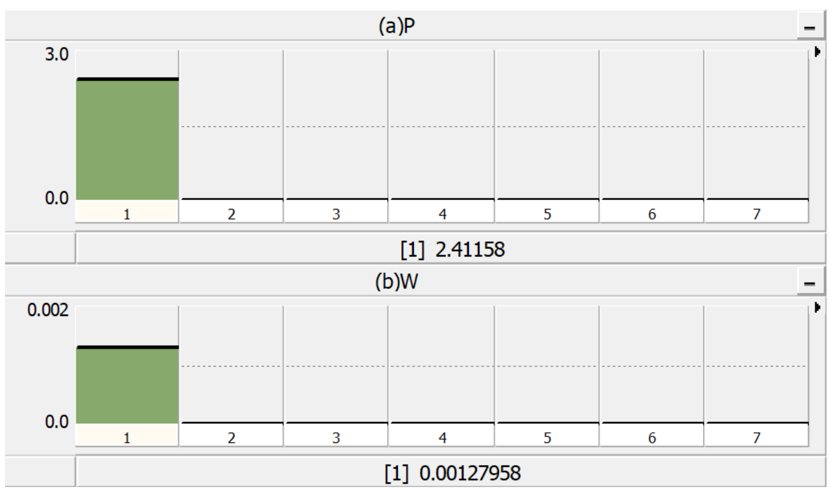

Figure 5-3 DFT on (a) active power output of synchronous machine (b) synchronous machine rotating speed, the fundamental frequency of DFT at 50 Hz.

The above method can be extended to measure the aggregated inertia response of a cluster of machines as well as the inertia of a system with IBRs.

5.1.2 Proposed method compared with inertia estimation from RoCoF

It is interesting to see whether the proposed inertia measurement method can be verified by checking whether an observation of RoCoF (Rate of Change of Frequency) gives the same result or not. Consider a system that the synchronous machine used in section 5.1.1

is connected to some loads. At some moment, part of the loads is tripped. According to the swing equation, the system active power change ΔP satisfies

$$2H\frac{d\Delta\omega}{dt} = -\Delta P - D\Delta\omega \tag{5.5}$$

Here, $\frac{d\Delta\omega}{dt}$ is the system RoCoF. The inertia constant H can be calculated by

$$H = \left|\frac{\Delta P + D\Delta\omega}{2\cdot RoCoF}\right| \tag{5.6}$$

Usually, in a synchronous machine, the damping coefficient D is small and $D\Delta\omega \approx 0$, so the synchronous machine inertia constant H can be estimated by

$$H = \left|\frac{\Delta P}{2\cdot RoCoF}\right| \tag{5.7}$$

The proposed inertia measurement method can be verified by equation (5.7), the 100 MVA synchronous machine with inertia constant $H = 3s$ connecting to 100MW resistive loads system is simulated in PSCAD/EMTDC. At 1s, 50MW of the loads are tripped out from the system. In Figure 5-4(c), the active power change in the system is -50MW (-0.5pu in a 100MVA base). In Figure 5-4(b), at 1.4 s, RoCoF is approximately 0.075pu/s. Based on equation (5.7), the measured inertia constant H by RoCoF is around 3.2s, which is close to the actual H of 3.0 s. The probing frequency injection method proposed in section 5.1.1 on the other hand gives a more accurate estimate of $H = 3.0\ s$.

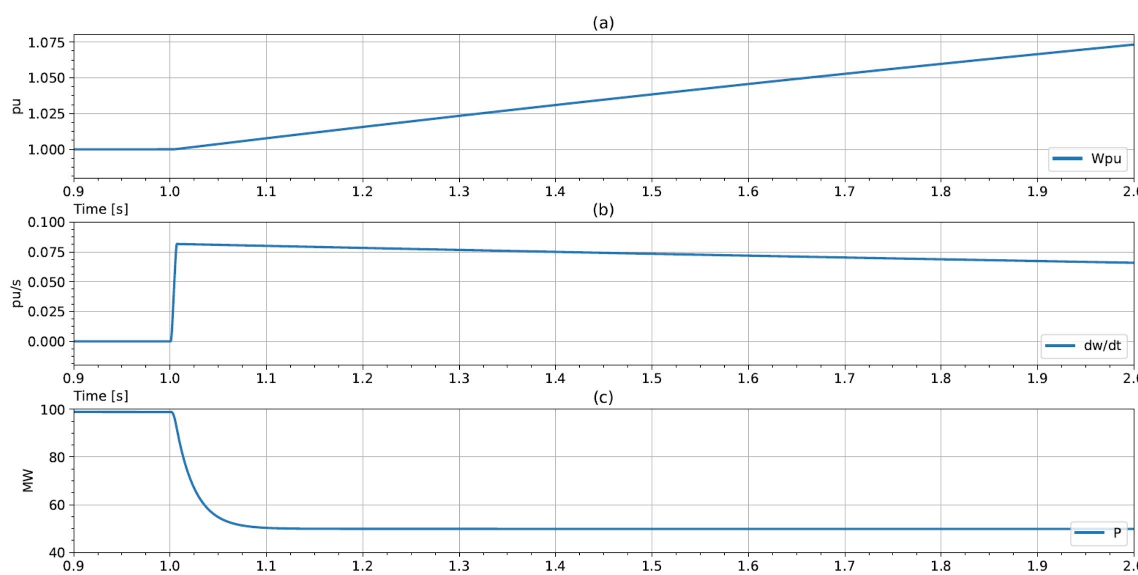

Figure 5-4 (a)System frequency (b) measured RoCoF (c) active power output from Synchronous machine.

5.2 Inertia response of a VSM

In a power electronics converter-dominated power system, the traditional mechanical rotational inertia of generators may not be the sole source of system inertia. The inertia estimation method proposed in section 5.1.1 is further used in this section to see whether a VSM or other type of GFM VSC can offer equivalent inertia in the manner of a synchronous machine. This experimental method may be particularly useful if the GFM VSC control system is "black boxed" so that theoretical calculation of inertia is not possible.

In section 3.2.1, it is shown that the inertia constant and damping coefficient in a VSM can be selected arbitrarily and is not constrained to the physical ranges available to a real machine. The damping coefficient D for a VSM is often selected to be larger than that of a synchronous machine [48] to give improved stability. This fact was explained in Chapter 4, section 4.4.2. For VSM inertia estimation, the impact of large D should be considered in equation (5.3) and (5.6).

5.2.1 VSM inertia measurement by the proposed probing frequency injection method

Assume the dc side voltage of VSM is constant, which is not an unreasonable assumption, as many rectifier/inverter arrangements are controlled in this manner. The VSM test system is the same as that reported in section 3.2 and consists of an ac grid represented by a Thevenin equivalent voltage source behind resistor R_s and inductor X_s as shown in Figure 5-5. The VSM's virtual inertia constant H is set at 0.5 s and damping coefficient D is at 50 pu, other system parameters remain the same as shown in Table 3-1. A probing current or voltage signal can be injected at PCC similar to the experiment on a synchronous machine shown in section 5.1.2. For this test case, a probing current I_h with 5% of rated current magnitude is injected at PCC.

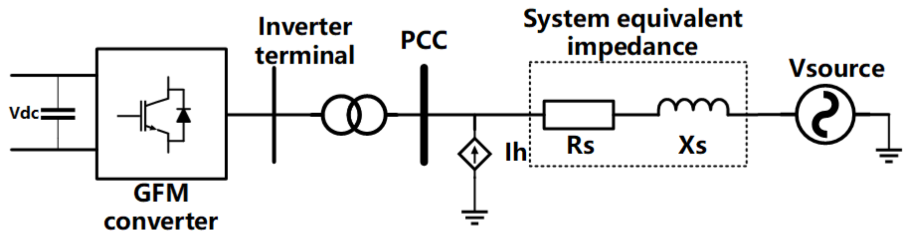

Figure 5-5 GFM converter inertia test case using current signal injection method.

As the damping coefficient D for a VSM may be significantly larger than that of a synchronous machine, the impact of D on the result should be considered when using equation (5.3) for inertia estimation. Figure 5-6 shows the **theoretical** calculation result of $\left|H + \frac{D}{2j\omega}\right|$ for a system with nominal frequency f_0, injection probing frequency $f_h = f_0 - \Delta f$, when Δf changes from 10 Hz to 59 Hz. As can be seen, when $D = 1$, which is close to that of a real synchronous machine, $\left|H + \frac{D}{2j\omega}\right| \approx H$ at any Δf range in the figure. However, when D is large such as $D = 20$ or 50, which may be the case for GFM converter, the larger the D, the larger error between H and its measurement of $\left|H + \frac{D}{2j\omega}\right|$.

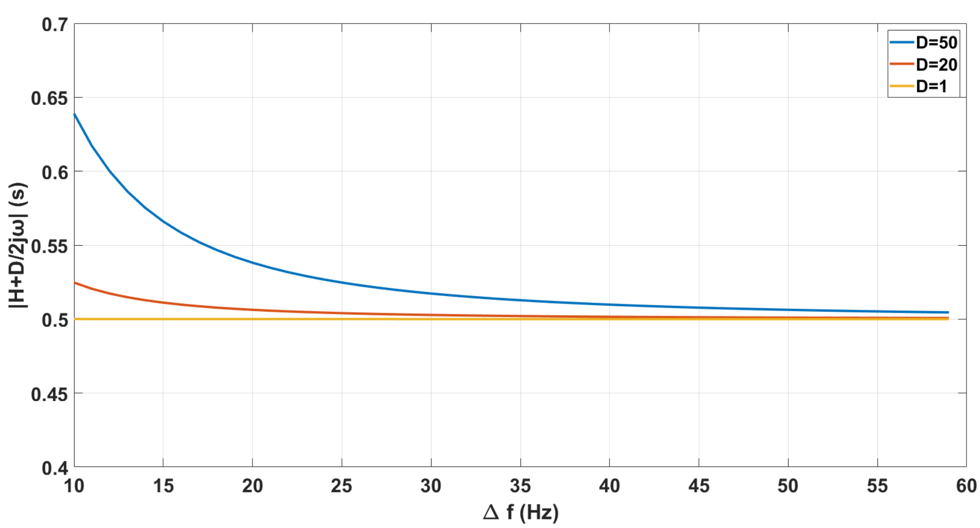

Figure 5-6 theoretical calculation of $\left|H + \frac{D}{2j\omega}\right|$ for VSM

The proposed experimental approach with injected frequency was applied to measure the inertia. Figure 5-7 shows the EMT simulation results for the case of $D = 20$ and $D = 50$. Overlaid on the measurement is the theoretical expectations from Figure 5-6, and the two match up well. In the simulation, the VSM inertia is measured at $\Delta f = 10, 20, 30, 40, 50$

and 59 Hz. From the graphs its is noticed that if the injected frequency can be kept small (i.e., large Δf of 50 Hz or more) the measured virtual inertia constant is much closer to the actual virtual inertia constant of $H = 0.5\ s$.

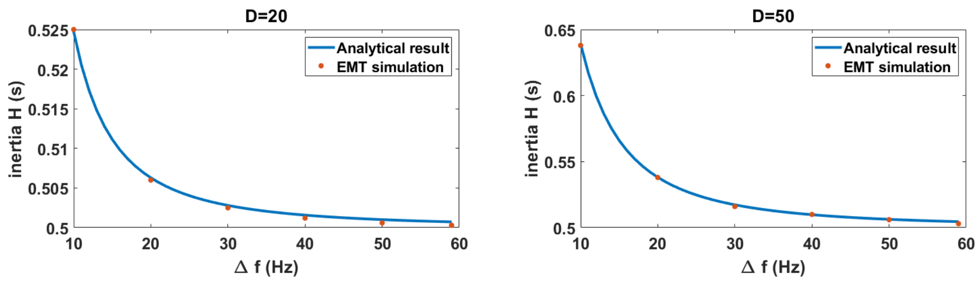

Figure 5-7 comparisons of the inertia measurement by EMT simulation and theoretically calculated $\left|H + \frac{D}{2j\omega}\right|$

The error caused by large D on VSM inertia measurement can also be avoided with a second probing frequency injection on the same VSM at another different Δf. If the inertia measurement is H_{m1} with Δf_1, and the inertia measurement is H_{m2} with Δf_2. Then the actual VSM inertia H can be calculated by

$$\begin{cases} H_{m1}^2 = H^2 - \dfrac{D^2}{4(2\pi\Delta f_1)^2} \\ H_{m2}^2 = H^2 - \dfrac{D^2}{4(2\pi\Delta f_2)^2} \end{cases} \Rightarrow H = \sqrt{\frac{H_{m1}^2\Delta f_1^2 - H_{m2}^2\Delta f_2^2}{\Delta f_1^2 - \Delta f_2^2}} \tag{5.8}$$

Thus, the error of large damping coefficient D on VSM inertia measurement is eliminated. Consider the case with $D = 50$ in Figure 5-7, $\Delta f_1 = 10\ Hz$, $\Delta f_2 = 20\ Hz$, $H_{m1} = 0.638\ s$, $H_{m2} = 0.538\ s$, then according to equation (5.8) the actual VSM inertia H is

$$H = \sqrt{\frac{0.638^2 \cdot 10^2 - 0.538^2 \cdot 20^2}{10^2 - 20^2}} s = 0.5s \tag{5.9}$$

which is the same as the actual virtual inertia set in the controls.

5.2.2 VSM inertia verification by RoCoF

To verify the VSM inertia by RoCoF, the GFM converter studied in section 5.2.1 is connected to some passive loads. The power consumption of Load 1 and 2 are 150 MW and 50 MW. A step change on load is applied in the system shown in Figure 5-8. The converter active power reference is set at 150 MW and initially only Load 1 is connected. Then, Load 2 is connected to the system at 5 s.

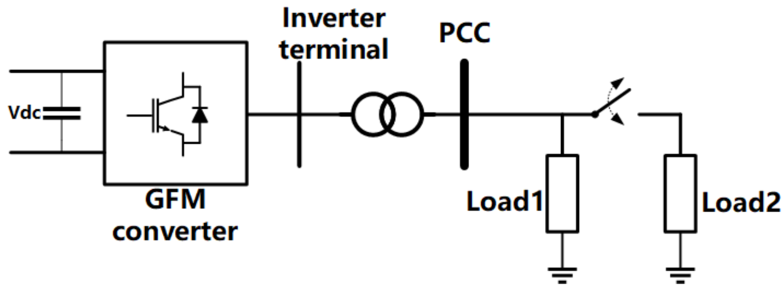

Figure 5-8 VSM inertia test case using RoCoF observation method.

When Load 2 is connected, the total power consumption increases from 150 MW to 200 MW. Since the converter active power reference is set at 150 MW, the power consumption is larger than the available power supply, and so the system frequency will start to drop. Figure 5-9(a) shows the EMT simulation result of transient system frequency change when the load increases. At 5.015s, the change of system frequency $\Delta\omega$ is -0.001 pu. In Figure 5-9 (b) and (c), the system RoCoF $\frac{d\omega}{dt}$ is -0.05 pu/s, and the active power output P from VSM changes from 0.75 pu to 0.85 pu. According to equation (5.6), the inertia constant H of the VSM can be estimated by

$$H = \left|\frac{\Delta P + D\Delta\omega}{2\cdot RoCoF}\right| = \left|\frac{0.85-0.75+50\cdot(-0.001)}{2\cdot(-0.05)}\right| s = 0.5s \tag{5.10}$$

The equivalent inertia of VSM as measured using RoCoF is consistent with the inertia measurement by the proposed probing frequency injection method. This further shows that the proposed method is also applicable when there is no rotating inertia, just the virtual inertia of the VSM. However, due to the large damping coefficient of the VSM, the impact of the damping coefficient D on the inertia measurement has to be considered. Generally, D is a control parameter of the VSM, but if the controller is "black boxed" or if we are measuring the aggregate virtual inertia of a number of VSMs, it may be difficult to know the value of D which will lead to only an approximate estimate of H. It is worth mentioning that the in-line cascaded current control is enabled in this test. This implies that adding current limiting control to VSM does not affect the amount of inertia it offers to the system during normal operation. However, it may be a different situation if a current limit is hit.

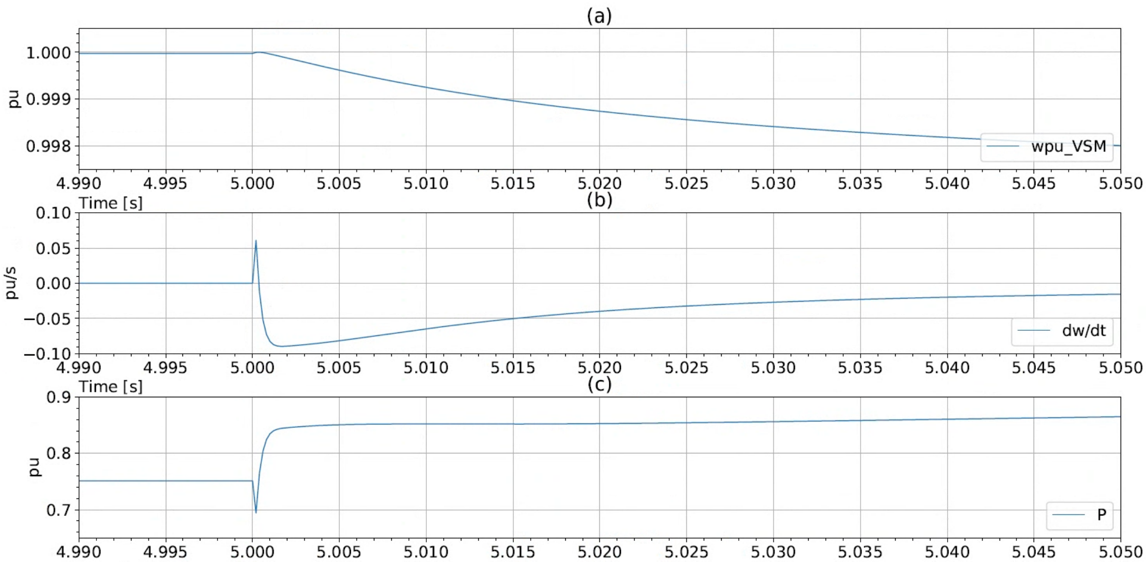

Figure 5-9 VSM test case (a)system frequency (b) RoCoF (c)active power output

5.3 Constructing a low inertia test system to investigate GFL inertia contribution

5.3.1 Aggregated system inertia measurement by RoCoF

To further study the frequency support from GFL and VSM in a low inertia system, a test low inertia system with GFL wind generation IBR, synchronous generator and load is developed in this section. The wind generation IBRs here are type-4 wind farms in GFL control. A GFL offshore type-4 wind turbine uses a VSC-HVdc link to transfer the power. The onshore inverter side controls the dc voltage, and the offshore rectifier side (sending end) controls the sending power.

The test IBR system is shown in Figure 5-10. There are two wind IBRs in the system, the rated power of IBR1 and IBR2 are 50MW and 150MW respectively. The synchronous machine is rated at 200 MVA with inertia constant $H_{sm} = 3\ s$ and a sub-transient reactance of 0.18 pu. Load 1 and Load 2 are purely resistive and consume 300 MW and 100 MW of power respectively.

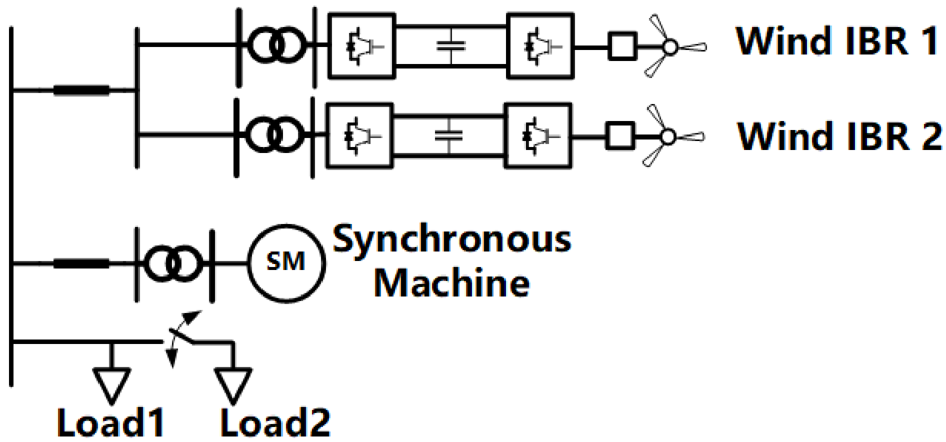

Figure 5-10 The test GFL Wind IBR system

This test IBR system is simulated in PSCAD/EMTDC. Initially, the 300 MW Load 1 is connected and the active power outputs from the synchronous machine and wind IBRs are 100 MW and 200 MW respectively. At $t = 4\ s$, the 100 MW Load 2 is switched on to the system. If a governor is not present nor is there a power-frequency droop ($P\omega$) control on wind IBRs to regulate the power order the system frequency will start to drop due to the load-generation mismatch. Figure 5-11 shows (a) the system frequency and (b) the system RoCoF. The RoCoF is around -0.08 pu at 4.4 s. Note that the RoCoF is as measured by a derivative function and shows some ripple, although looking at the frequency plot, it should be 0 before t=4 s and -0.08 pu after 4.0 s.

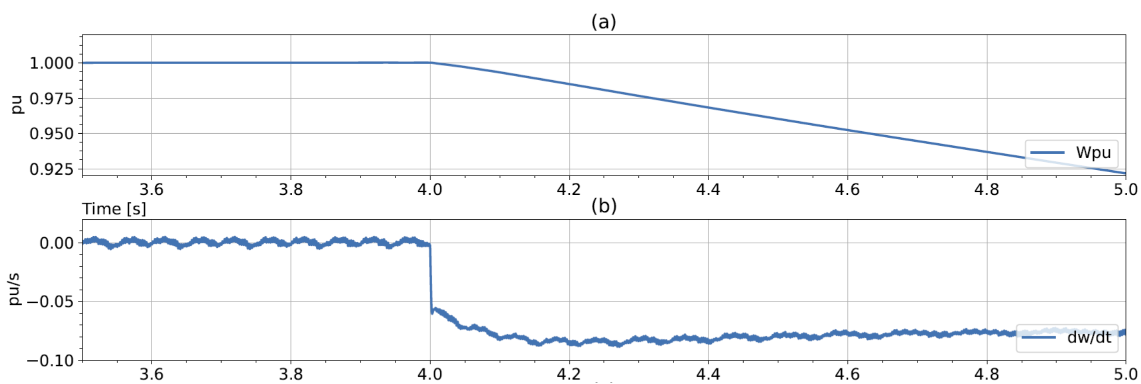

Figure 5-11 test IBR system (a) system frequency (b) measured RoCoF

In the system, the total capacity is 400 MVA and the power change in the system is 100 MW. According to RoCoF observation, the system inertia H_{sys} can be estimated as

$$H_{sys} = \frac{100}{2 \cdot 400 \cdot |-0.08|} s = 1.56 s \tag{5.11}$$

5.3.2 GFL IBRs Inertia contribution

If "n" synchronous machines are present, with individual inertia of $H_1 \cdots H_n$, and MVA ratings of $MVA_1 \cdots MVA_n$, then the total system inertia H_{sys} is:

$$H_{sys} = \frac{MVA_1}{MVA_{total}} H_1 + \frac{MVA_2}{MVA_{total}} H_2 + \ldots + \frac{MVA_n}{MVA_{total}} H_n$$
$$\text{where, } MVA_{total} = \sum_{i=1}^{n} MVA_i \tag{5.12}$$

For a system with aggregated IBRs of virtual inertia H_{IBR} and $MVA = MVA_{IBR}$, and an aggregated synchronous machines of inertia H_{sm} and $MVA = MVA_{sm}$, using equation (5.12), the equivalent inertia of the total system is

$$H_{sys} = \frac{MVA_{sm}}{MVA_{total}} H_{sm} + \frac{MVA_{IBR}}{MVA_{total}} H_{IBR} \tag{5.13}$$

Consider the IBR system shown in Figure 5-10, since the total system MVA_{total} is 400 MVA, the machine MVA_{sm} is 200 MVA and the GFL IBRs MVA_{IBR} is 200 MVA, the GFL IBR inertia constant is calculated as

$$H_{IBR} = \frac{MVA_{total}}{MVA_{IBR}} H_{sys} - \frac{MVA_{sm}}{MVA_{IBR}} H_{sm} = \frac{400}{200} \cdot 1.56 - \frac{200}{200} \cdot 3 = 0.12s \tag{5.14}$$

This shows that the inertia contribution from the GFL controlled IBRs (without $P\omega$ droop) is very limited at 0.12 s, which is very small (only about 7%) in comparison to the total inertia of 1.56 s. This shows that the grid following converter does not make any significant contribution to the system inertia.

5.3.3 Aggregated GFL IBR system inertia measurement by probing frequency injection

Next, the equivalent inertia is measured with the proposed probing frequency injection method. A current probing signal I_h with frequency ω_h is injected at the bus shown in Figure 5-12 which generates frequency content of $\omega_0 - \omega_h$ in speed and power, where ω_0 is the fundamental frequency. The system power response $\Delta P(\omega_0 - \omega_h)$ measured from the power flow going to Load 1 (as it is the only load, its power must be equal to the total supply). Since there is only one synchronous machine as the only source of inertia in this system, the equivalent system frequency $\Delta\Omega = (\omega_0 - \omega_h)$ can be measured from the synchronous machine speed. The impact of the damping coefficient of the synchronous machine on the inertia measurement is small and thus is neglected. So, if the total MVA rating of the system is S_{MVA}, the equivalent system inertia is

$$H_{sys} = \left| \frac{\Delta P(\omega_0 - \omega_h)}{2(\omega_0 - \omega_h)\Delta\Omega(\omega_0 - \omega_h)S_{MVA}} \right| \tag{5.15}$$

Note that in equation (5.15), $\Delta P(\omega_0 - \omega_h)$ is in MW, $\Delta\Omega(\omega_0 - \omega_h)$ is in pu, $\omega_0 - \omega_h$ is in rad/s. Figure 5-13 shows the simulation measurement result with a 10 Hz, 0.05A current probing signal starting at 4.5 s. It takes around 1 s to settle to the final reading of the measured inertia constant of 1.5 s. This is consistent with the result from RoCoF observation.

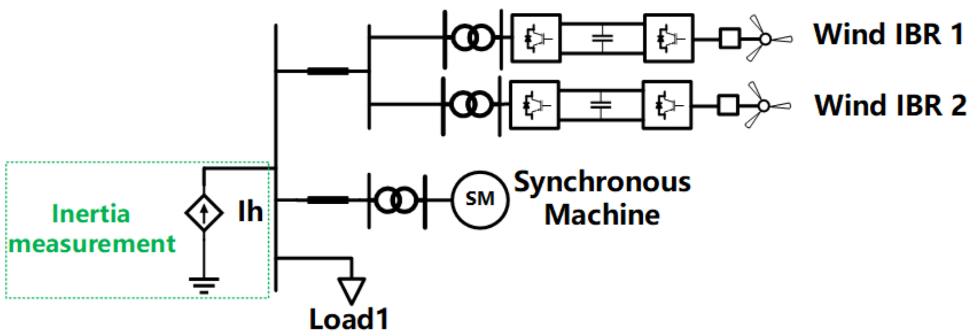

Figure 5-12 Inertia measurement on test system using probing frequency injection

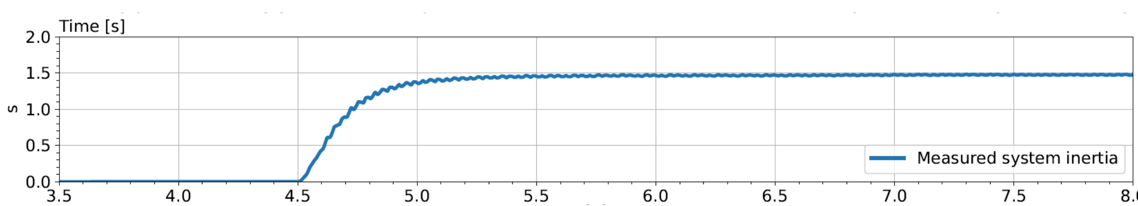

Figure 5-13 Measured synchronous machine inertia by probing frequency injection.

In general, systems with less than 3-4 seconds of equivalent system inertia are considered to have low inertia and may be more susceptible to frequency disturbances [91][92][93]. So, the test system developed in this section is considered as a low inertia system. This test system will be further used for studying the frequency support from the GFM converter in the next section.

5.4 Comparison of frequency support from VSM and GFL VSC in the test low inertia system

In this section, the low inertia system developed in section 5.3 is connected to (1) a VSM and (2) a GFL VSC to study their respective frequency support performances in such low inertia IBR system. As the comparison is on the inertia contribution, and not a primary or secondary response, the governor of the synchronous machine is disabled in this study.

Figure 5-14 shows the system configuration. The low inertia test system is connected to a GFL or VSM MMC-HVdc link as the case may be. The MMC-HVdc system parameters are the same as shown in Table 2-2, Section 2.2.3. The local converter terminal is operated as an inverter and can be regarded as being connected to a constant dc voltage V_{dc} which is controlled by a remote converter. The HVdc converter is rated at 1000MVA, and the active power order is set at 500MW. In this example, Load 1 and Load 2 consume 800 MW and 100 MW respectively. The wind IBRs and synchronous machine settings remain the same as in section 5.3.

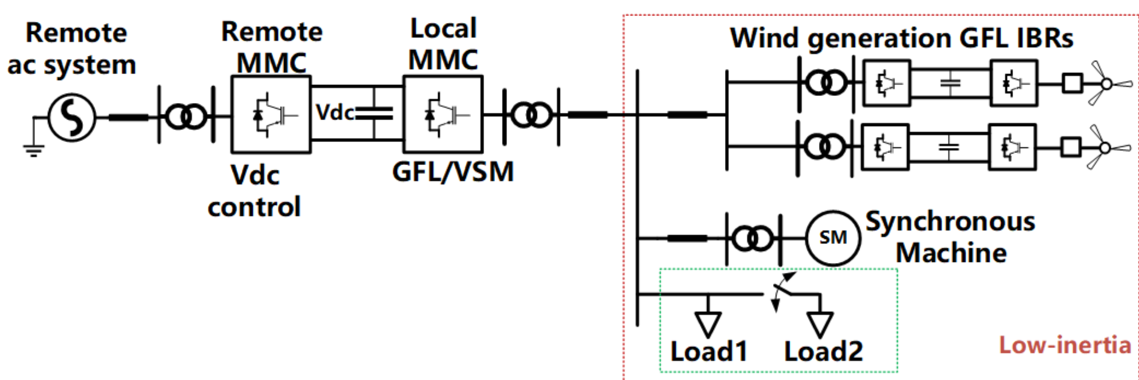

(a)

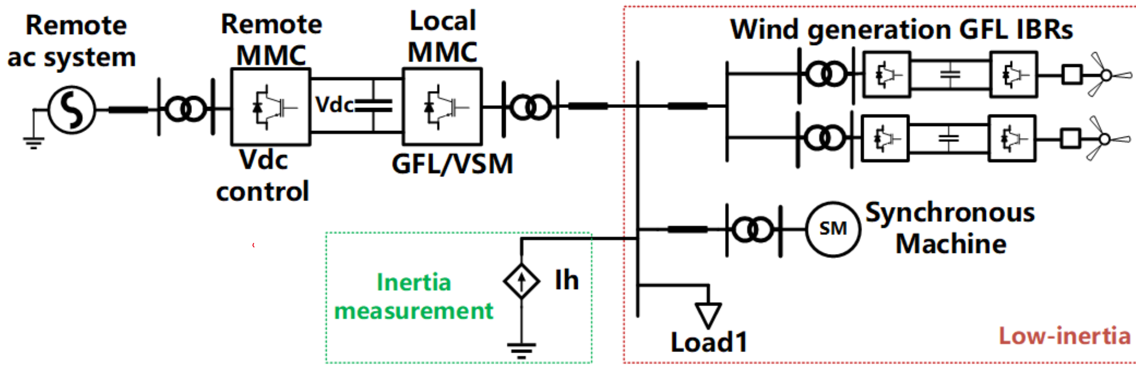

(b)

Figure 5-14 The low inertia IBR test system connected to a GFL or VSM MMC-HVdc (a)Inertia measured by ROCOF (b)Inertia measured by probing frequency injection.

Scenario 1	GFL MMC without $P\omega$ droop
Scenario 2	GFL MMC with $P\omega$ droop
Scenario 3	VSM MMC without $P\omega$ droop
Scenario 4	VSM MMC with $P\omega$ droop

Table 5-1 GFL and VSM frequency support study scenarios

In the simulation, Load 2 will be connected to the system at 4 s and the system power demand is larger than the power supply as shown in Figure 5-14 (a). This will cause a frequency drop and the system inertia is measured by ROCOF measurement. Later, as shown in Figure 5-14 (b), the system inertia is measured by the proposed probing frequency injection method in the steady state without applying generation-load mismatch frequency events. Depending on the different control strategies on the MMC, four scenarios are studied as shown in Table 5-1. In Scenarios 1 and 2, the local MMC is controlled in GFL. As in Scenarios 3 and 4, the local MMC is controlled in VSM. The impact of adding a power-frequency $P\omega$ droop on the power order is also considered for GFL and VSM in Scenarios 2 and 4.

5.4.1 GFL frequency support

In Scenario 1, the MMC is controlled in GFL mode without $P\omega$ droop. As was shown in Section 5.3.1, there is no inertia support from the GFL MMC. The synchronous machine has an inertia of $H_{sm} = 3\ s$. According to (5.13), compared with the system in Section 5.3 without MMC, the total system inertia in the system with GFL MMC will drop to

$$H_{sys\_GFL} = \frac{MVA_{sm}}{MVA_{total}} H_{sm} = 3 \cdot \frac{200}{400+1000} s = 0.43s \tag{5.16}$$

This can be verified by the RoCoF and power change ΔP in the system shown in Figure 5-15. In Figure 5-15, (a) is the system frequency, (b) is RoCoF, (c) is the active power output from the MMC and (d) is the active power output from the synchronous machine. Note that, to minimize ripple and noise interference, a filter with time constant $T_f = 0.01\ s$ had to be included in the derivative operator required to calculate RoCoF. Ideally, the RoCoF should show a step change at t = 4 s, but the filter delay smooths out this response. At 4.2s, the system inertia calculated by RoCoF is

$$H'_{sys\_GFL} = \left| \frac{\Delta P}{2 \cdot RoCoF} \right| = \left| \frac{100/1400}{2 \cdot (-0.08)} \right| = 0.45s \tag{5.17}$$

Since in Scenario 1, there is no $P\omega$ droop for GFL to regulate its power order when the frequency drops, the system frequency keeps dropping and eventually the system becomes unstable at around 6.3 s as in Figure 5-15.

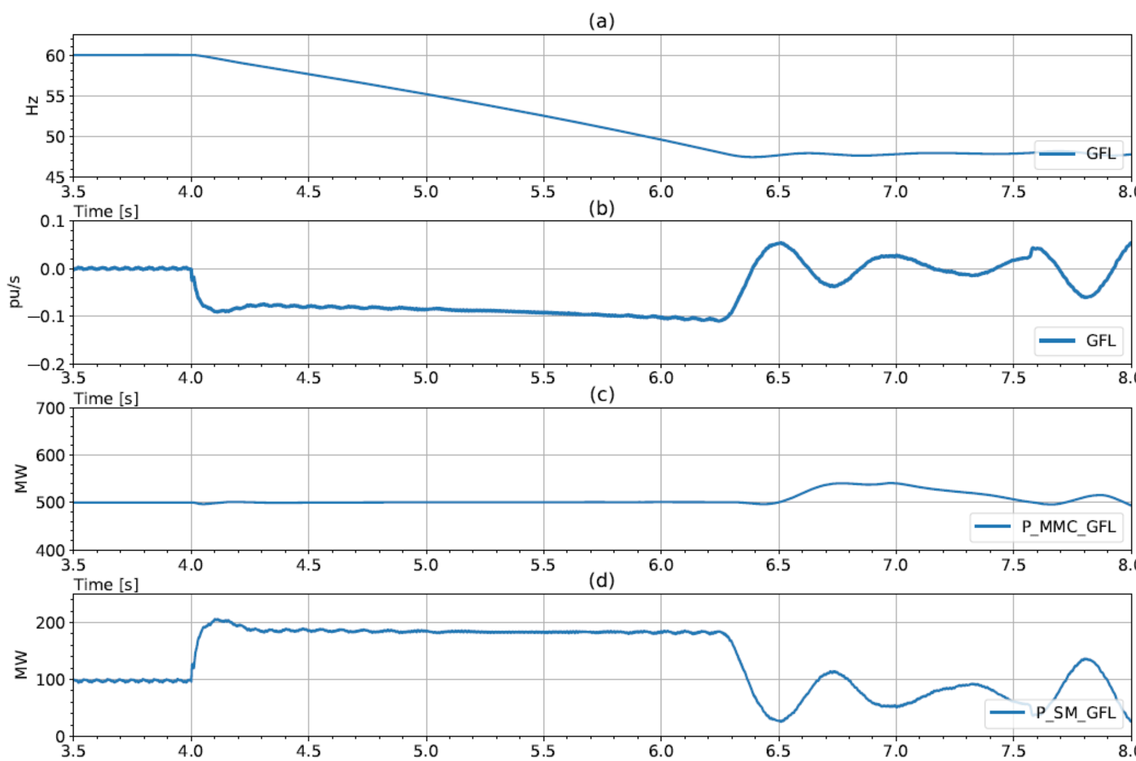

Figure 5-15 Scenario 1 (a) system frequency (b) RoCoF (c) active Power output from MMC (d) active power output from SM

On the other hand, in Scenario 2, the GFL MMC has a $P\omega$ droop shown in Figure 5-16. It follows the active power – frequency requirements in IEEE Standard 2800-2022 [27]. The standard advocates dividing the active power-frequency droop control into a primary frequency response (PFR) characteristic and a fast frequency response (FFR) characteristic marked in yellow and green in Figure 5-16. The PFR's dead band db_{PFR} is $\pm 0.1Hz$, and the droop gain is $D_{PFR} = 0.033\ pu/Hz$. If there is a frequency drop in the system, the active power output ΔP_{PFR} in pu from PFR is

$$\Delta P_{PFR} = D_{PFR}(f_{ref} - f_{measure} - db_{PFR}) \tag{5.18}$$

For FFR, the dead band db_{FFR} is $\pm 0.5Hz$, the droop gain $D_{FFR} = 0.167\ pu/Hz$.

$$\Delta P_{FFR} = D_{FFR}(f_{ref} - f_{measure} - db_{FFR}) \tag{5.19}$$

The PFR and FFR are independent of each other but complement together to regulate the power output from the MMC during the frequency change events. If the maximum allowed active power output from MMC is P_{avl}, the power order P'_{ref} for MMC with $P\omega$ droop is

$$P'_{ref} = \min\left\{P_{avl}, P_{ref} + \Delta P_{PFR} + \Delta P_{FFR}\right\} \tag{5.20}$$

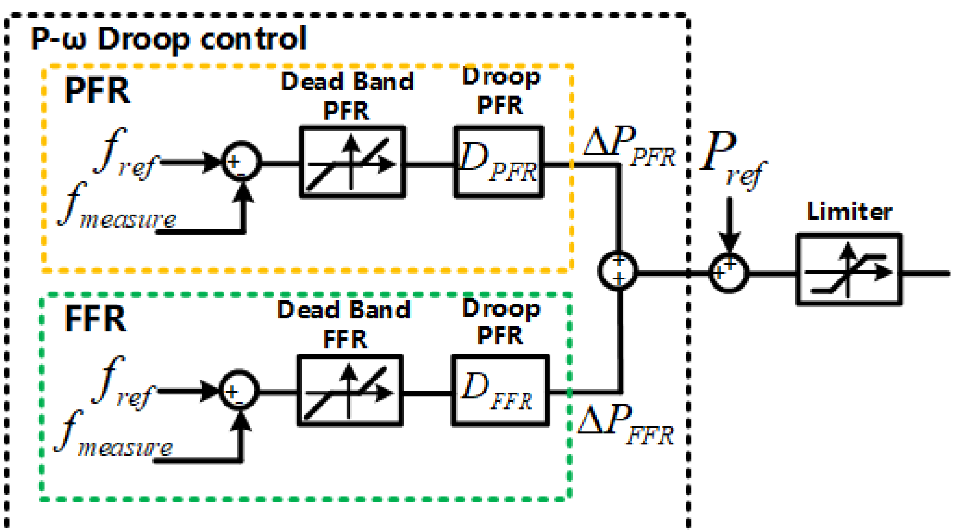

Figure 5-16 the active power – frequency droop control

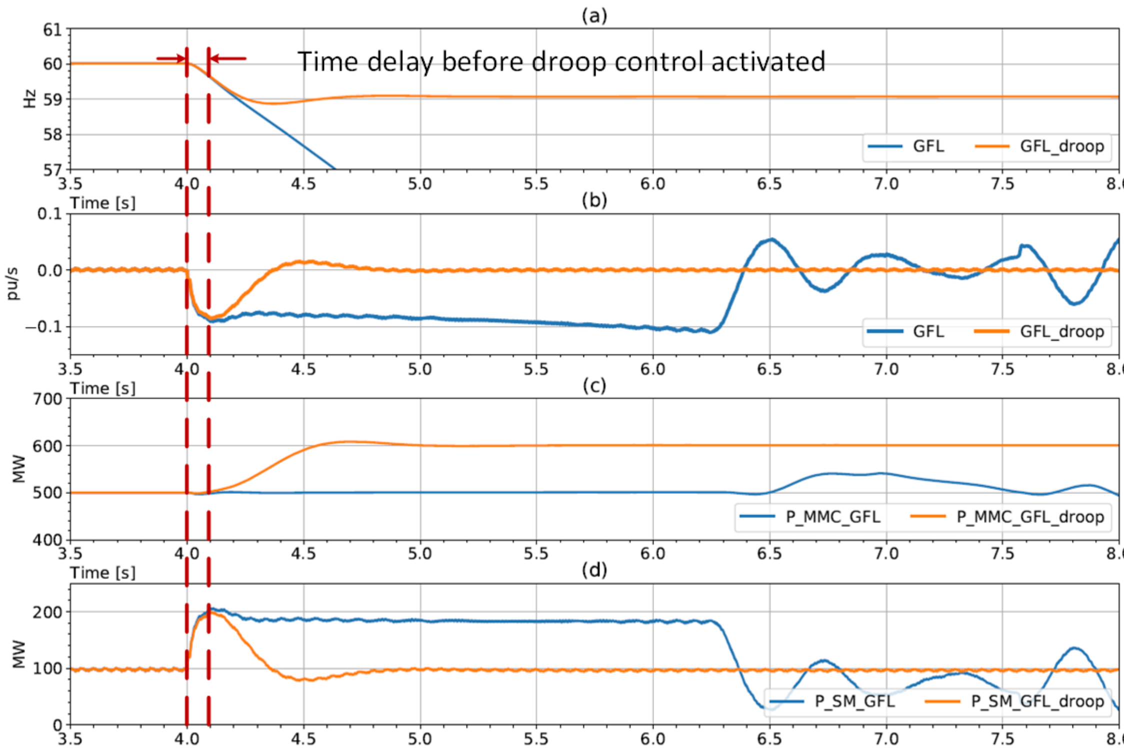

Figure 5-17 Scenario 2 (orange curve) (a) system frequency (b) RoCoF (c) active Power output from MMC (d) active power output from SM

Figure 5-17 shows the comparison between the cases without $P\omega$ droop (Scenario 1 -blue) and with $P\omega$ droop (Scenario 2- orange). The 100 MW Load 2 is switched on to the system at 4 s. As a result, the system frequency begins to drop, identical to the situation for scenario 1 discussed earlier. However, turning on the droop characteristic at 4.05 s makes the MMC output extra power and prevent the system frequency from dropping below 59.1 Hz as can be seen in Figure 5-17 (a) and (c). This conveys that although adding $P\omega$ droop does not per-se add inertia to the system, it nevertheless prevents the frequency from running down completely by re-establishing the generation-load balance, albeit at a different frequency.

It is worth noting that due to the fast transient and activation of power-frequency droop control, it is challenging to accurately measure the system inertia by RoCoF observation for Scenario 2. This is similar to the case of a rotating machine, where adding a $P\omega$ droop to the governor transfer function can reduce the RoCoF but is not actually increasing the rotational inertia.

Note that the proposed probing frequency injection method measures the system inertia during the steady state, and thus the $P\omega$ droop does not activate and make an impact on the inertia measurement. This greatly improves the convenience and accuracy of the inertia measurement in such IBR systems.

Similar to the case discussed in section 5.3, here the power response to the injection signal is obtained from the power going to Load 1, while the equivalent system frequency measurement is obtained from the synchronous machine's rotating speed. Figure 5-18 shows the system inertia measurement result for Scenarios 1 and 2. The injected measurement signal has 5% of the rated current magnitude at 10 Hz and starts to inject into the system at 4.5 s. The measured inertia result is 0.43 s which is exactly the value in (5.16).

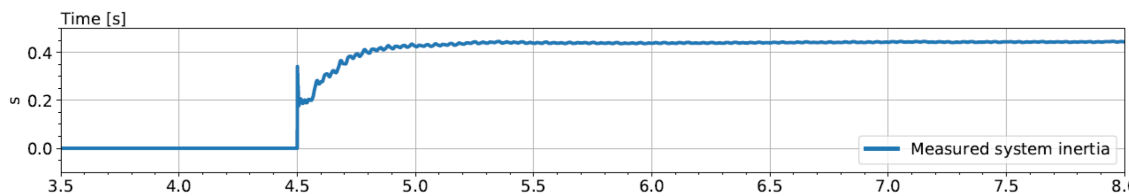

Figure 5-18 system inertia measurement for Scenarios 1 and 2 with the proposed probing frequency injection method

5.4.2 VSM frequency support

In Section 5.4.1, the frequency support from the GFL MMC to the IBR system was discussed. In this section, the performance of the frequency support with the MMC controlled as a VSM will be investigated.

5.4.2.1 RoCoF observation for the system with VSM

The VSM inertia constant H_{VSM} is 2 s and the damping coefficient D is 50 pu. According to (5.13), the calculated total system inertia H_{sys_GFM} is

$$H_{sys\_GFM} = \frac{MVA_{sm}}{MVA_{total}} H_{sm} + \frac{MVA_{VSM}}{MVA_{total}} H_{VSM} = 3 \cdot \frac{200}{1400} + 2 \cdot \frac{1000}{1400} s = 1.86s \quad (5.21)$$

To check the system inertia by RoCoF observation, loads in Figure 5-14 (a) are stepped up from 800 MW to 900 MW at $t = 4\,s$. Figure 5-19 shows EMT simulation results for Scenario 3 (VSM without $P\omega$ droop control, green) and Scenario 4 (VSM with $P\omega$ droop control, Red). Note that, for Scenario 4, the added $P\omega$ droop has same parameters as with the GFL in Scenario 2.

For the case without droop (i.e., Scenario 3), at $t = 6\ s$, the measured RoCoF is around -0.01 pu/s in Figure 5-19 (b), the active power change from the MMC is $\Delta P_{MMC} = 90MW$ in Figure 5-19(c) and from the synchronous machine is $\Delta P_{SM} = 8MW$ in Figure 5-19(d). Since the damping Coefficient D in VSM is very large, this impact cannot be neglected for the inertia estimation. In VSM, $D\Delta\omega \approx 0.05\ pu$ at 6 s. According to (5.6), the total system inertia measured by RoCoF is

$$H'_{sys\_GFM} = \left| \frac{\Delta P_{SM} + (\Delta P_{VSM} + D\Delta\omega)}{2 \cdot RoCoF} \right| = \left| \frac{8 + (90 - 0.05 \cdot 1000)}{2 \cdot (-0.01) \cdot 1400} \right| = 1.71s \tag{5.22}$$

This is within 8% of the inertia value in (5.21). However, if $D\Delta\omega$ in VSM is not considered, the measurement result is 3.5 s, which gives 88% error! In Section 5.5, it will be demonstrated that the probing frequency injection method offers higher accuracy in measuring inertia and does not necessitate knowledge of $D\Delta\omega$ in VSM.

Compared with the system inertia of the GFL MMC, which is only 0.43 s as shown in Section 5.4.1, the system inertia with the VSM MMC is significantly increased. This demonstrates the superior frequency support provided by VSM control.

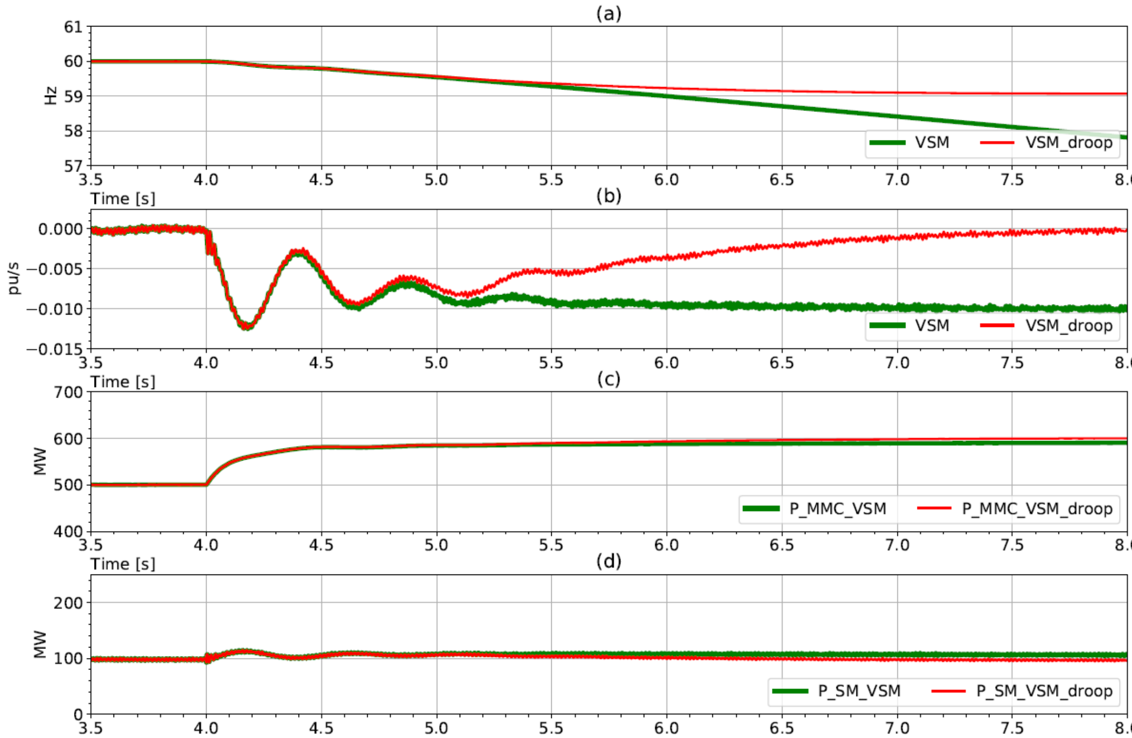

Figure 5-19 Scenario 3 (green) and 4 (red) (a) system frequency (b) RoCoF (c) active Power output from MMC (d) active power output from SM

Figure 5-20 compares the simulation results of the four scenarios. The system RoCoF with VSM scenarios (Scenario 3: without droop, green; Scenario 4: with droop, red) are much smaller than the scenarios with GFL (Scenario 1: without droop, blue; Scenario 2: with droop, orange) shown in Figure 5-20 (b). The active power output of the VSM changes instantly after the system power mismatch occurs, which is faster than the active power output change of GFL with frequency droop shown in Figure 5-20 (c). The superior frequency support performance of VSM is also reflected in the synchronous machine active power output shown in Figure 5-20 (d). The transient active power output from the synchronous machine is much less in VSM scenarios compared with GFL scenarios, which conveys that the IBR system with VSM relies less on synchronous machines to maintain stable. Table 5-2 summarizes the frequency support performance for the 4 scenarios in terms of the inherent inertia response and the capability to stabilize system frequency with auxiliary droop control.

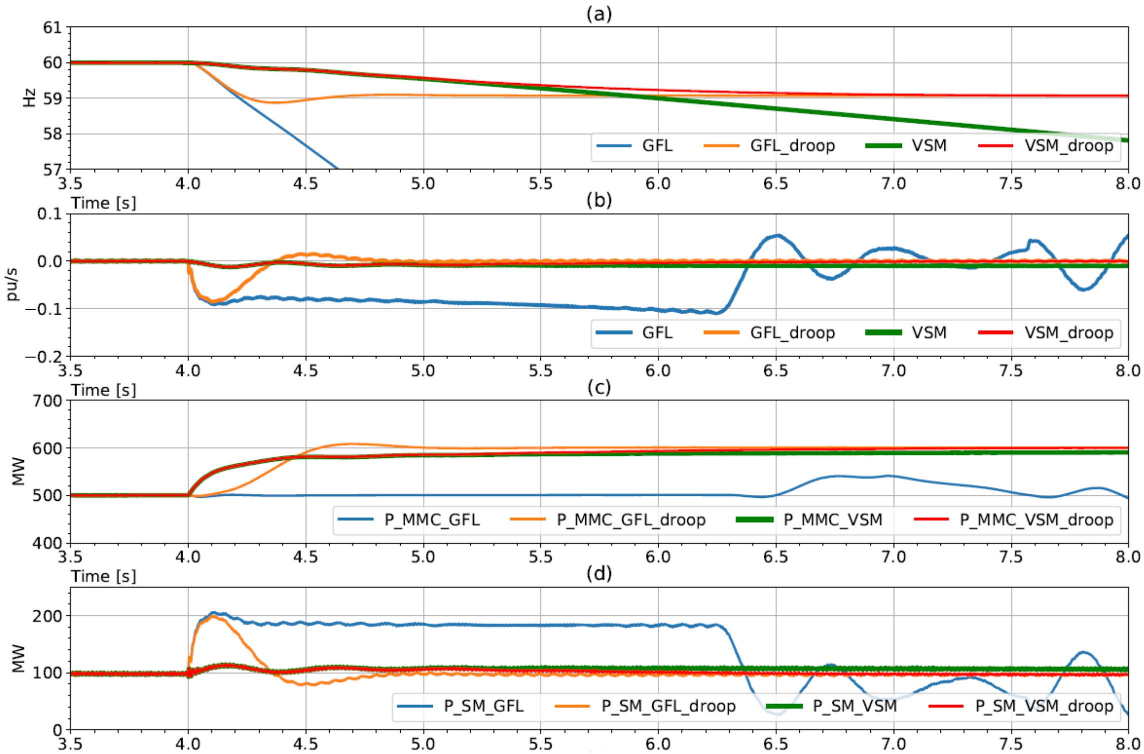

Figure 5-20 Comparison of the 4 scenarios

Control type	Inherent Inertia response	Frequency stabilization with droop
GFL	Negligible (Scenario 1)	Is Possible (Scenario 2)
VSM	Similar to actual synchronous machines (Scenario 3)	Is Possible (Scenario 4)

Table 5-2 Comparison of frequency support performance of GFL and VSM

5.5 Probing frequency injection inertia measurement for the system with multiple SMs and/or VSMs

This section investigates how the composite inertia of an IBR system with actual and virtual synchronous machines can be estimated.

5.5.1 Individual inertia measurements of each device (SM or VSM) in a network

Consider the system in Figure 5-14 (b) which has one synchronous machine and the local HVdc inverter is controlled as a VSM. The wind harvesting converters operate as GFLs and so are not part of the inertia contribution. In this section, we show how the inertia of each option (SM or VSM) can be individually determined. In the following section, we will show how the individual measurements can be combined to give the aggregate inertia of the system.

In the previous section, the IBR system inertia with VSM is measured by RoCoF. However, according to (5.22), the inertia estimation requires one to know the value of $D\Delta\omega$ in the VSM controller, which may be unavailable, especially when the control systems are "black boxed". This renders the RoCoF inertia measurement to be inaccurate. As was mentioned in Section 5.4.1, the probing frequency injection method is better at measuring inertia. This is because, although the accuracy of the probing frequency injection measurement of VSM inertia is affected by a large damping coefficient D, the measured result is nevertheless close to the actual value if the injected frequency is kept small (i.e., 10 Hz or less) as was shown in Section 5.2.1.

To demonstrate the proposed probing frequency injection method for this case, a current probing signal equal to 5% of the system rated current magnitude at 10Hz is injected at the Load 1 bus at $t = 4.5\ s$. Power changes $\Delta P_{sm}(\omega)$ for the synchronous machine and $\Delta P_{vsm}(\omega)$ for the VSM are measured. Speed change $\Delta\Omega_{sm}(\omega)$ for the SM is obtained from the shaft speed measurement and the virtual speed change $\Delta\Omega_{vsm}(\omega)$ for the VSM virtual speed change is obtained from the VSM controller. Figure 5-21 shows that the inertia measurement for the synchronous machine is $H_{sm} = 3\ s$ and for VSM is $H_{vsm} = 2\ s$, which is consistent with the actual value.

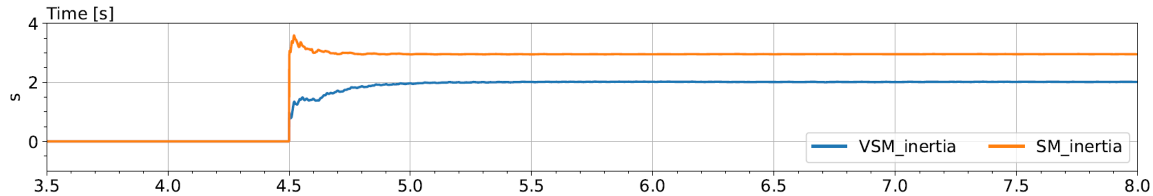

Figure 5-21 Measured individual SM and VSM

The inertia of a synchronous machine is an intrinsic physical property determined by its rotating mass and cannot be changed once the machine is connected to the power system. However, the VSM has the ability of dynamically adjusting its virtual inertia during operation, allowing more control flexibility. It is interesting to check whether the proposed probing frequency injection-based inertia measurement can be used to check the change in apparent inertia. For the above case, at $t = 6\,s$, if the virtual inertia constant of VSM changes from 2 s to 3 s, Figure 5-22 shows the measured inertia for VSM, the measurement tracks VSM's inertia well. There is about 1 s settling time for the final reading to stabilize.

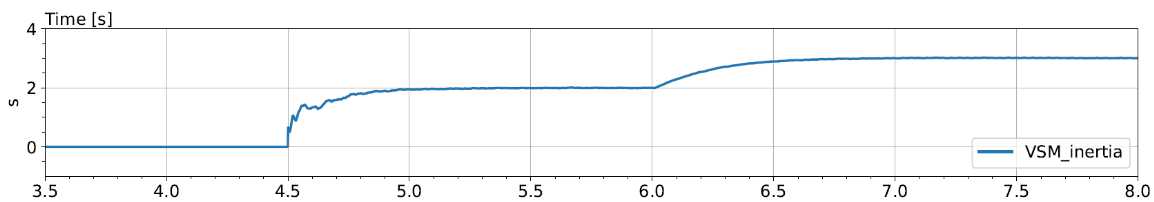

Figure 5-22 measured VSM inertia when it changes

5.5.2 Aggregated system inertia calculation with SMs and/or VSMs

The aggregate inertia H_{sys} of the entire system of SMs and/or VSMs can be determined once the individual inertia of the SMs or VSMs is measured using the approach of the previous section. First consider the system in the previous example shown in Figure 5-14 (b) in which the synchronous machine has an MVA rating of MVA_{sm} and inertia constant of H_{sm}, and the VSM has MVA rating of MVA_{vsm} and inertia constant of H_{vsm}. Then in the manner (5.13), the aggregated inertia of the composite system is calculated below:

$$H_{sys} = \frac{MVA_{sm}}{MVA_{total}} H_{sm} + \frac{MVA_{vsm}}{MVA_{total}} H_{vsm} \tag{5.23}$$

where, $MVA_{total} = MVA_{sm} + MVA_{vsm}$

Equation (5.23) can be extended to a system with n_{sm} synchronous machines and/or n_{vsm} VSMs:

$$H_{sys} = \frac{\sum_{i=1}^{n_{sm}} MVA_{sm_i} H_{sm_i} + \sum_{j=1}^{n_{vsm}} MVA_{vsm_j} H_{vsm_j}}{MVA_{total}} \tag{5.24}$$

where, $MVA_{total} = \sum_{i=1}^{n_{sm}} MVA_{sm_i} + \sum_{j=1}^{n_{vsm}} MVA_{vsm_j}$

Figure 5-23 shows the calculated aggregate system inertia based on the individual inertia measurement results from Section 5.5.2. Initially, the system inertia is 1.86 s, then at $t = 6$ s, the apparent inertia of the VSM is ordered to change from 2 s to 3s, which dynamically increases the total system inertia from 1.86 s to 2.57 s.

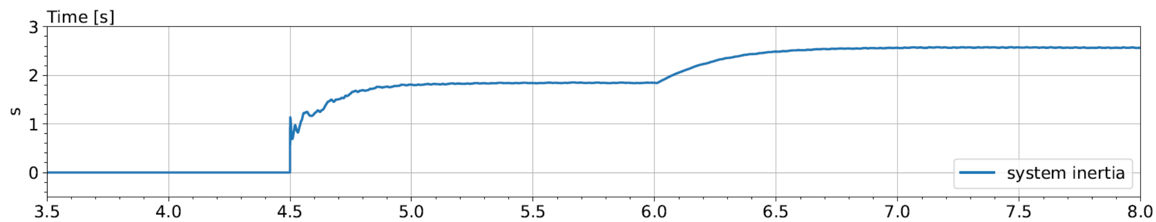

Figure 5-23 Calculated aggregated system inertia

5.6 Summary

This chapter proposes a new inertia measurement method for IBR systems based on probing frequency injection. The proposed method is first validated on a single synchronous machine and then on a VSM. It shows accurate measurement results for the synchronous machine case. However, for VSMs, which can have large virtual damping coefficients, the measurement can have errors. Nevertheless, this error can be made negligibly small if the frequency of the injected component is kept small (10Hz or less). Alternatively, it can be entirely eliminated by conducting two injected probing signals at different frequencies. The probing frequency injection method can conveniently measure the system inertia without the application of the generation-load mismatch frequency events and give more accurate results compared with RoCoF observation.

The frequency support provided by an HVdc inverter was measured with the inverter controlled as a GFL and then as a VSM. The system inertia was measured by both RoCoF and probing frequency injection methods. It was determined that the GFL does not contribute significant inertia to the system, which is to be expected because the inverter is controlled in constant power mode. On the other hand, by emulating an actual synchronous machine, the VSM can provide significant inertia to the system and greatly improve system ride through capability to frequency variation events.

Chapter 6

Conclusions and Future Work

This chapter presents concluding remarks for this Ph.D. thesis and discusses future work.

6.1 Conclusions

The main contributions of this thesis are:

- The dynamic performance of the VSM developed in this thesis is compared with that of a synchronous machine and a GFL VSC. It is shown that the VSM can behave similarly to a synchronous machine. Moreover, the VSM can select a wider range of inertia constants and damping coefficients than the actual synchronous machine and achieve better control dynamic behavior. When compared with the GFL, the VSM shows better performance in maintaining stable operation when connected to a weak AC system. However, when connected to a stronger AC system, the GFL converter can maintain stable operation with a good dynamic response, while the VSM may exhibit a slower response following a phase angle jump in comparison to a GFL converter.

- The current limiting performance of two VSM current limiting methods, namely switchable current limiting and in-line cascaded current limiting, is compared using EMT simulation. The in-line cascaded current limit is permanently active, whereas the switchable current limiting loop is only switched on when an overcurrent is detected. The switchable current limiting method fails to limit the overcurrent during the immediate moments after fault inception due to the control mode switch needing a short period to react when a fault is detected. However, for in-line cascaded current limiting, since the current limiting loop is always in-line for normal as well as faulted operation, it does not require very fast fault detection and control mode switching, and thus the overcurrent is well limited over the entire fault transient.

- Using EMT simulation, it was shown that the disturbance ride-through performance of the VSM with either switchable or in-line cascaded current limiting control can be significantly optimized by transiently changing the active power order and the damping coefficient in its power synchronization loop. This greatly improves the VSM converter's post-fault recovery, particularly when connected to strong AC systems, which was seen as a challenge for more classical GFM control methods. Additionally, the performance with weak AC systems was also improved.

- The linearized models of VSM with and without in-line cascaded current control connected to a Thevenin equivalent ac voltage source are developed to investigate the VSM control stability margin under various ac system strength. They show that the VSM is more stable for the weak system when the in-line cascaded current limiting feature is added; and can experience unstable operation with a stronger system strength. One could envisage an adaptive controller where the parameters change with network conditions. However, detecting a network change in sufficient time and changing gains dynamically, could prove to be a problem. Thankfully a more robust solution is possible, because a single suitable gain parameter set can be found to allow stable operation when connected to weak as well as strong ac systems.

- A wider range of inertia constants and damping coefficients can be selected for the VSM than are present in an actual synchronous machine. An important discovery from eigenvalue analysis is that the damping coefficient of the VSM controller should be larger than that of an actual synchronous machine to avoid instability However, eigenvalue analysis shows that the stability of the VSM becomes poorer with a large inertia constant. Thus, the inertia constant for the VSM should not be excessively large for inertia contribution purposes.

- A new method to measure the inertia of the IBR system based on probing frequency injection is proposed. The effectiveness of this method is examined using Electromagnetic Transient (EMT) simulation on a VSM model. However, the method produces inaccurate results when applied straightforwardly with a high damping coefficient of VSM. Nonetheless, this error can be minimized and overlooked by keeping the injected frequency component small (10 Hz or less) or eliminated by conducting two injected probing signals at different frequencies.

- It is shown that GFL IBRs do not contribute significant inertia directly to the system, although they can still support frequency if an active power–frequency droop is included, just in the manner of a frequency droop added to the governor of a real synchronous machine. On the other hand, VSMs do add virtual inertia to the system and directly limit the rate of change of frequency (RoCoF).

- In contrast to the RoCoF observation method, the proposed probing frequency injection method provides a more accurate and convenient way to measure inertia, especially for IBR systems. The RoCoF method can be influenced by the fast transient and activation of power-frequency droop control in IBRs, resulting in inaccurate measurements of system inertia. Additionally, the RoCoF method requires a small or known a-priori damping coefficient, which is derived from knowledge of the VSM's control system. A large damping coefficient can introduce significant measurement errors if not taken into consideration. In contrast, the proposed probing frequency injection method can measure system inertia without applying a load-generation imbalance, i.e., it can be applied with the SM or VSM operating in the steady-state.

6.2 Future Work

Further investigations are summarized below:

- In this thesis, the VSC or IBR is assumed to have a constant dc voltage bus. This is true if the HVdc remote converter is connected to a strong ac system and operates in GFL dc voltage control. However, it is possible that the remote converter could be connected to a very weak network. The analysis of such networks could be undertaken in the future.

- The improvement of VSM disturbance ride through performance is achieved by dynamically changing the control parameters in this thesis. Other solutions to improve VSM disturbance ride through may be possible and requires further study.

- The proposed probing frequency injection method in the thesis requires a precise measurement of synchronous speed or GFM virtual synchronous speed deviation $\Delta\Omega$ at the injected probing signal frequency, which can be challenging to obtain in the field test. A measurement method to capture $\Delta\Omega$ for the field test requires further development.

References

[1] L.Unruh, A. Kariyawasam, S. Dadallage, A. Isaacs, Hawaii Electric Company Stage 2 System Impact Study "Hawaiian Electric Island-Wide PSCAD Studies", Electranix Corporation, 2021.

[2] J. Matevosyan, B. Badrzadeh, et.al, "Grid-Forming Inverters". IEEE Power & energy, Volume 17, Number 6, pp.89-98, 2019.

[3] Energy Systems Integration Group (ESIG) report, "Grid-Forming Technology in Energy Systems Integration", ESIG, 2022

[4] J. Matevosyan, J. MacDowell, et.al, "A Future with Inverter-Based Resources". IEEE Power & energy, Volume 19, Number 6, pp.18-28, 2022.

[5] NERC Inverter-Based Resource Performance Working Group (IRPWG) report, "Grid Forming Technology: Bulk Power System Reliability Consideration". NERC, Dec. 2021.

[6] Lin, Yashen, Joseph H. Eto, Brian B. Johnson, Jack D. Flicker, Robert H. Lasseter, Hugo N. Villegas Pico, Gab-Su Seo, Brian J. Pierre, and Abraham Ellis. 2020. esearch Roadmap on Grid-Forming Inverters. Golden, CO: National Renewable nergy aboratory. REL/TP-5D00-73476.

[7] Zhou, J. Z., Ding, H., Fan, S., Zhang, Y., & Gole, A. M. (2014). Impact of short circuit ratio and phase locked loop parameters on the small signal behaviour of a VSC HVDC converter. IEEE Transactions on Power Delivery, 29(5), 2287–2296.

[8] "VSC transmission", Cigre Working Group B4.37-269, Tech. Rep., 2005.

[9] "Guide for the Development of Models for HVDC Converters in a HVDC Grid," Cigre Working Group B4.57-604, Tech. Rep., 2014.

[10] K. Frey, M. Garg, R. Morgenstern, N. Platt and E. Spahic, "Provision of fast frequency response by SVC plus frequency stabilizer," 15th IET International Conference on AC and DC Power Transmission (ACDC 2019), 2019, pp. 1-6, doi: 10.1049/cp.2019.0053.

[11] Collados-Rodriguez, C., Cheah-Mane, M., Cifuentes-Garcia, F., Prieto-Araujo, E., Gomis-Bellmunt, O., Coronado, L., Longas, C., Sanz, S., Martin, M., & Cordon, A. (2022). Integration of an MMC-HVDC Link to the Existing LCC-HVDC Link in Balearic Islands Based on Grid-Following and Grid-Forming Operation. IEEE Transactions on Power Delivery, 8977(c), 1–11.
[12] The Paris Agreement, https://www.un.org/en/climatechange/paris-agreement, United Nations Climate Change, 2016.
[13] Engler, A. Device for Parallel Operation of Equal Range Single-Phase or Three-Phase Voltage Sources. EP1286444B1, 21 August 2001.
[14] Lasseter, R. H., Chen, Z., & Pattabiraman, D. (2020). Grid-Forming Inverters: A Critical Asset for the Power Grid. IEEE Journal of Emerging and Selected Topics in Power Electronics, 8(2), 925–935.
[15] M. C. Chandorkar, D. M. Divan and R. Adapa, "Control of parallel connected inverters in standalone AC supply systems," in IEEE Transactions on Industry Applications, vol. 29, no. 1, pp. 136-143, Jan.-Feb. 1993, doi: 10.1109/28.195899.
[16] Du, W., Chen, Z., Member, S., Schneider, K. P., Member, S., Lasseter, R. H., Fellow, L., Nandanoori, S. P., Tuffner, F. K., & Kundu, S. (2020). A Comparative Study of Two Widely Used Grid-Forming Droop Controls on Microgrid Small-Signal Stability. 8(2), 963–975.
[17] Zhong, Q. C., & Weiss, G. (2011). Synchronverters: Inverters that mimic synchronous generators. IEEE Transactions on Industrial Electronics, 58(4), 1259–1267.
[18] Alipoor, J., Miura, Y., & Ise, T. (2015). Power System Stabilization Using Virtual Synchronous Generator with Alternating Moment of Inertia. IEEE Journal of Emerging and Selected Topics in Power Electronics,03(2), 451–458.
[19] Chen, M., Zhou, D., & Blaabjerg, F. (2020). Modelling, Implementation, and Assessment of Virtual Synchronous Generator in Power Systems. Journal of Modern Power Systems and Clean Energy, 8(3), 399–411.
[20] Sakimoto, K. I., Sugimoto, K., & Shindo, Y. (2013). Low voltage ride through capability of a grid connected inverter based on the virtual synchronous generator. Proceedings of the International Conference on Power Electronics and Drive Systems, 1066–1071.
[21] H. P. Beck and R. Hesse, "Virtual synchronous machine," 2007 9th International Conference on Electrical Power Quality and Utilisation, 2007, pp. 1-6, doi: 10.1109/EPQU.2007.4424220.
[22] Johnson, B.B.; Sinha, M.; Ainsworth, N.G.; Dorfler, F.; Dhople, S.V. Synthesizing virtual oscillators to control islanded inverters. IEEE Trans. Power Electron. 2016, 31, 6002–6015.
[23] Johnson, B.; Rodriguez, M.; Sinha, M.; Dhople, S. Comparison of virtual oscillator and droop control. In Proceedings of the IEEE 18th Workshop on Control and Modeling for Power Electronics (COMPEL), Stanford, CA, USA, 9–14 July 2017; IEEE: Piscataway, NJ, USA, 2017.
[24] Unruh, Peter, Maria Nuschke, Philipp Strauß, and Friedrich Welck. 2020. "Overview on Grid-Forming Inverter Control Methods" Energies 13, no. 10: 2589.
[25] Liu, J., Miura, Y., & Ise, T. (2016). Comparison of Dynamic Characteristics between Virtual Synchronous Generator and Droop Control in Inverter-Based Distributed Generators. IEEE Transactions on Power Electronics, 31(5), 3600–3611.

[26] D'Arco, S., & Suul, J. A. (2014). Equivalence of virtual synchronous machines and frequency-droops for converter-based Microgrids. IEEE Transactions on Smart Grid, 5(1), 394–395.
[27] IEEE Standard for Interconnection and Interoperability of Inverter-Based Resources (IBRs) Interconnecting with Associated Transmission Electric Power Systems. IEEE Std 2800™-2022, 2022.
[28] Y. Gu and T. C. Green, "Power System Stability With a High Penetration of Inverter-Based Resources," in Proceedings of the IEEE, 2022, doi: 10.1109/JPROC.2022.3179826.
[29] Dong, S., Chi, Y., & Li, Y. (2016). Active voltage feedback control for hybrid multiterminal HVDC system adopting improved synchronverters. IEEE Transactions on Power Delivery, 31(2), 445–455.
[30] N. Bottrell and T. C. Green, "Comparison of Current-Limiting Strategies During Fault Ride-Through of Inverters to Prevent Latch-Up and Wind- Up," IEEE Trans. Power Electron., vol. 29, no. 7, pp. 3786–3797, Jul. 2014.
[31] Guo, C., Liu, W., Zhao, C., & Iravani, R. (2017). A Frequency-Based Synchronization Approach for the VSC-HVDC Station Connected to a Weak AC Grid. IEEE Transactions on Power Delivery, 32(3), 1460–1470.
[32] F. Colas, T. Qoria, X. Guillaud, F. Gruson. Deliverable 3.5 Local Control for Grid-Forming Converters: Experimental Validation. Migrate, 2019, 41.
[33] Ashabani, M. (2014). Synchronous converter and synchronous-VSC-state of art of universal control strategies for smart grid integration. Smart Grid Conference 2014, SGC 2014, 1–8.
[34] Me, S. P., Zabihi, S., Blaabjerg, F., & Bahrani, B. (2021). Adaptive Virtual Resistance for Post-fault Oscillation Damping with Grid-forming Control. IEEE Transactions on Power Electronics, 8993(c), 1–1.
[35] Taul, M. G., Wang, X., Davari, P., & Blaabjerg, F. (2020). Dynamics of Grid-Forming Converters During Fault Conditions. IEEE Journal of Emerging and Selected Topics in Power Electronics, 8(2), 1062–1073.
[36] Paquette, A. D., & Divan, D. M. (2015). Virtual Impedance Current Limiting for Inverters in Microgrids with Synchronous Generators. IEEE Transactions on Industry Applications, 51(2), 1630–1638.
[37] Rosso, R., Wang, X., Liserre, M., Lu, X., & Engelken, S. (2020). Grid-forming converters: An overview of control approaches and future trends. ECCE 2020 - IEEE Energy Conversion Congress and Exposition, 4292–4299.
[38] Mo, O., Darco, S., & Suul, J. A. (2017). Evaluation of Virtual Synchronous Machines with Dynamic or Quasi-Stationary Machine Models. IEEE Transactions on Industrial Electronics, 64(7), 5952–5962.
[39] Kkuni, K. V., Mohan, S., Yang, G., & Xu, W. (2021). Comparative assessment of typical control realizations of grid forming converters based on their voltage source behaviour. 1–22.
[40] Aresuul, J., & Darco, S. (2018). Comparative Analysis of Small-Signal Dynamics in Virtual Synchronous Machines and Frequency-Derivative-Based Inertia Emulation. Proceedings - 2018 IEEE 18th International Conference on Power Electronics and Motion Control, PEMC 2018, 268053, 344–351.

[41] Unamuno, E., Suul, J. A., Molinas, M., & Barrena, J. A. (2019). Comparative Eigenvalue Analysis of Synchronous Machine Emulations and Synchronous Machines. IECON 2019 - 45th Annual Conference of the IEEE Industrial Electronics Society, 1, 3863–3870.
[42] Qu, Z., Peng, J. C. H., Yang, H., & Srinivasan, D. (2021). Modeling and Analysis of Inner Controls Effects on Damping and Synchronizing Torque Components in VSG-Controlled Converter. IEEE Transactions on Energy Conversion, 36(1), 488–499.
[43] Huang, L., Xin, H., Yang, H., Wang, Z., & Xie, H. (2018). Interconnecting Very Weak AC Systems by Multiterminal VSC-HVDC Links with a Unified Virtual Synchronous Control. IEEE Journal of Emerging and Selected Topics in Power Electronics, 6(3), 1041–1053.
[44] Li, C., Li, Y., Cao, Y., Zhu, H., Rehtanz, C., & Hager, U. (2018). Virtual Synchronous Generator Control for Damping DC-Side Resonance of VSC-MTDC System. IEEE Journal of Emerging and Selected Topics in Power Electronics, 6(3), 1054–1064.
[45] Ørum, E., Kuivaniemi, M., Laasonen, M., Bruseth, A. I., Jansson, E. A., Danell, A., Elkington, K., & Modig, N. (2015). ENTSO Report - Future System Inertia. 1–58.
[46] D. Zografos, M. Ghandhari, "Power system inertia estimation by approaching load power change after a disturbance," in 2017 IEEE Power & Energy Society General Meeting, Chicago, IL, USA, 2017, pp. 1-5.
[47] J. Zhao, Y. Tang and V. Terzija, "Robust online estimation of power system center of inertia frequency," IEEE Trans. Power Syst., vol. 34, no. 1, pp. 821-825, Jan. 2019.
[48] Kundur P. Power system stability and control [M]. New York: McGraw-hill, 1994.
[49] B. M. Weedy and B. J. Cory, Electric Power Systems, 4th Edition. West Sussex, England: John Wiley & Sons Ltd., 1998.
[50] J. Arrillaga, High Voltage Direct Current Transmission, 2nd Edition. London: The Institution of Electrical Engineers, 1998.
[51] E. W. Kimbark, Direct Current Transmission, Vol. I. New York: Wiley, 1971.
[52] "HVDC grid feasibility study", Cigre WG B4.52-533, 2013.
[53] "IEEE guide for planning DC links terminating at AC locations having low short-circuit capacities," IEEE Std 1204-1997, Tech. Rep., 1997.
[54] X. Jiang and A.M. Gole, "Frequency Scanning Method for the Identification of Harmonic Instabilities in HVDC Systems", IEEE Trans. Power Delivery, Vol 10, No. 4., October 1995, pp1875-1881.
[55] D. Grahame Holmes, Thomas A. Lipo. Pulse Width Modulation for Power Converters: Principles and Practice. Wiley, IEEE Press, 2003.
[56] Dzung, P. Q., Nguyen, et al. (2014). New space vector PWM method based on virtual flux vector for T-NPC inverter. Proceedings of the 2014 9th IEEE Conference on Industrial Electronics and Applications, ICIEA 2014, 1371–1376.
[57] Tan, L., Wu, B., Sood, V., Xu, D., Narimani, M., Cheng, Z., & Zargari, N. R. (2018). A Simplified Space Vector Modulation for Four-Level Nested Neutral-Point Clamped Inverters with Complete Control of Flying-Capacitor Voltages. IEEE Transactions on Power Electronics.
[58] A. Nabae, I. Takahashi, and H. Akagi, "A New Neutral-Point-Clamped PWM Inverter," IEEE Transactions on Industry Applications, vol. IA-17, pp. 518–523, September/October 1981.

[59] A. Yazdani and R. Iravani, Voltage-Sourced Converters in Power Systems: Modeling, Control and Applications, John Wiley & Sons, 2010.
[60] K. Sharifabadi, L. Harnefors, et.al, "Design, Control, and Application of Modular Multilevel Converters for HVDC Transmission Systems". ISBN: 978-1-118-85156-2 Wiley-IEEE Press, October 2016.
[61] J. Rodríguez, J.-S. Lai, and F. Z. Peng, "Multilevel inverters: a survey of topologies, controls, and applications," IEEE Trans. Ind. Electron., vol. 49, no. 5, pp. 724–738, August 2002.
[62] N. Flourentzou, V. G. Agelidis, and G. D. Demetriades, "VSC-based HVDC power transmission systems: An overview," IEEE Trans. Power Electron., vol. 24, no. 3, pp. 592–602, March 2009.
[63] M. Glinka and R. Marquardt, "A new AC/DC multilevel converter family," IEEE Trans. Power Electron., vol. 52, no. 3, pp. 662–669, June 2005.
[64] R.Marquardt, A. Lesnicar, and J. Hildinger, "Modulares Stromrichterkonzept für Netzkupplungsanwendung beihohen Spannungen," Proceedings of the ETG-Fachtagung, Bad Nauheim, Germany, 2002.
[65] J. D. Ainsworth, M. Davies, P. J. Fitz, K. E. Owen, and D. R. Trainer, "Static Var compensator (STATCOM) based on single-phase chain circuit converters," IEE Proceedings: Generation, Transmission and Distribution, vol.145, no. 4, pp. 381–386, 1998.
[66] J. S. Lai and F. Z. Peng, "Multilevel converters—A new breed of power converters", Proc. Conf. Rec. IEEE Ind. Appl. Soc. Annu. Meeting, pp. 2348-2356, 1995.
[67] J. Wang, R. Burgos and D. Boroyevich, "A survey on the modular multilevel converters — Modeling, modulation and controls," 2013 IEEE Energy Conversion Congress and Exposition, 2013, pp. 3984-3991, doi: 10.1109/ECCE.2013.6647229.
[68] S. Allebrod, R. Hamerski, and R. Marquardt, "New transformerless, scalable modular multilevel converters for HVDC-transmission," in IEEE Power Electronics Specialists Conference - PESC 2008, Rhodes, Greece, 2008.
[69] Lin, W., Jovcic, D., Nguefeu, S., & Saad, H. (2016). Full-Bridge MMC Converter Optimal Design to HVDC Operational Requirements. IEEE Transactions on Power Delivery, 31(3), 1342–1350.
[70] Barker, C.D., Whitehouse, R.S., Adamczyk, A.G., et al; "Low frequency active power oscillation damping using a MMC-VSC HVDC link". 13th IET Int. Conf. on AC and DC Power Transmission (ACDC 2017), Manchester, UK, 2017, pp. 1– 6
[71] M. Saeedifard, and R. Iravani, "Dynamic Performance of a Modular Multilevel Back-to-Back HVDC System," IEEE Trans. on Power Delivery, vol. 25, no. 4, pp. 2903-2912, Oct. 2010.
[72] E. Solas, G. Abad, J. A. Barrena, A. Carcar, and S. Aurtenetxea, "Modulation of Modular Multilevel Converter for HVDC Application," 14th International Power Electronic and Motion Control Conference, pp. 84-89, Mondragon, Sep. 2010.
[73] G. Ding, G. Tang, Z. He, and M. Ding, "New Technologies of Voltage Source Converter (VSC) for HVDC Transmission System Based on VSC," in Proc. IEEE Power Eng. Soc. General Meeting, pp. 1-8, Beijing, Jun. 2008.
[74] Q. Tu, and Z. Xu, "Impact of Sampling Frequency on Harmonic Distortion for Modular Multilevel Converter," IEEE Trans. on Power Delivery, vol. 26, no. 1, pp.298-306, Jan. 2011.

[75] J. Rocabert, A. Luna, F. Blaabjerg, and P. Rodríguez, “Control of power converters in ac microgrids,” IEEE Trans. Power Electron., vol. 27, no. 11, pp. 4734–4749, Nov. 2012.
[76] K. Li, and C. Zhao, “New Technologies of Modular Multilevel Converter for VSC-HVDC Application,” Asia-Pacific Power and Energy Eng. Conference (APPEEC), Baoding, Mar. 2010.
[77] Gnanarathna, U. N., Gole, A. M., & Jayasinghe, R. P. (2011). Efficient modeling of modular multilevel HVDC converters (MMC) on electromagnetic transient simulation programs. IEEE Transactions on Power Delivery, 26(1), 316–324.
[78] General Electric Company, Electric Power Research Institute.” Transmission line reference book, 345 kV and above (second edition),” Electric Power Research Institute, Palo Alto, 1982.
[79] J. Peralta, H. Saad, S. Dennetiere, J. Mahseredjian and S. Nguefeu, "Detailed and Averaged Models for a 401-Level MMC–HVDC System," in IEEE Transactions on Power Delivery, vol. 27, no. 3, pp. 1501-1508, July 2012.
[80] B. Jacobson, P. Karlsson, G. Asplund, L. Harnefors, and T. Jonsson, “VSC-HVDC transmission with cascaded two-level converters,” Proceedings of CIGRÉ 2010, vol. B4-110, 2010.
[81] C. Oates, “Modular multilevel converter design for VSC HVDC applications,” IEEE Journal of Emerging and Selected Topics in Power Electronics, vol. 3, no. 2, pp. 505–515, Jun. 2015.
[82] C. D. Barker and N. M. Kirby, "Reactive power loading of components within a modular multi-level HVDC VSC converter," 2011 IEEE Electrical Power and Energy Conference, 2011, pp. 86-90.
[83] C. Du, M. H. J. Bollen, E. Agneholm and A. Sannino, "A New Control Strategy of a VSC–HVDC System for High-Quality Supply of Industrial Plants," in IEEE Transactions on Power Delivery, vol. 22, no. 4, pp. 2386-2394, Oct. 2007.
[84] Du, C. “VSC-HVDC for Industrial Power Systems”. PhD thesis, Chalmers University of Technology, Gothenburg, Sweden, 2007.
[85] R. H. Park, "Two-reaction theory of synchronous machines generalized method of analysis-part I," in Transactions of the American Institute of Electrical Engineers, vol. 48, no. 3, pp. 716-727, July 1929.
[86] B. Fan, T. Liu, F. Zhao, H. Wu and X. Wang, "A Review of Current-Limiting Control of Grid-Forming Inverters Under Symmetrical Disturbances," in IEEE Open Journal of Power Electronics, vol. 3, pp. 955-969, 2022.
[87] Mehrmann, Volker and Stykel, Tatjana. "Descriptor Systems: A General Mathematical Framework for Modelling, Simulation and Control, vol. 54, no. 8, 2006, pp. 405-415.
[88] Darbandi, A. F., Sinkar, A., & Gole, A. Effect of Short-Circuit Ratio and Current Limiting on the Stability of a Virtual Synchronous Machine Type Grid forming Converter. 182–187, 2022.
[89] The MathWorks, Inc., Natick, MA. MATLAB Version 7.0.4.352 (R14), 2005.
[90] N. Pogaku, M. Prodanovic, and T. C. Green, “Modeling, Analysis and Testing of Autonomous Operation of an Inverter-Based Microgrid,” IEEE Trans. Power Electron., vol. 22, no. 2, pp. 613–625, Mar. 2007.
[91] U.S. Department of Energy, “Grid Modernization Multi-Year Program Plan,” 2017.

[92] International Energy Agency, “The Power of Transformation: Wind, Sun and the Economics of Flexible Power Systems,” 2014.
[93] National Renewable Energy Laboratory, "Renewable Energy Grid Integration Data Book: 2018 Edition," 2018.
[94] V. K. Sood, V. Khatri, H. Jin, “Performance Assessment using EMTP of two Gate Firing Units for HVDC Converters operating with Weak AC Systems”, International Conference on Power System Transients, Sept. 3-7, 1995, Technical University of Lisbon, Portugal. pp 517-522.
[95] V.K.Sood, HVDC and FACTS Controllers - Applications of Static Converters in Power Systems, April 2004, ISBN 1-4020-7890-0, Published by Kluwer Academic Publishers, 300 pages.

Appedix A

A.1 Park transformation

The three-phase voltage or current vectors in abc domain can be transferred into a rotating dq domain at angular velocity ω through park transformation as shown in Figure A-1. This can be expressed by

$$\overrightarrow{u_{dq0}} = K_T \cdot \overrightarrow{u_{abc}} \tag{A.1}$$

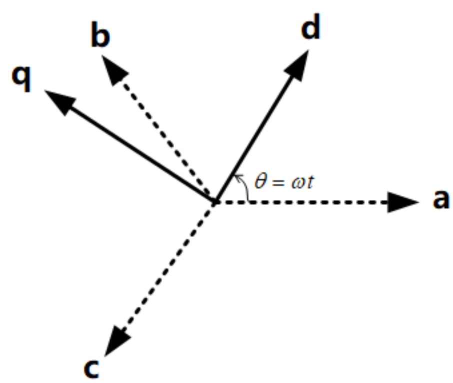

Figure A-1 transformation from abc to dq domain

Assuming the synchronization angle $\theta = \omega t$, and q axis leads d axis, then in (A.1)

$$K_T = \frac{2}{3}\begin{bmatrix} \cos\theta & \cos(\theta-\frac{2}{3}\pi) & \cos(\theta+\frac{2}{3}\pi) \\ -\sin\theta & -\sin(\theta-\frac{2}{3}\pi) & -\sin(\theta+\frac{2}{3}\pi) \\ \frac{1}{2} & \frac{1}{2} & \frac{1}{2} \end{bmatrix} \tag{A.2}$$

Note that, if q axis lags d axis, then

$$K_{Tlag} = \frac{2}{3}\begin{bmatrix} \cos\theta & \cos(\theta-\frac{2}{3}\pi) & \cos(\theta+\frac{2}{3}\pi) \\ \sin\theta & \sin(\theta-\frac{2}{3}\pi) & \sin(\theta+\frac{2}{3}\pi) \\ \frac{1}{2} & \frac{1}{2} & \frac{1}{2} \end{bmatrix} \tag{A.3}$$

The reverse transformation from dq domain to abc domain can be expressed by

$$\overrightarrow{u_{abc}} = K_T^{-1} \cdot \overrightarrow{u_{dq0}} \tag{A.4}$$

In (A.4),

$$K_T^{-1} = \begin{bmatrix} \cos\theta & -\sin\theta & 1 \\ \cos(\theta-\frac{2}{3}\pi) & -\sin(\theta-\frac{2}{3}\pi) & 1 \\ \cos(\theta+\frac{2}{3}\pi) & -\sin(\theta+\frac{2}{3}\pi) & 1 \end{bmatrix} \tag{A.5}$$

If q axis lags d axis,

$$K_{Tlag}^{-1} = \begin{bmatrix} \cos\theta & \sin\theta & 1 \\ \cos(\theta-\frac{2}{3}\pi) & \sin(\theta-\frac{2}{3}\pi) & 1 \\ \cos(\theta+\frac{2}{3}\pi) & \sin(\theta+\frac{2}{3}\pi) & 1 \end{bmatrix} \tag{A.6}$$

A.2 Linearization of the network dynamic equations

Applying Kirchhoff's Voltage Law (KVL) to the circuit shown in Figure 4-2. In abc domain, the network dynamics from PCC bus to the Thevenin equivalent voltage source can be expressed by

$$v_{sabc} - v_{tabc} + R_s i_{abc} + L_s \frac{di_{abc}}{dt} = 0 \tag{A.7}$$

R_s and L_s are the equivalent inductance and resistance from PCC bus to the Thevenin equivalent voltage source. In the matrix form, (A.7) can be written as

$$\begin{bmatrix} v_{sa} \\ v_{sb} \\ v_{sc} \end{bmatrix} - \begin{bmatrix} v_{ta} \\ v_{tb} \\ v_{tc} \end{bmatrix} + \begin{bmatrix} R_s & 0 & 0 \\ 0 & R_s & 0 \\ 0 & 0 & R_s \end{bmatrix} \begin{bmatrix} i_a \\ i_b \\ i_c \end{bmatrix} + \begin{bmatrix} L_s & 0 & 0 \\ 0 & L_s & 0 \\ 0 & 0 & L_s \end{bmatrix} \frac{d}{dt} \begin{bmatrix} i_a \\ i_b \\ i_c \end{bmatrix} = 0 \tag{A.8}$$

Applying Park transformation to (A.8),

$$K_{Tlag}^{-1} \left(\begin{bmatrix} v_{td} \\ v_{tq} \\ v_{t0} \end{bmatrix} - \begin{bmatrix} v_{sd} \\ v_{sq} \\ v_{s0} \end{bmatrix} \right) = \begin{bmatrix} R_s & 0 & 0 \\ 0 & R_s & 0 \\ 0 & 0 & R_s \end{bmatrix} K_{Tlag}^{-1} \begin{bmatrix} i_d \\ i_q \\ i_0 \end{bmatrix} + \begin{bmatrix} L_s & 0 & 0 \\ 0 & L_s & 0 \\ 0 & 0 & L_s \end{bmatrix} \frac{d}{dt} \left(K_{Tlag}^{-1} \begin{bmatrix} i_d \\ i_q \\ i_0 \end{bmatrix} \right) \tag{A.9}$$

Multiply K_{Tlag} on both sides of the equation,

$$\begin{bmatrix} v_{td} \\ v_{tq} \\ v_{t0} \end{bmatrix} - \begin{bmatrix} v_{sd} \\ v_{sq} \\ v_{s0} \end{bmatrix} = R_s \begin{bmatrix} i_d \\ i_q \\ i_0 \end{bmatrix} + K_{Tlag} \cdot L_s \frac{d}{dt} \left(K_{Tlag}^{-1} \begin{bmatrix} i_d \\ i_q \\ i_0 \end{bmatrix} \right) \tag{A.10}$$

In (A.10),

$$K_{Tlag} \cdot L_s \frac{d}{dt} \left(K_{Tlag}^{-1} \begin{bmatrix} i_d \\ i_q \\ i_0 \end{bmatrix} \right) = K_{Tlag} \cdot L_s \frac{d}{dt} \left(K_{Tlag}^{-1} \right) \begin{bmatrix} i_d \\ i_q \\ i_0 \end{bmatrix} + L_s \frac{d}{dt} \left(\begin{bmatrix} i_d \\ i_q \\ i_0 \end{bmatrix} \right) \tag{A.11}$$

According to (A.3) and (A.6),

$$
\frac{d}{dt}(K_{Tlag}^{-1}) = \frac{d}{dt}\begin{bmatrix} \cos\theta & \sin\theta & 1 \\ \cos(\theta - \frac{2}{3}\pi) & \sin(\theta - \frac{2}{3}\pi) & 1 \\ \cos(\theta + \frac{2}{3}\pi) & \sin(\theta + \frac{2}{3}\pi) & 1 \end{bmatrix}
$$

$$
= \omega\begin{bmatrix} -\sin\theta & \cos\theta & 0 \\ -\sin(\theta - \frac{2}{3}\pi) & \cos(\theta - \frac{2}{3}\pi) & 0 \\ -\sin(\theta + \frac{2}{3}\pi) & \cos(\theta + \frac{2}{3}\pi) & 0 \end{bmatrix} \tag{A.12}
$$

Substitute (A.12) into (A.11) and (A.10), (A.10) can be rearranged as

$$
\begin{bmatrix} v_{td} \\ v_{tq} \\ v_{t0} \end{bmatrix} - \begin{bmatrix} v_{sd} \\ v_{sq} \\ v_{s0} \end{bmatrix} - R_s\begin{bmatrix} i_d \\ i_q \\ i_0 \end{bmatrix} - L_s\frac{d}{dt}\begin{bmatrix} i_d \\ i_q \\ i_0 \end{bmatrix} - \omega L_s\begin{bmatrix} 0 & 1 & 0 \\ -1 & 0 & 0 \\ 0 & 0 & 0 \end{bmatrix}\begin{bmatrix} i_d \\ i_q \\ i_0 \end{bmatrix} = 0 \tag{A.13}
$$

Thus, in a three-phase balanced system,

$$
\begin{cases} L_s\dfrac{di_d}{dt} = v_{td} - v_{sd} - R_s i_d - \omega L_s i_q \\ L_s\dfrac{di_d}{dt} = v_{tq} - v_{sq} - R_s i_q + \omega L_s i_d \end{cases} \tag{A.14}
$$

Similarly, if L is the equivalent inductance from the converter terminal to the PCC bus, for the network dynamics from the converter terminal to PCC bus,

$$
\begin{cases} L\dfrac{di_d}{dt} = v_{cd} - v_{td} - \omega L i_q \\ L\dfrac{di_d}{dt} = v_{cq} - v_{tq} + \omega L i_d \end{cases} \tag{A.15}
$$

In pu unit, (A.14) and (A.15) can be linearized as

$$
\begin{cases} \dfrac{L_s}{\omega_0}\dfrac{d\Delta i_d}{dt} = \Delta v_{td} - \Delta v_{sd} - L_s i_q \Delta\omega - L_s \omega \Delta i_q - R_s \Delta i_d \\ \dfrac{L_s}{\omega_0}\dfrac{d\Delta i_q}{dt} = \Delta v_{tq} - \Delta v_{sq} + L_s i_d \Delta\omega + L_s \omega \Delta i_d - R_s \Delta i_q \end{cases} \tag{A.16}
$$

$$\begin{cases} \frac{L}{\omega_0}\frac{d\Delta i_d}{dt} = \Delta v_{cd} - \Delta v_{td} - Li_q\Delta\omega - L\omega\Delta i_q \\ \frac{L}{\omega_0}\frac{d\Delta i_q}{dt} = \Delta v_{cq} - \Delta v_{tq} + Li_d\Delta\omega + L\omega\Delta i_d \end{cases} \tag{A.17}$$

ω_0 is the nominal angular velocity at 376.99 rad/s.

Now, assuming the ac voltage angle at PCC bus is θ, and the ac voltage angle at the Thevenin equivalent voltage source is φ, the three-phase voltages at voltage source side are

$$\begin{aligned} v_{sa} &= V_m \cos(\omega t + \varphi - \theta) \\ v_{sb} &= V_m \cos(\omega t - \frac{2}{3}\pi + \varphi - \theta) \\ v_{sc} &= V_m \cos(\omega t + \frac{2}{3}\pi + \varphi - \theta) \end{aligned} \tag{A.18}$$

Also, if q axis lags d axis, v_{sd}, v_{sq} at the Thevenin equivalent voltage source can be expressed by

$$\begin{aligned} \begin{bmatrix} v_{sd} \\ v_{sq} \end{bmatrix} &= \frac{2}{3}\begin{bmatrix} \cos\omega t & \cos(\omega t - \frac{2}{3}\pi) & \cos(\omega t + \frac{2}{3}\pi) \\ \sin\omega t & \sin(\omega t - \frac{2}{3}\pi) & \sin(\omega t + \frac{2}{3}\pi) \\ \frac{1}{2} & \frac{1}{2} & \frac{1}{2} \end{bmatrix}\begin{bmatrix} v_{ta} \\ v_{tb} \\ v_{tc} \end{bmatrix} \\ &= \frac{2}{3}\begin{bmatrix} \cos\omega t & \cos(\omega t - \frac{2}{3}\pi) & \cos(\omega t + \frac{2}{3}\pi) \\ \sin\omega t & \sin(\omega t - \frac{2}{3}\pi) & \sin(\omega t + \frac{2}{3}\pi) \\ \frac{1}{2} & \frac{1}{2} & \frac{1}{2} \end{bmatrix}\begin{bmatrix} V_m \cos(\omega t + \varphi - \theta) \\ V_m \cos(\omega t - \frac{2}{3}\pi + \varphi - \theta) \\ V_m \cos(\omega t + \frac{2}{3}\pi + \varphi - \theta) \end{bmatrix} \\ &= \begin{bmatrix} V_m \cos(\varphi - \theta) \\ -V_m \sin(\varphi - \theta) \end{bmatrix} \end{aligned} \tag{A.19}$$

Thus, (A.19) can be linearized as

$$\begin{cases} \Delta v_{sd} = V_m \sin(\varphi - \theta)\Delta\theta \\ \Delta v_{sq} = V_m \cos(\varphi - \theta)\Delta\theta \end{cases} \tag{A.20}$$

Appedix B

B.1 E, A and B matrix for linearized model of the VSM without in-line cascaded current control

$$E=\begin{bmatrix} 1 & & & & & & & & & & & \\ & J & & & & & & & & & & \\ & & \frac{L}{\omega_0} & & & & & & & & & \\ & & & \frac{L}{\omega_0} & & & & & & & & \\ & & \frac{L_s}{\omega_0} & & & & & & & & & \\ & & & \frac{L_s}{\omega_0} & & & & & & & & \\ & & & & 1 & & & & & & & \\ & & & & & & & & & & & \\ & & & & & & & & & & & \\ & & & & & & & & & & & \\ & & & & & & & & & & & \\ & & & & & & & & & & & \end{bmatrix}_{12\times 12} \tag{B.1}$$

In (B.1), $E_{1,1}=1, E_{2,2}=J, E_{3,3}=E_{4,4}=\frac{L}{\omega_0}, E_{5,3}=E_{6,4}=\frac{L_s}{\omega_0}, M_{7,5}=1.$

$$A=\begin{bmatrix}
 & \omega_0 & & & & & & & & & & \\
 & -D & & & & & & & & & & -1 \\
 & -Li_q & & -L\omega_{vsm} & & 1 & & -1 & & & & \\
 & Li_d & L\omega_{vsm} & & & & 1 & & -1 & & & \\
 & -L_s i_q & -R_s & -L_s\omega_{vsm} & & & & 1 & & -1 & & \\
 & L_s i_d & L_s\omega_{vsm} & -R_s & & & & & 1 & & -1 & \\
 & & & & & & & -\frac{v_{td}}{\sqrt{v_{td}^2+v_{tq}^2}} & -\frac{v_{tq}}{\sqrt{v_{td}^2+v_{tq}^2}} & & & \\
 & & & & K_i & -1 & & -\frac{K_p v_{td}}{\sqrt{v_{td}^2+v_{tq}^2}} & -\frac{K_p v_{tq}}{\sqrt{v_{td}^2+v_{tq}^2}} & & & \\
 & & & & & & 1 & & & & & \\
 & & v_{td} & v_{tq} & & & & i_d & i_q & & & -1 \\
V_m\sin(\varphi-\theta) & & & & & & & & & -1 & & \\
V_m\sin(\varphi-\theta) & & & & & & & & & & -1 &
\end{bmatrix}_{12\times 12} \tag{B.2}$$

In (B.2),

$A_{1,2} = \omega_0$,

$A_{2,12} = -1, A_{2,2} = -D$,

$A_{3,6} = 1, A_{3,8} = -1, A_{3,2} = -Li_q, A_{3,4} = -L\omega_{vsm}$,

$A_{4,7} = 1, A_{4,9} = -1, A_{4,2} = Li_d, A_{4,3} = L\omega_{vsm}$,

$A_{5,8} = 1, A_{5,10} = -1, A_{5,2} = -L_s i_q, A_{5,4} = -L_s\omega_{vsm}, A_{5,3} = -R_s$,

$A_{6,9} = 1, A_{6,11} = -1, A_{6,2} = L_s i_d, A_{6,3} = L_s\omega_{vsm}, A_{6,4} = -R_s$,

$A_{7,8} = -\frac{V_{td}}{\sqrt{V_{td}^2+V_{tq}^2}}, A_{7,9} = -\frac{V_{tq}}{\sqrt{V_{td}^2+V_{tq}^2}}$,

$A_{8,8} = -K_p\frac{V_{td}}{\sqrt{V_{td}^2+V_{tq}^2}}, A_{8,9} = -K_p\frac{V_{tq}}{\sqrt{V_{td}^2+V_{tq}^2}}, A_{8,5} = K_i, A_{8,6} = -1$,

$A_{9,7} = 1, A_{9,2} = Li_d, A_{9,3} = L\omega_{vsm}$,

$A_{10,3} = V_{td}, A_{10,8} = i_d, A_{10,4} = V_{tq}, A_{10,9} = i_q, A_{10,12} = -1$,

$A_{11,1} = V_m\sin(\varphi-\theta), A_{11,10} = -1$,

$A_{12,1} = V_m\sin(\varphi-\theta), A_{12,11} = -1$.

$$B = \begin{bmatrix} & \\ 1 & \\ & \\ & \\ & \\ & \\ & 1 \\ K_p & \\ & \\ & \\ & \\ & \end{bmatrix}_{12\times 2} \tag{B.3}$$

In (B.3), $B_{2,1} = 1, B_{7,2} = 1, B_{8,2} = K_p$.

B.2 E, A and B matrix for linearized model of the VSM with in-line cascaded current control

$$
E=\begin{bmatrix}
1&&&&&&&&&&&&&&&&\\
&1&&&&&&&&&&&&&&&\\
&&1&&&&&&&&&&&&&&\\
&&&1&&&&&&&&&&&&&\\
&&&&1&&&&&&&&&&&&\\
&&&&&J&&&&&&&&&&&\\
&&&&&&\frac{L}{\omega_0}&&&&&&&&&&\\
&&&&&&&\frac{L}{\omega_0}&&&&&&&&&\\
&&&&&&\frac{L_s}{\omega_0}&&&&&&&&&&\\
&&&&&&&\frac{L_s}{\omega_0}&&&&&&&&&\\
&&&&&&&&&&&&&&&&\\
&&&&&&&&&&&&&&&&\\
&&&&&&&&&&&&&&&&\\
&&&&&&&&&&&&&&&&\\
&&&&&&&&&&&&&&&&\\
&&&&&&&&&&&&&&&&\\
&&&&&&&&&&&&&&&&
\end{bmatrix}_{17\times 17} \tag{B.4}
$$

In (B.4), $E_{1,1}=E_{2,2}=E_{3,3}=E_{4,4}=E_{5,5}=1, E_{6,6}=J, E_{7,7}=E_{8,8}=\frac{L}{\omega_0}, E_{9,7}=E_{10,8}=\frac{L_s}{\omega_0}$.

$$
A=\begin{bmatrix}
&&&&&&&&&&-1&&&&&&\\
&&&&&&&&&&&-1&&&&&\\
&&&&&&-1&&&&&&&&1&&\\
&&&&&&&-1&&&&&&&&1&\\
&&&&&\omega_0&&&&&&&&&&&\\
&&&&&-D&&&&&&&&&&&-1\\
&&&&&-Li_q&&-L\omega_{vsm}&1&&-1&&&&&&\\
&&&&&Li_d&L\omega_{vsm}&&&1&&-1&&&&&\\
&&&&&-L_s i_q&-R_s&-L_s\omega_{vsm}&&&1&&-1&&&&\\
&&&&&L_s i_d&L_s\omega_{vsm}&-R_s&&&&1&&-1&&&\\
K_{vi}&&&&&&&&&&-K_{vp}&&&&-1&&\\
&K_{vi}&&&&&&&&&&-K_{vp}&&&&-1&\\
&&K_{ii}&&&&-K_{ip}&-\omega_0 L&-1&&1&&&&K_{ip}&&\\
&&&K_{ii}&&&\omega_0 L&-K_{ip}&&-1&&1&&&&K_{ip}&\\
&&&&&&v_{td}&v_{tq}&&&i_d&i_q&&&&&-1\\
&&&&V_m\sin(\varphi-\theta)&&&&&&&&-1&&&&\\
&&&&V_m\sin(\varphi-\theta)&&&&&&&&&-1&&&
\end{bmatrix}_{17\times 17} \tag{B.5}
$$

In (B.5),

$A_{1,11}=-1$,

$A_{2,12}=-1$,

$A_{3,15}=1, A_{3,7}=-1$,

$A_{4,16} = 1, A_{4,8} = -1,$

$A_{5,6} = \omega_b,$

$A_{6,17} = -1, A_{6,6} = -D,$

$A_{7,9} = 1, A_{7,11} = -1, A_{7,6} = -Li_q, A_{7,8} = -L\omega_{vsm},$

$A_{8,10} = 1, A_{8,12} = -1, A_{8,6} = Li_d, A_{8,7} = L\omega_{vsm},$

$A_{9,11} = 1, A_{9,13} = -1, A_{9,6} = -L_s i_q, A_{9,8} = -L_s\omega_{vsm}, A_{9,7} = -R_s,$

$A_{10,12} = 1, A_{10,14} = -1, A_{10,6} = L_s i_d, A_{10,7} = L_s\omega_{vsm}, A_{10,8} = -R_s,$

$A_{11,11} = -K_{vp}, A_{11,1} = K_{vi}, A_{11,15} = -1,$

$A_{12,12} = -K_{vp}, A_{12,2} = K_{vi}, A_{12,16} = -1,$

$A_{13,15} = K_{ip}, A_{13,7} = -K_{ip}, A_{13,3} = K_{ii}, A_{13,8} = -\omega_0 L, A_{13,11} = 1, A_{13,9} = -1,$

$A_{14,16} = K_{ip}, A_{14,8} = -K_{ip}, A_{14,4} = K_{ii}, A_{14,7} = \omega_0 L, A_{14,12} = 1, A_{14,10} = -1,$

$A_{15,7} = V_{td}, A_{15,11} = i_d, A_{15,8} = V_{tq}, A_{15,12} = i_q, A_{15,17} = -1,$

$A_{16,5} = V_m \sin(\varphi - \theta), A_{16,13} = -1,$

$A_{17,5} = V_m \sin(\varphi - \theta), A_{17,14} = -1.$

$$B = \begin{bmatrix} & 1 \\ & \\ & \\ & \\ & \\ 1 & \\ & \\ & \\ & \\ & \\ & K_{vp} \\ & \\ & \\ & \\ & \\ & \\ & \end{bmatrix}_{17\times 2} \tag{B.6}$$

In (B.6), $B_{1,2} = 1, B_{6,1} = 1, B_{11,2} = K_{vp}$.